# REPORT DOCUMENTATION PAGE

Public reporting burden for this collection of information is estimated to average 1 hour per response, including the time for reviewing instructions, searching existing data sources, gathering and maintaining the data needed, and completing and reviewing the collection of information. Send comment regarding this burden estimates or any other aspect of this collection of information, including suggestions for reducing this burden, to Washington Headquarters Services, Directorate for information Operations and Reports, 1215 Jefferson Davis Highway, Suite 1204, Arlington, VA 22202-4302, and to the Office of Management and Budget, Paperwork Reduction Project (0704-0188), Washington, DC 20503.

| 1. AGENCY USE ONLY (Leave blank) | 2. REPORT DATE 11/01/99 | 3. REPORT TYPE AND DATES COVERED Final Report 04/15/95 - 04/15/98 |
|---|---|---|

**4. TITLE AND SUBTITLE**

Failure Criteria for Composites

**5. FUNDING NUMBERS**

$172,134  for 36 mos.

04/15/95 - 04/15/98

**6. AUTHOR(S)**

Anthony M. Waas, PI

**7. PERFORMING ORGANIZATION NAMES(S) AND ADDRESS(ES)**

University of Michigan
Aerospace Engineering
1320 Beal Avenue
Ann Arbor, MI  48109-2140

**8. PERFORMING ORGANIZATION REPORT NUMBER**

**9. SPONSORING / MONITORING AGENCY NAME(S) AND ADDRESS(ES)**

Air Force Office of Scientific Research
801 N. Randolph Street
Arlington, VA  22203

**10. SPONSORING / MONITORING AGENCY REPORT NUMBER**

**11. SUPPLEMENTARY NOTES**

The views, opinions and/or findings contained in this report are those of the author(s) and should not be construed as an official    AFOSR                position, policy or decision, unless so designated by other documentation.

**12a. DISTRIBUTION / AVAILABILITY STATEMENT**

Approved for public release; distribution unlimited.

**12 b. DISTRIBUTION CODE**

**13. ABSTRACT (Maximum 200 words)**

Understanding the mechanisms of failure of composite structures and developing mechanism based failure criteria are important considerations in designing structures made of composite materials. The compressive response of composite materials has received considerable attention due to their significance in the aerospace industry and the complexity associated with compressive failure. Several competing failure mechanisms such as fiber/matrix interfacial failure, fiber microbuckling/kinking, delamination initiation and delamination buckling may become active in compressive loading. Environmental effects such as an elevated temperature can alter and affect these failure mechanisms. In this project, a micromechanics based predictive model for the notched strength of multidirectional laminates is presented and implemented via the finite element method. Experimental results to verify/refute this model are presented at both room and elevated temperature. The in-situ shear response of the matrix, the fiber mechanical properties, the laminate lay-up and fiber volume fraction serve as input to the model. The predictions of the model are found to match favorably with experimental data. The effect of ply angle and its influence on the failure mechanism are quantified and compared with available experimental data. This work is the first development of a non-empirical mechanics based failure prediction methodology for notched strength of composite laminates.

**14. SUBJECT TERMS**

Compressive Failure, Polymer Matrix Composites,
Biaxial Loads

**15. NUMBER IF PAGES**

**16. PRICE CODE**

| 17. SECURITY CLASSIFICATION OR REPORT | 18. SECURITY CLASSIFICATION OF THIS PAGE | 19. SECURITY CLASSIFICATION OF ABSTRACT | 20. LIMITATION OF ABSTRACT |
|---|---|---|---|
| UNCLASSIFIED | UNCLASSIFIED | UNCLASSIFIED | UL |

Standard Form 298 (Rev. 2-89)
Prescribed by ANSI Std. 239-18
298-102

DTIC QUALITY INSPECTED 4

# TABLE OF CONTENTS

# LIST OF FIGURES

5. Micromechanics Model to Predict Failure of Angle Plies as a Function of Ply Angle

# LIST OF TABLES

# CHAPTER 1

# INTRODUCTION

## 1.1. Introduction

Continuous fiber reinforced composite laminates offer several superior attributes when compared to metals on a pound for pound basis. Because of this, these laminates are increasingly utilized in weight critical aerospace applications. There are numerous textbooks that have been published recently. These provide a broad coverage of the material science aspects and mechanics aspects of composite materials in general and composite laminates in particular.

Although the utilization of composite laminates in structural application is relatively recent, the concepts and basic ideas that are central to the notion that a composite material exhibits superior properties than the constituents by themselves is as old as the straw-reinforced clay bricks in ancient Egypt. In more recent times, iron rods were used to reinforce masonry in the nineteenth century, leading to steel-reinforced concrete. Phenolic resin reinforced with asbestos fibers was introduced in the beginning of the twentieth century. The first fiberglass application was made in 1942, reinforced plastics were also used in aircraft and electrical components. Filament winding was invented in 1946 and incorporated into the manufacturing of missiles applications in the 1950s. The first boron and high strength carbon fibers were introduced in the early 1960s,

with applications of advanced composites to aircraft components by 1968. Metal matrix composites such as boron/aluminum were introduced in 1970. Dupont developed Kevlar (aramid) fibers in 1973. Starting in the late 1970s applications of composites expanded widely to the aircraft, automotive, sporting goods, and biomedical industries. Currently, emphasis is being placed on development of newer metal/matrix and ceramic/matrix composites, as well as carbon/carbon composites, for applications in harsh environments, particularly elevated temperature.

Continuous fiber composites (CFCs) are one of the most important materials to be introduced into aircraft structures in the last 20 years (Figure 1.1). CFCs consist of strong fibers set in a matrix of epoxy resin that is mechanically and chemically protective. They were developed at the RAE Farnborough and announced in 1966. Not only do CFC's possess excellent strength/weight and stiffness but also they offer the unusual opportunity to design the structure and the material simultaneously. The directional properties of composite materials can be used to aeroelastically tailored wing structures in order to obtain, under load, specified twist and camber. This has beneficial effects on aerodynamic drag, control effectiveness and air load distribution, leading to increases in range capability and load carrying capacity. Such tailoring can be used to obtain a lower weight design that satisfies all of the applicable design constrains such as strength, flutter and divergence. Compared to 2000 and 7000 series aluminum alloys, CFC's offer weight savings of 20%. A further advantage is the ability to mould complex shapes.

Still, CFC material remains expensive and labor intensive in fabricating structures. Further drawbacks include significantly reduced strength due to undetected damage, reparability problems, and environmental difficulties. The first major application of CFC was demonstrated in the design of AV-8B Harrier II by the then McDonnell Douglas (Boeing) and British Aerospace. It took about 10 years to get CFC's into the production cycle.

Carbon fiber based CFC's are used extensively in recent aerospace applications (Figure 1.2). Majorities of airplane surface components are being replaced by CFC material except in primary load bearing members (landing gear, main spar), or thermal resistance member (engine mount, nozzle, firewall, etc). The most aggressive application of composite structure in an aerospace vehicle can be seen at scaled composite corporation [Ref. 1.7], where all composite vehicles are being developed and tested. Typical CFC-metal main wing structure along with conventional types is shown in Figure 1.3. Shown is the main wing of the British Aerospace Experimental Aircraft Prototype. Dark areas illustrate the use of CFC and light areas show metal usage, including three titanium-made wing attachment joints.

One particular accomplishment in how the CFC application to structures can be stretched in aero-vehicle design is the Boeing-Sikorski RAH-66 Comanche helicopter (Figure 1.4), currently in the flight testing stage. In addition to conventional composite application to save weight, the Comanche airframe has load-bearing members made of Hercules IM7 graphite in thermosetting epoxy resin. The RAH-66 is built around a composite box (Figure 1.5) beam running the length of the forward fuselage. The beam also provides space for the fuel.

Composites also have opened new opportunities for crashworthy design. Cockpit floors have frangible panels to let the crew seats stroke down in a crash, and the entire tailboom is designed to break away when impacts greater than 20 ft per second occur, to relieve crash loads on the retractable landing gear. The main rotor is an all-composite bearingless design.

Comparably simple to manufacture and cheaper than other exotic composites (carbon-carbon, metallic hybrid, etc), CFC still have many attractive aspects in many applications. An inherent stealthy characteristic (carbon absorbs electromagnetic energy) is another blessing of CFC in recent years. It is noteworthy that apart from one or two exceptions, the top speed of airplanes (military fighter especially) has been limited by neither aerodynamics nor propulsions but by the material/structural efficiency.

One problem that is of significant interest to the US Air Force is the utilization of carbon fiber based polymeric laminates for aircraft application in the presence of moderate to high temperature (room to 500°F). In such applications, the ability of the structure to withstand repeated mechanical loading cycles can be significantly weakened by the presence of elevated temperature. Since polymer matrix composites offer significant advantages in manufacturing, they have been the materials of choice for a number of Department of Defense programs earmarked at reducing weight and thereby cutting operational cost. The notched strength of a composite structure subjected to uniaxial loading at room temperature has been investigated before (see for example, Waas et al. [Ref. 2.5], Soutis [Ref. 4.10], Soutis & Fleck [Ref. 4.5]. The effect of remote biaxial loads, on the other hand, has been less well studied (see, Khamseh & Waas [Ref. 2.11]). In

4

all of these investigations, the focus has been on identifying the dominant failure mechanisms at room temperature. The understanding of failure mechanisms under various loading conditions (uniaxial and biaxial loading, room and elevated temperature) is the subject of the present thesis.

Such an investigation, in some sense, adds closure and completeness to the previous investigations cited above. An additional motivational factor for the present study stemmed from the need to introduce a micromechanics based prediction capability to understand the origins of failure and how the failure mechanism is influenced by factors such as ply angle and stacking sequence. With a view to attaining these goals, a systematic experimental program was designed and the results used to drive the modeling features that are introduced in this thesis.

The organization of this thesis is as follows: Chapter 2 describes the experimental study and results obtained. Chapter 3 describes the procedure used to obtain the stress and strain fields that are subsequently used in chapter 4 and 7 for the micromechanics based finite element investigation. Chapter 5 examines the effect of ply angle and its influence on the in plane failure mode. Chapter 6 describes the procedure used to obtain the in-situ shear response of the polymer matrix used in the composites. Chapter 8 includes a summary of the contribution from this thesis, with recommendation for future investigations.

## 1.2. Figures
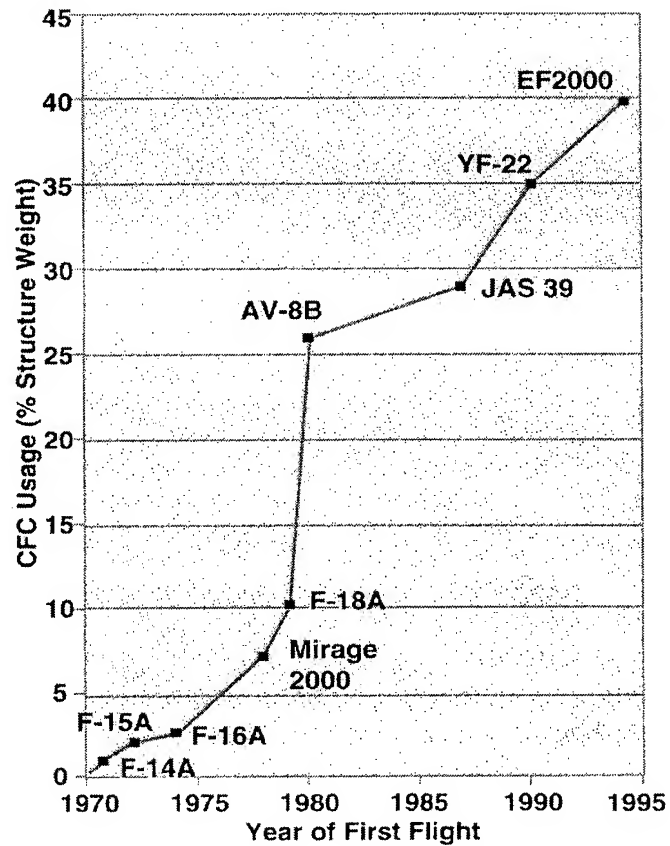


Figure 1.1 CFC Application trend (Ref. 1.2)
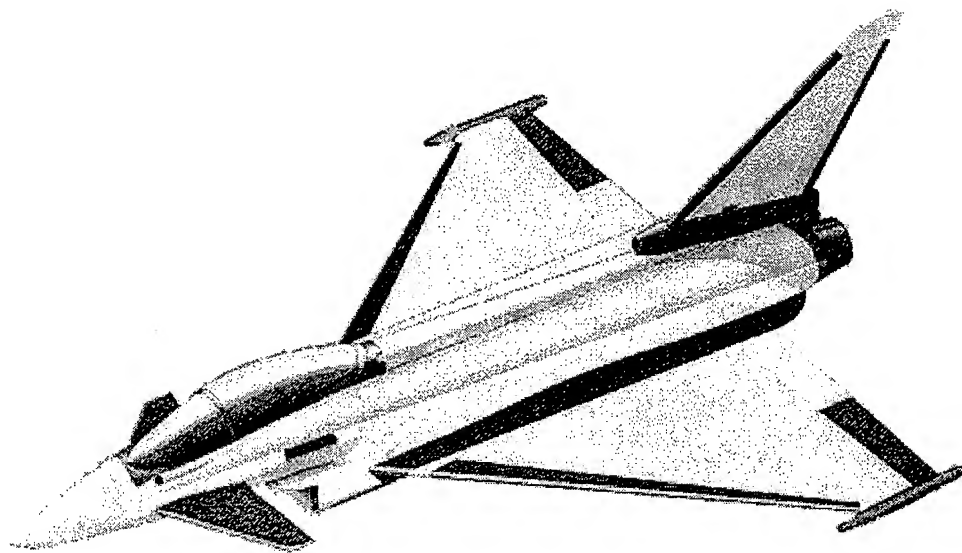


Figure 1.2 CFC Application in EuroFighterAircraft (White area, EFA Web Site)
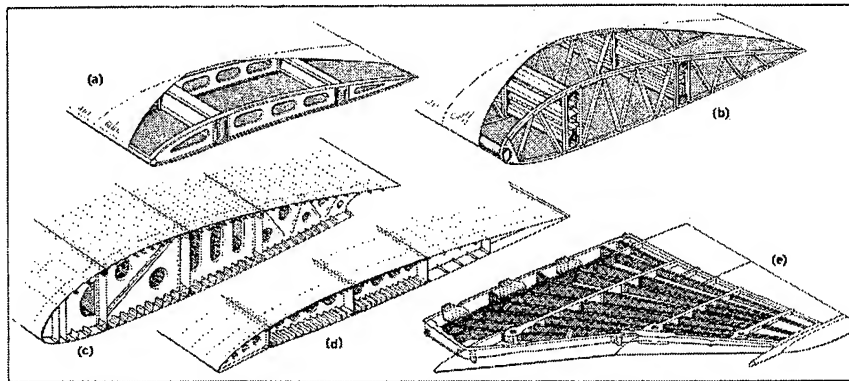
**Figure 1.3 Evolution of wing structure in chronological order (a)-(e) (Ref. 1.2)**
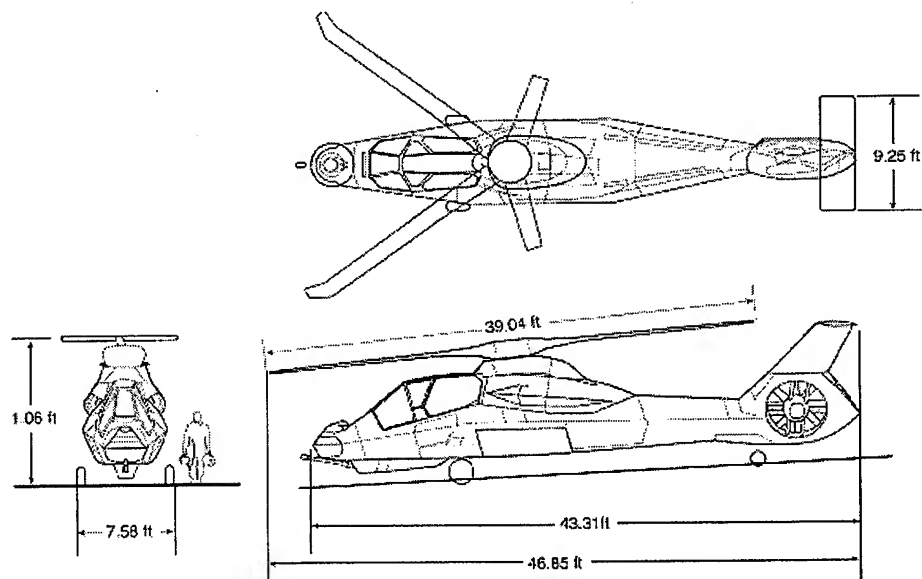


**Figure 1.4 RAH66 Comanche (Ref. 1.5)**
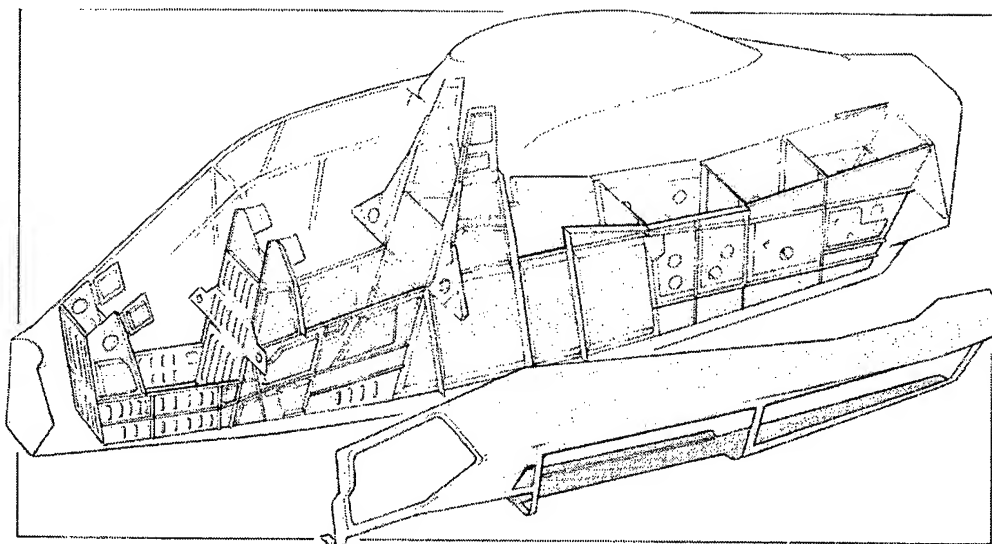
**Figure 1.5 CFC Fuselage member of RAH66 (Ref. 1.2)**

## 1.3. References

1. Issac M. Daniel and Ori Ishai, 1994, "Engineering Mechanics of Composite materials", Oxford University Press.

2. Ray Whitford, Fundamentals of Fighter Design, 1999,"Air International", Key Publishing

3. NASA Langley Research Center, 1984, "Tough Composite Materials: Recent Developments", Noyes Publication.

4. Lawrence H. Van Vlack, 1985, "Elements of Material Science and Engineering", Addison-Wesley Publishing Company

5. http://www.boeing.com

6. http://eurofighter-typhoon.com/index2/index2.htm

7. http://www.scaled.com

# CHAPTER 2

## FAILURE MECHANISMS OF MULTIDIRECTIONAL LAMINATES UNDER ROOM & ELEVATED TEMPERATURE

### 2.1. Introduction

For structural applications, polymer based fibrous composite materials possess several favorable attributes when compared to other traditional materials such as metals. A high specific stiffness is one attribute that favors applications in the aerospace industry. Because of their complex microstructure, these materials exhibit a variety of failure mechanisms when subjected to mechanical and thermal loads. Understanding these mechanisms and developing micromechanics based modeling capability have been subject areas that have received a considerable amount of attention in the recent past. In the present chapter, the results of an experimental investigation into the failure mechanisms of notched fibrous composite laminated plates will be presented. Plates containing a centrally located circular hole were subjected to planar compressive loads, both biaxial and uniaxial, under room (25° C) and elevated temperature (200° C).

The motivation for this study stemmed from a problem commonly occurring in aerospace applications where flat plates and panels containing cutouts have to be designed to carry a certain amount of mechanical load under various

operational temperatures. An important question that arises in this process is the identification of the dominant failure mechanism at a given temperature and loading conditions, which is activated during service conditions. A secondary, but equally important question is the amount of stiffness and strength degradation in terms of the failure initiation in the presence of an elevated temperature environment.

In this chapter, details of the experiments and the test procedure will be presented. Next, the results obtained from the different types of laminates will be described, with important observations deduced from the tests to ascertain the laminate residual stiffness properties as well as a discussion of the effect of the environment on the observed failure mode. Finally, remarks on how the failure characteristics are related to the lay-up and environment will be followed.

## 2.2. Test Specimens

As pointed out in several papers (See Khamseh & Waas, [Ref. 2.10], difficulties associated with stress concentrations are encountered in the design of a cruciform shaped planar specimen for in-plane biaxial loading, in so far as achieving failure in the center of the specimen is concerned. In order to select the size of the specimen, a model of the notched laminated plate and grips (steel) was generated using the ABAQUS FEA software package. The stress analysis program was used to examine the effect of several specimen geometries on the stress concentrations due to the applied loads. The loads were applied at the boundaries of the loading arms by use of displacement constraints. Eight noded parabolic

plane stress elements were used to model the plate material and steel grips. Ply properties were entered from which ABAQUS calculates the equivalent plane stress constants using classical lamination theory. It was concluded from the results that a cruciform configuration matching the dimensions given in Figure 2.1, was the desirable specimen shape. The word 'desirable' is used to refer to a stress state for which an in-plane region in the interior of the specimen (shown as the cross hatched area in Figure 2.1) is not influenced by the effects of the far field edges (i.e., edge curvatures identified as $R_C$ in Figure 2.1) of the plate due to the loading.

Specimen configurations corresponding to several values of $R_C$ were studied (Khamseh & Waas, [Ref. 2.11]) using the FEA prior to arriving at a 'optimum' value of $R_C$ based on the condition that the specimen with a hole does not contain effects associated with the stress concentration at the hole interfering with nonuniformities in the stress field generated on account of the edge curvatures. For the composite plate we studied, this 'working' area translated into a 6.35-cm (2.5-in.) square region in the middle of the cruciform configuration.

The test specimens were made of graphite / toughened epoxy material containing Hercules IM7 (Intermediate Modulus) fiber and 977-3 toughened epoxy matrix, designed for operation at high temperatures. In Table 2.1, we show the lamina properties, based on data provided by the manufacturer. The stacking sequence for these symmetric laminates were as follows: Cross-Ply $[0/+90]_{12s}$, Angle-Ply $[+60/-60]_{12s}$ and Quasi-Isotropic $[+45/0/-45/90]_{6s}$. In Table 2.2., Laminate material properties, calculated using generalized classical lamination theory(CLT) are listed. The linear elastic plane stress solution that corresponds to

the problem at hand, as given in Lekhnitskii [Ref. 2.1] was used to calculate the stress field corresponding to the uniaxial and equi-biaxial loading. The obtained solution was next verified with the strain data (far field and near the hole edge) that was measured in the room temperature test for each laminate type. Such a check yielded good agreement between test data and the 2D-elasticity solution. Details of the elasticity solution are given in chapter 3.

The inplane dimensions of the test specimens are given in Figure 2.1. The thickness of the laminates was 0.635 cm (0.25 in.) with a 0.013 cm (0.005 in.) tolerance. In the center of the steel grips, a 0.724 cm (0.285 in.) channel, 3.048 cm (1.200 in.) in depth, was machined along the length of the grip. A specimen arm sat in this channel, bonded to the walls of the channel with the use of Devcon® brand plastic steel putty adhesive, treated with release agent in order to allow for ease of separation of the two materials at the end of an experiment. More importantly, the Devcon® putty acted as an interface between the specimen edge and the grip surface on which the specimen 'sat' effectively smoothening out the interface surface irregularities between the two materials and ensuring a smooth load transfer. To ensure proper alignment of the specimen inside the channel (i.e., ensuring reasonably centered seating of the specimen inside the channel), metal shim plates of various thickness were added to both sides of the specimen to minimize any gap inside the channel.

## 2.3. Loading Apparatus

The biaxial loading frame has four load actuators capable of exerting tensile / compressive loads of 222 kN (50,000 lbf) when mated to a 20.7 MPa (3000 psi) hydraulic power supply. It should be noted that each of the actuators can be programmed to operate in a load or displacement feedback control mode (via the use of a load cell or displacement transducer) fully independent of the other three cylinders, thereby allowing for both uniaxial as well as biaxial tests. Two load cells were used in the system, one along each loading axis, each rated for a magnitude of 222 kN (50,000 lbf) in tension and compression.

The loaded ends of the specimen were clamped for uniaxial and biaxial loading cases. The 2.00 in. long clamp holders contained grooves of 0.2 in. in depth and 0.3 in. in width. The test specimen was inserted into the grooves and the remaining gap in the groove was taken up by mild steel shims. The center of the holders were marked and aligned with the center of the specimens and loading apparatus in order to ensure a uniform symmetric loading. A ball joint, positioned along the loaded axis, was included to minimize bending effects.

## 2.4. Radiation Heater Setup

To perform a compression test at the elevated temperature, a feedback-controlled radiation-heating element with an insulation tunnel (Figure 2.3) was designed and used. Special strain gages for high temperature (mounted with high temperature glue and lead wire insulated for thermal protection) were used for the test. To ensure a steady temperature in the enclosed test chamber, four

14

locations in the test chamber were used to monitor temperature. The heating rate was limited to be very slow (2°C / min). In addition, thermocouple gages placed inside the specimen cutout edge and on the specimen surface were used to verify that the specimen temperature was fairly even (less than 2°C change from location to location). The load cell and the loading frame were cooled by circulating water through a copper pipe wrapped around both parts. The maximum temperature of the tests was limited to 200°C (392°F), which was the manufacturer specified limit of the strain gage.

## 2.5. Data Acquisition

A 50,000 lbf load cell was used to obtain a load time history for the far field applied load. Surface strain measurements at various locations on the specimen were recorded with strain gages. Strain gages were mounted along the edges of the hole, as well as in the corresponding far field region. A set of two additional strain gages were mounted inside the hole, along the wall thickness, in order to record changes in strain in the out of plane (through the thickness) direction, revealing failure initiation (Figure 2.4). Strain gage readings, along with load cell readings were monitored & recorded using a commercial data analysis software package (LabTech® Notebook) via an analog to digital (A/D) converter. The data sampling rate was 5 samples / sec at the loading rate of 0.0001 inch / sec. The general arrangement of test setup is shown in Figure 2.5.

15

## 2.6. Test Procedure

The 48 ply composites were tested under uniaxial and 1:1 (in far-field displacement) biaxial loading at both room temperature and 200°C in order to understand the failure mechanisms and how they are affected by temperature.

The catastrophic nature of the failure in composites and the additional limitation placed upon the visual investigation of failure initiation and progression suggested a displacement-controlled mode for the tests (as opposed to the load control). This facilitates examination of specimens loaded to initial (local) failure but recovered prior to global failure in a displacement feedback control mode.

Each opposing pair of pistons was programmed to move a certain distance in a specified time interval. Preliminary results indicated that a rate of 0.381-cm (0.15 in.) in 25 minutes (0.0001 in. / sec) for piston travel would assure a quasi-static test. This resulted in a far field strain rate of approximately 17 $\mu\varepsilon$ /sec (cross ply), 14 $\mu\varepsilon$ /sec (angle ply) and 19 $\mu\varepsilon$ /sec (quasi-isotropic). The rate is reverse calculated from uniaxial strain measurement. The influence of hole size on the failure mode had been established and verified before (Khamseh and Waas, [Ref. 2.10-11]). Therefore, in the present study one hole size (0.5 in. Diameter) was chosen for all specimens.

Each test consists of loading a particular type of laminate until global failure first, to estimate the ultimate strength of the specimen. This information is used subsequently to aid in unloading specimens that have failure initiated but not reached their ultimate load carrying capacity. A sudden nonlinear (with respect

16

to a far-field load component) increase in strain inside the hole (strain gage placed through the thickness on the hole edge) indicates that there is a failure initiation at the hole edge of the specimen, even though there may not be a sign of global failure of the specimen.

During the heating cycle, the loading piston was separated to ensure free thermal stress heating, and thermal strain was measured and recorded to compare with actual strain due to loading. Typical strain gage test data plotted as a function of load is shown in Figure 2.6. For a cross ply laminated loaded in equibiaxial compression at the room temperature. As expected, the response is "symmetric" since the cross ply laminate has equal stiffness along the loading direction. Detecting localized failure was done by following the through thickness strain, as shown in Figure 2.7 for a uniaxial cross ply specimen at elevated temperature. Test was stopped as soon as any nonlinear strain increase was observed. These unloaded specimens were sectioned and observed under an optical microscope in order to examine the failure initiating mechanisms (kink banding, micro-buckling, fiber/matrix interface cracking, matrix cracking etc.). Both the in-plane and out-of-plane views of the failed region were examined and digital photomicrographs were next acquired. Same procedure was used for the rest of specimens. Typical experimental results are shown in Figure 2.8 and 2.9.

## 2.7. Room Temperature Uni & Biaxial Compression of 48 Ply Notched Laminates

Cross ply laminates show the typical kink banding failure mode (also identified before by a number of researchers) [Ref. 2.2-2.12] at around a far field stress of 44 Ksi (Table 2.3). Failure initiates in the zero plies, at the hole edge, and propagates in a direction that is perpendicular to the direction of applied far-field load. Both inplane and out-of-plane kink banding occur in the zero plies. In Figure 2.10, a typical view of the out-of-plane kink band is shown. The surface strain at the hole edge in the direction of applied load at failure initiation is $7,500\mu\varepsilon$ and the corresponding far field strain is approximately $3,000\mu\varepsilon$. When the damage propagates in the form of kink bands, the fiber/matrix interface is completely severed in a number of fibers within the kink bands. In addition, the kink banding also introduces interlaminar separation between the kinked ply and the neighboring 90° plies.

The failure of the angle ply specimens subjected to the same type of loading is quite different. As indicated in Figure 2.12, the angle ply laminates when stressed in the Y-direction, fail by a mechanism of fiber matrix shearing. The failure is sudden so that the initiation and final failure occur almost at the same time. Because the strains near the hole edge are much larger than elsewhere, the failure initiates at the hole edge and traverses along the 60° fiber angle (the crack runs through the matrix between the fibers). It appears that the -60° fibers running at an angle to the crack path do not provide the requisite crack bridging toughness

to arrest the crack, so that once initiated the specimen is "split" cleanly along a line at 60° (Table 2.4.).

Quasi-Isotropic laminate specimens fail by both inplane shear failure and kink banding simultaneously (Figure 2.13). Whether kink formation in the 0° plies or fiber/matrix interface failure in the angle plies is dominant is determined by the specimen characteristics (stacking sequence, individual imperfection, etc.) and the in-situ shear response of the matrix. This aspect will be discussed later in this thesis (chapter 7). In the present case, shear failure along the fiber/matrix interface led to catastrophic failure throughout the tests. Although there was evidence of kink band formation observed after the test, the fiber/matrix interfacial failure in the 45° degree plies was seen to be the dominant event that propagates the failure starting at the hole edge (Table 2.5).

The main difference in response of the laminates between the remote uniaxial and the remote equibiaxial displacement loading is not in the mechanism of failure but the magnitude of far-field loading necessary to achieve failure initiation. A remote equibiaxial compression loading tends to relieve the compressive stress gradient away from the hole, as compared with the uniaxial loading (see chapter 3). For the cross ply case, this combined effect due to biaxial loading does not show much of an effect on the magnitude of the failure initiation stress, because the failure mechanism is initiated by a fiber instability. However, the angled ply and the quasi-isotropic specimen show different far field failure initiation loads because the failure mechanism is governed by the state of shear at the matrix, which is a strong function of ply angle and overall stacking.

19

For the case of cross ply laminates, since there are only $0^o$ / $90^o$ plies, failure initiation occurs by kink banding in the $0^o$ plies, starting from the hole edge at a position that is perpendicular to the direction of loading. Ideally, both kink bands (on either side of the hole) should happen at the same time, but due to material non-homogeneity or a slight perturbation of the symmetry of loading, one of the two kink bands form first, then followed by the other. The kink band formation leads to interlaminar cracking between the kinked ply and the adjacent 90° ply.

For a angled ply laminates, failure initiates along fiber/matrix angle (60°) direction. Once initiated, the failure propagates through the thickness catastrophically, which shows the fibers in the opposite angle can not withstand the energy release along the failure plane.

A quasi-isotropic laminate shows competition between shear failure in the +45/-45 lamina and the 0/90 lamina. The experimental results show that quasi-isotropic laminate fail by interfacial failure along the ±45° plies, however it is postulated that this mechanism is triggered by the kink banding in the zero plies.

## 2.8. Elevated Temperature

At elevated temperature, a new parameter emerges to influence the mechanism of failure. Because the matrix properties undergo changes in mechanical properties (chapter 6) than the fiber as temperature increases, the matrix sensitive mechanical properties of laminates such as transverse modulus and shear modulus are highly affected at the elevated temperature. This behavior is closely related with the change in matrix property associated with the shear

stress vs. shear strain response, as will become evident later in chapter 6. Furthermore, due to the mismatch in the coefficients of thermal expansion, the nature of the fiber / matrix interface is also changed. In addition, the matrix rich region between plies that control the interlaminar strength is also affected.

As in the room temperature tests, failure initiation is sensed by a sudden increase in the through thickness (out of plane mode) strains, which allows the unloading of a specimen for post-failure microscopic examination of regions near the hole edge.

Cross ply laminates show extensive kink formation just as in the room temperature case. Compared to the room temperature case, failure occurs at a lower load (See Table 2.3). Again, the kink banding initiates at the hole edge and propagates in a direction perpendicular to the direction of loading (Figure 2.10). Noticeably, the out of plane failure is very extensive. This observation may point to the reduced interlaminar strength at elevated temperature, for the reasons discussed above. Figure 2.11 shows the appearance of the kink bands when viewed in the through the thickness direction.

In the case of the angle ply laminates, the drop in failure load at high temperature is not as drastic as the cross ply laminates (Table 2.4), but the maximum strain at the hole is reduced to about half when compared to the room temperature case. An examination of the failed angle ply specimens reveal that the fiber / matrix interfacial strength is important in controlling the failure (Figure 2.12).

Quasi-Isotropic laminates (Table 2.5) show a combination of the different failure modes, however, fiber/matrix shear failure is still the dominant failure

mechanism. A band of damage consistently propagates along the +45 / -45 line from 0° hole edge, in the form of interfacial fiber/matrix cracking indicating that this is the form of energy release at the failure.

## 2.9. Concluding Remarks

The experimental results of a series of uniaxial and equibiaxial inplane compressive loading experiments on notched composite laminated plates under room temperature and elevated temperature conditions were investigated in this chapter. Three types of 48 ply graphite/epoxy composites were studied in order to understand their compressive failure mechanisms.

The laminate stacking sequence was selectively designed to isolate the different failure mechanisms that operate in angle plies and plies oriented in the loading direction. In specimens containing plies along the direction of the load (cross ply), uniaxial compression leads to fiber kink banding. This same scenario persists at both room and elevated temperature.

The angle ply specimens show failure along the fiber / matrix interface. The failure persists either at $+\theta$ or $-\theta$ angle or both. Fibers across the line of failure were broken due to the large amount of energy released as the interfacial crack propagates rapidly. At elevated temperature, the same failure mechanisms persist, but at different magnitudes of far-field loading. Under equibiaxial compression, the remote load to initiate failure at a given temperature is higher than the uniaxial case, whereas for cross ply laminates there is no appreciable increase in load between the uniaxial and biaxial cases at a given temperature.

Further, for a given loading (uniaxial or biaxial), the failure initiation load decreases for cross ply laminates, whereas there is not a noticeable decrease for the angle ply laminates.

The failure of the quasi-isotropic laminates (Figure 2.13) involves a combination of kink banding and fiber/matrix interfacial failure, although in every case, the interfacial failure/matrix failure is dominant in releasing the stored energy at failure. The magnitude of remote failure initiation loads between the loading cases at a given temperature as a function of temperature for a given loading case (uniaxial or biaxial) is very much like the angle ply laminates, although the difference were much larger for the angle ply laminates

From test series of test results, and the loads reported in Table 2.3 through Table 2.5, the correlation is now evident. This can be seen by comparison of the room temperature failure initiation loads with the corresponding loads at high temperature. In cross ply laminates there is a noticeable decrease in the failure initiation loads between room and high temperature whereas such a reduction is hardly noticeable in the angle ply and quasi-isotropic laminates. This observation shows that the mechanism of failure initiation in cross ply laminates (fiber instability followed by kink banding) is strongly influenced by the matrix, since the mechanical properties of the matrix has been degraded at the high temperature (to be discussed in chapter 6, later). On the other hand, the mechanism of failure initiation in angle ply laminates and quasi-isotropic laminates is not affected as much as cross ply laminates by temperature.

On the other hand, at a given temperature, biaxial loading reduces the failure initiation load for cross ply laminates, whereas, for the angle ply and quasi-

isotropic laminates this trend is reversed. These findings are explained later, in conjunction with a micromechanics based finite element analysis (chapter 7) and a simple stress analysis (chapter 3).

## 2.10. Tables and Figures

| Material | $E_{11}$ (Msi) | $E_{22}$ (Msi) | $G_{12}$ (Msi) | $\nu_{12}$ | Thickness (in) |
|---|---|---|---|---|---|
| IM7 / 977-3 Epoxy | 23.5 | 1.21 | 0.72 | 0.30 | 0.0052 |
| IM7 Fiber | 42 | | | 0.25 | 2.756 E-04 |
| 977-3 Epoxy | 0.7 | | | 0.34 | 2.444 E-04 |

**Table 2.1 Zero ply material properties of the 48 ply graphite / 977- 3 epoxy composites**

| Laminate Type | Stacking Sequence | $E_{xx}$ (Msi) | $E_{yy}$(Msi) | $G_{xy}$(Msi) | $\nu_{xy}$ |
|---|---|---|---|---|---|
| Quasi-isotropic | $[+45/0/-45/90]_{6s}$ | 8.828 | 8.828 | 3.372 | 0.309 |
| Cross-Ply | $[0 / 90]_{12s}$ | 12.401 | 12.404 | 0.7119 | 0.029 |
| Angle-Ply | $[+60 / -60]_{12s}$ | 1.492 | 7.383 | 4.698 | 0.309 |

**Table 2.2 Laminate material properties as determined from classical lamination theory (CLT) using the properties from table 2.1**

| Specimen Type | Temperature (C°) | Loading Type | Failure initiation load (Ksi) | Max. Hole Strain (με) | Failure Mode |
|---|---|---|---|---|---|
| Cross-Ply | 25 | Uniaxial | 44 | 7,500 | Kink at 0° edge |
| Cross-Ply | 200 | Uniaxial | 19 | 2,700 | Kink at 0° edge |
| Cross-Ply | 25 | Biaxial | 37 | 6,600 | Kink in 0, 90° edge |
| Cross-Ply | 200 | Biaxial | 18 | 2,080 | Kink in 0, 90° edge |

**Table 2.3. Cross Ply Experimental Data**

| Specimen Type | Temperature (C°) | Loading Type | Failure initiation load (Ksi) | Max. Hole Strain (με) | Failure Mode |
|---|---|---|---|---|---|
| Angle-Ply | 25 | Uniaxial | 22.5 | 6,600 | Shear Failure (+60 / -60) |
| Angle-Ply | 200 | Uniaxial | 22 | 3,284 | Shear Failure (+60 / -60) |
| Angle-Ply | 25 | Biaxial | 35 | 4,500 | Shear Failure (+60 / -60) |
| Angle-Ply | 200 | Biaxial | 31 | 2,200 | Shear Failure (+60 / -60) |

**Table 2.4 Angle Ply Experimental Data**

| Specimen Type | Temperature (C°) | Loading Type | Failure initiation load (Ksi) | Max. Hole Strain (µε) | Failure Mode |
|---|---|---|---|---|---|
| Quasi isotropic | 25 | Uniaxial | 21 | 6,600 | Shear Failure (+45 / -45) |
| Quasi isotropic | 200 | Uniaxial | 19 | 3,900 | Shear Failure (+45 / -45) |
| Quasi isotropic | 25 | Biaxial | 26 | 4,443 | Shear Failure (+45 / -45) |
| Quasi isotropic | 200 | Biaxial | 24 | 2,872 | Shear Failure (+45 / -45) |

**Table 2.5 Quasi-Isotropic Experimental Data**

Figure 2.1 Specimens
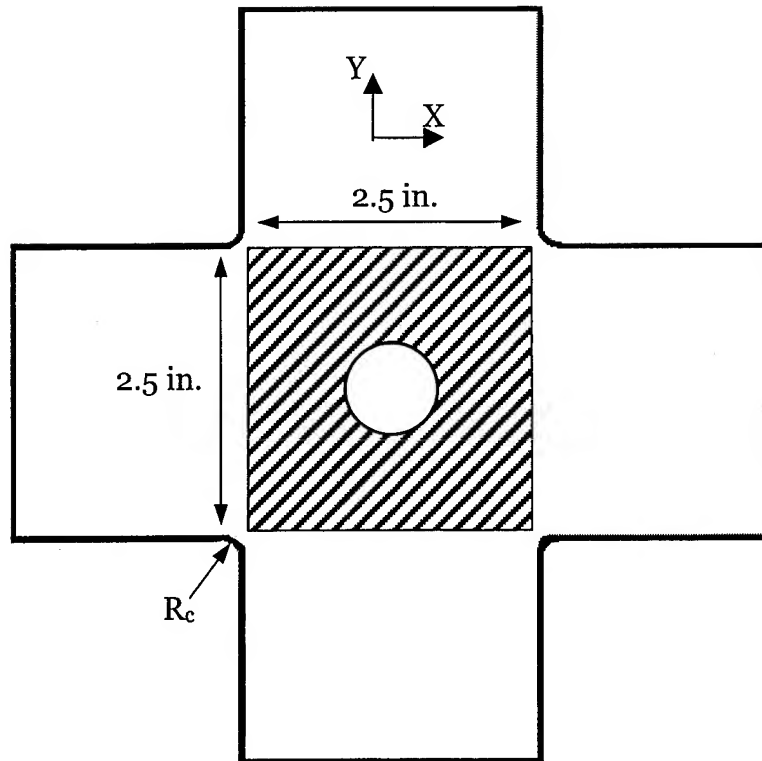
- 5.5" x 5.5" Cruiciform Specimens, $R_c$ = 0.25
- HERCULES IM-7/977-3 (Toughened Epoxy Resin)
- 48 Ply Plate, 0.5" Hole Diameter, 0.25" thickness
- Cross-Ply : $(0/90)_{12s}$
  Angled Ply : $(+60/-60)_{12s}$
  Quasi-Isotropic : $(+45/0/-45/90)_{6s}$
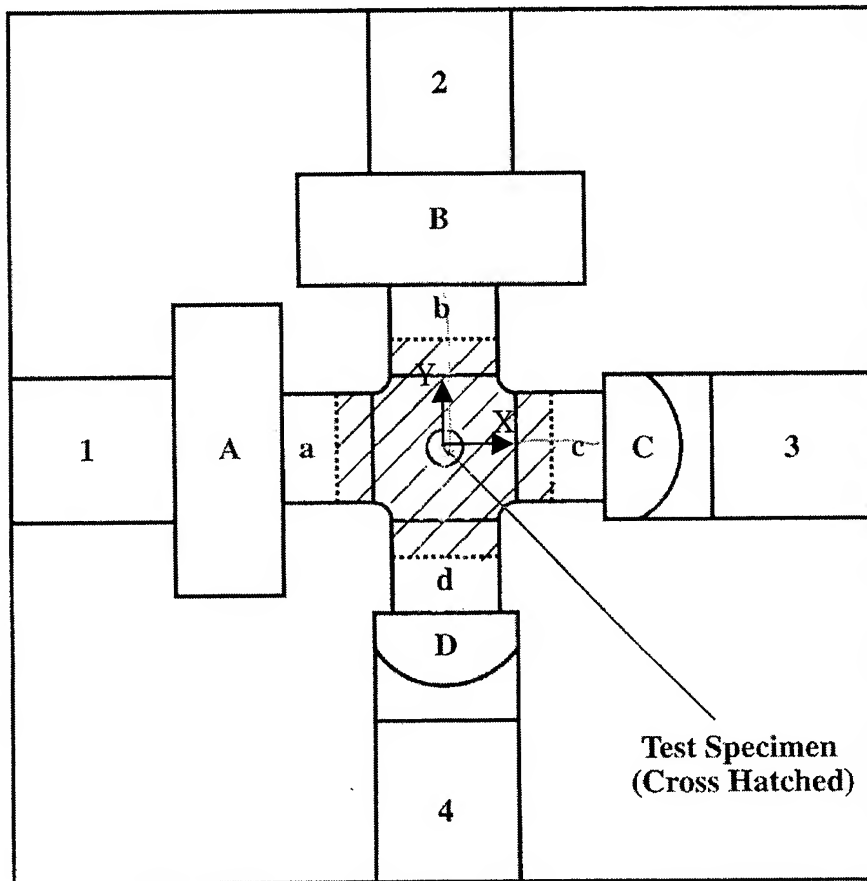
**Figure 2.2 Test Setup**
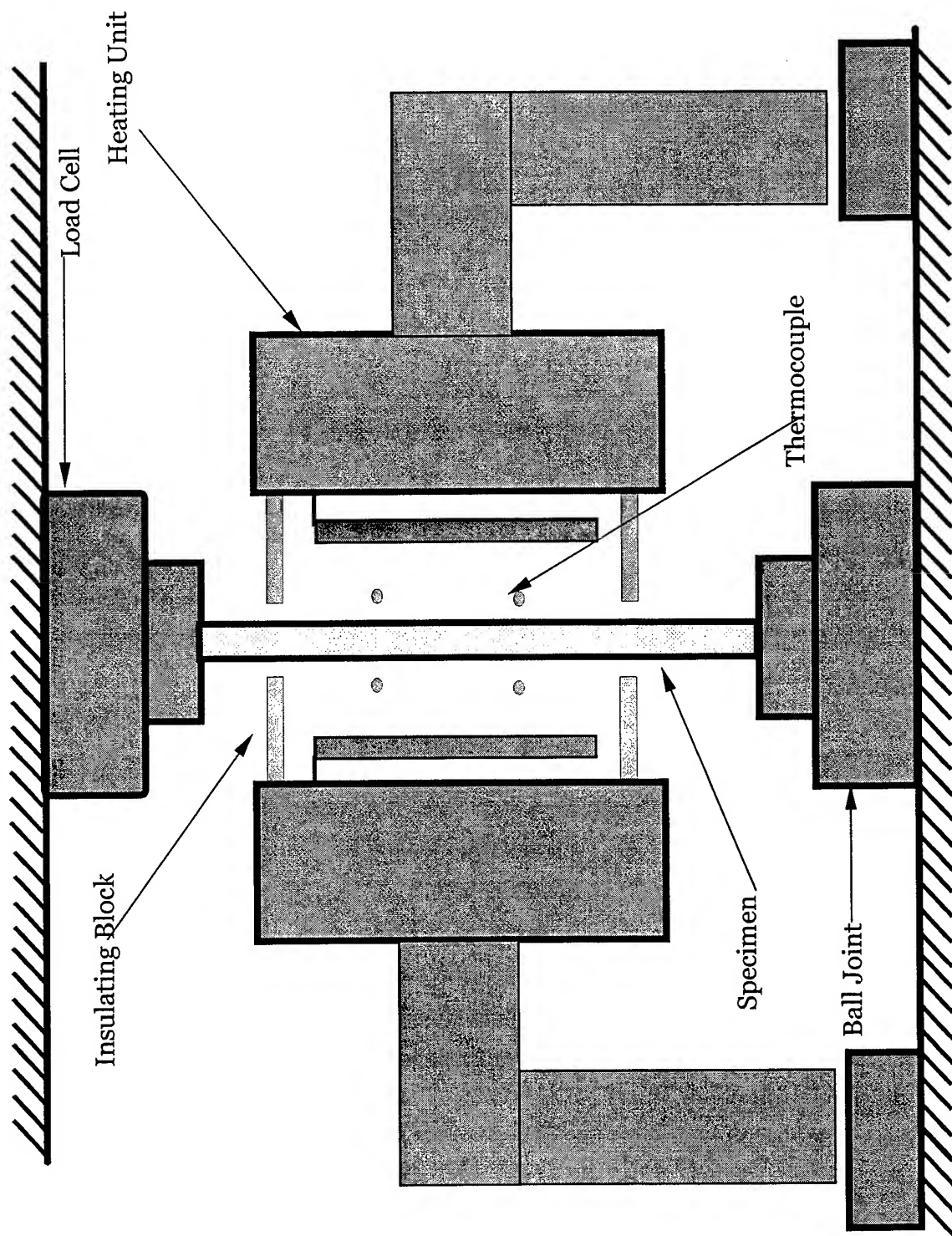
Figure 2.3 Experimental set up : General Arrangement
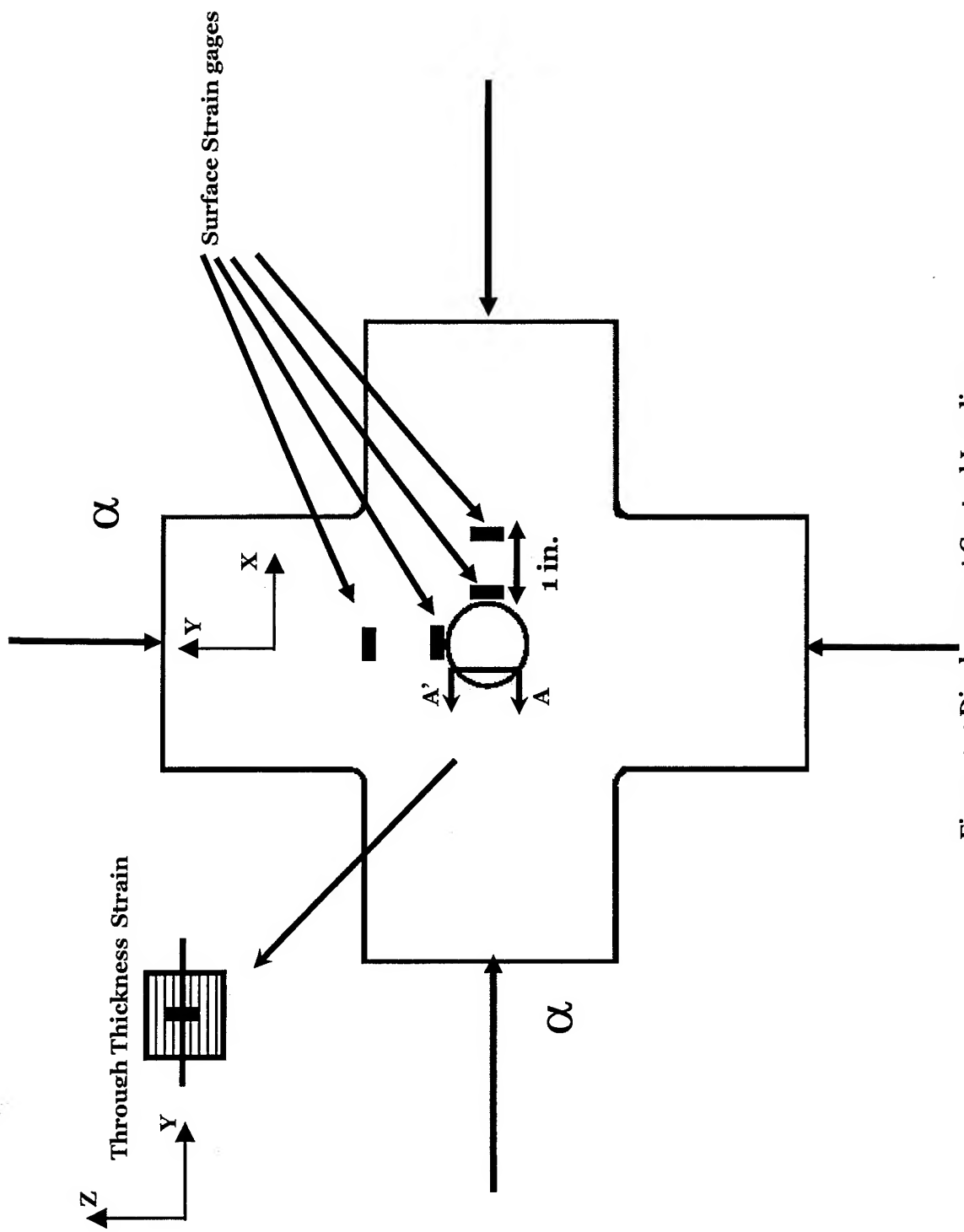
Figure 2.4 Displacement Control Loading

31
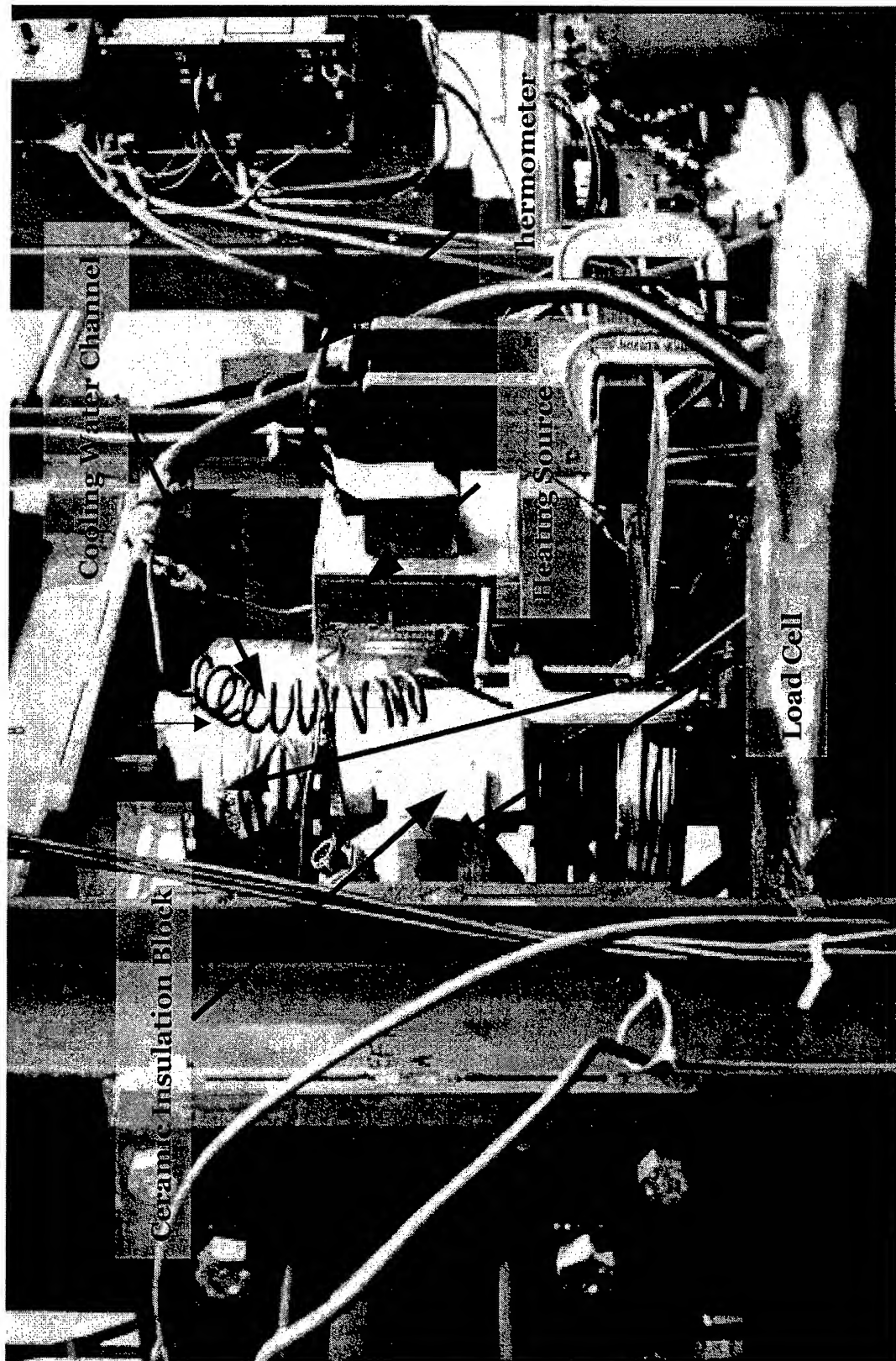
**Figure 2.5 Experiment Setup : Biaxial Loading**

32
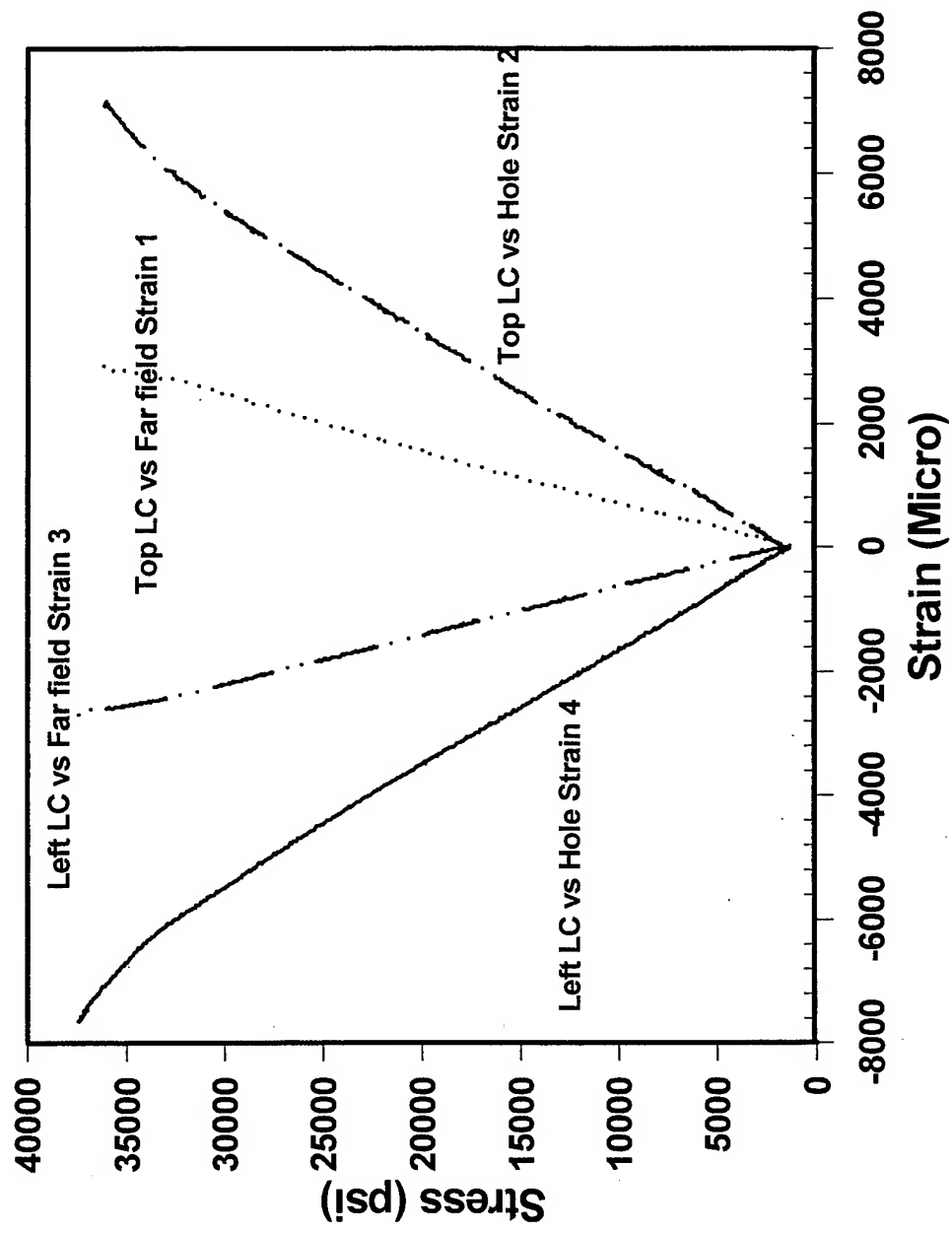
Figure 2.6 Experimental Result for Equibiaxial Displacement Loading (Cross ply)

33
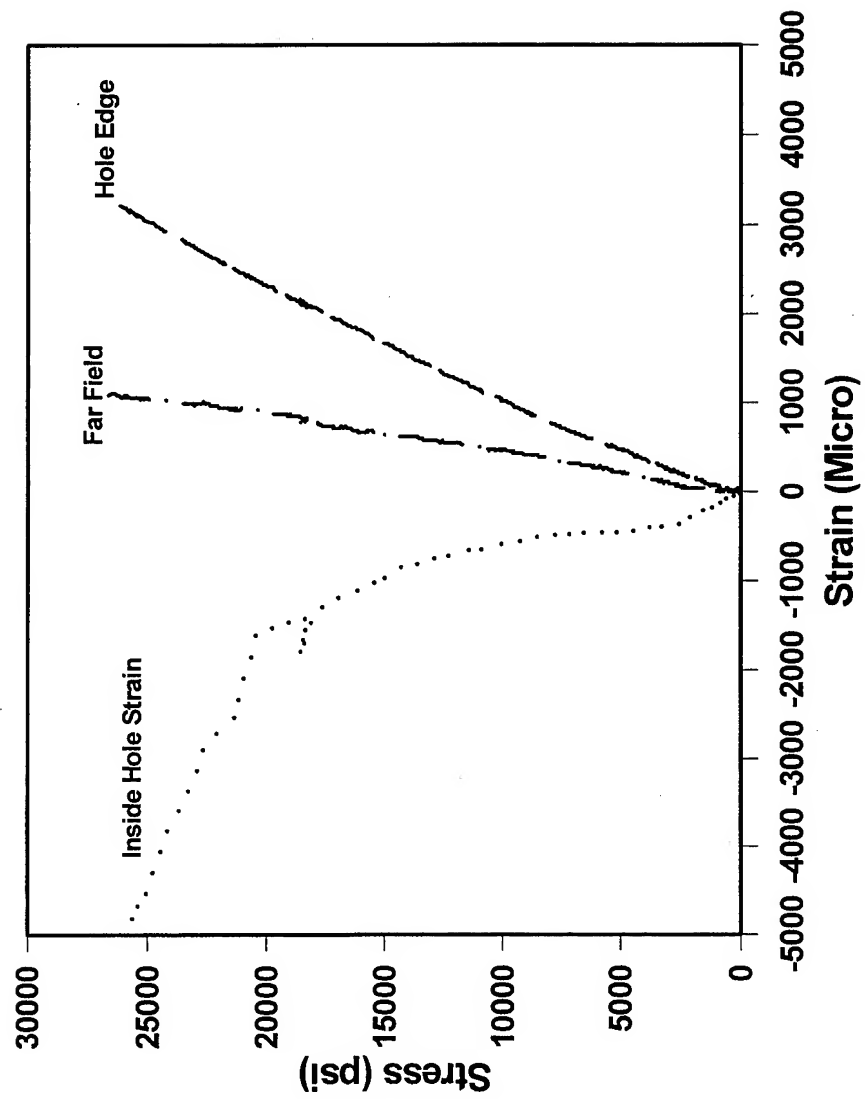
Figure 2.7 Uniaxial Test Result (Cross ply, Elevated Temperature)s

34
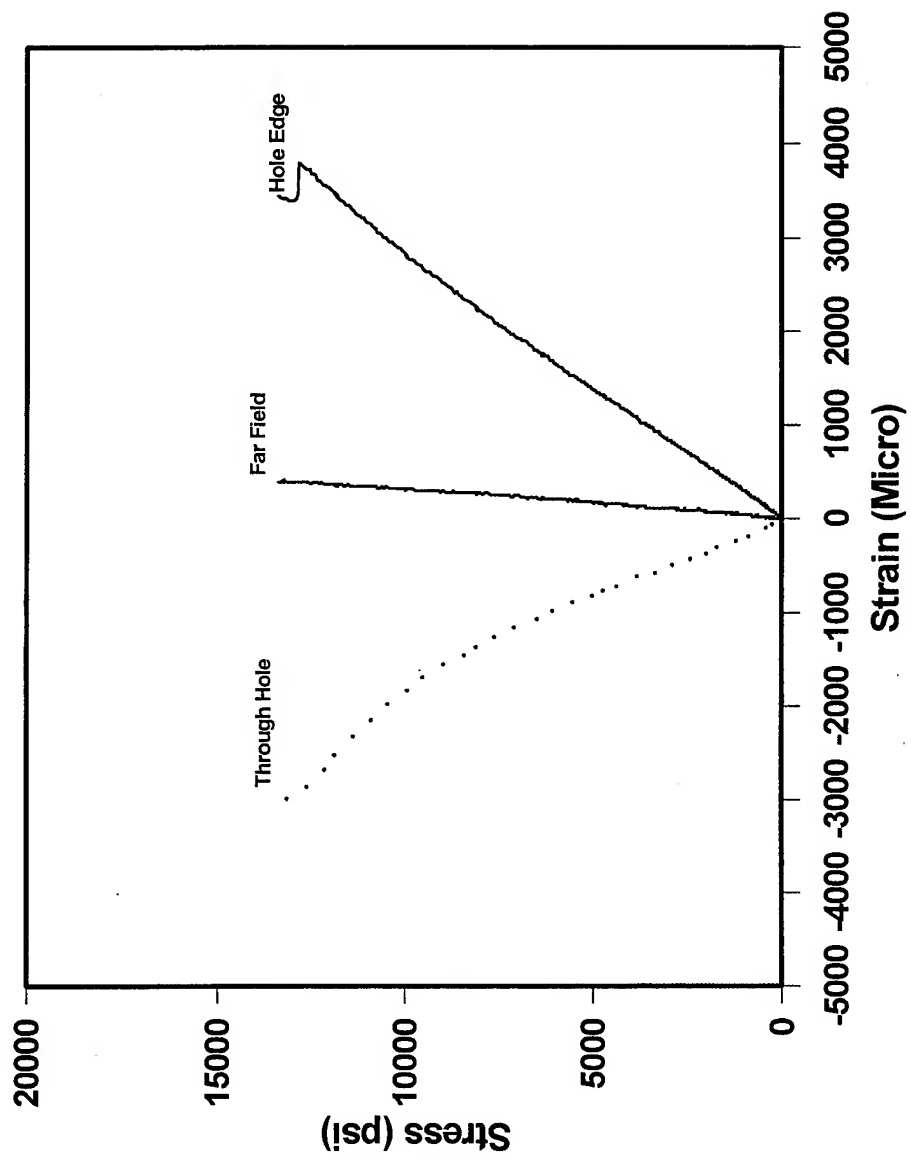
Figure 2.8 Uniaxial Test Result (Angle Ply, Elevated Temperature)

35
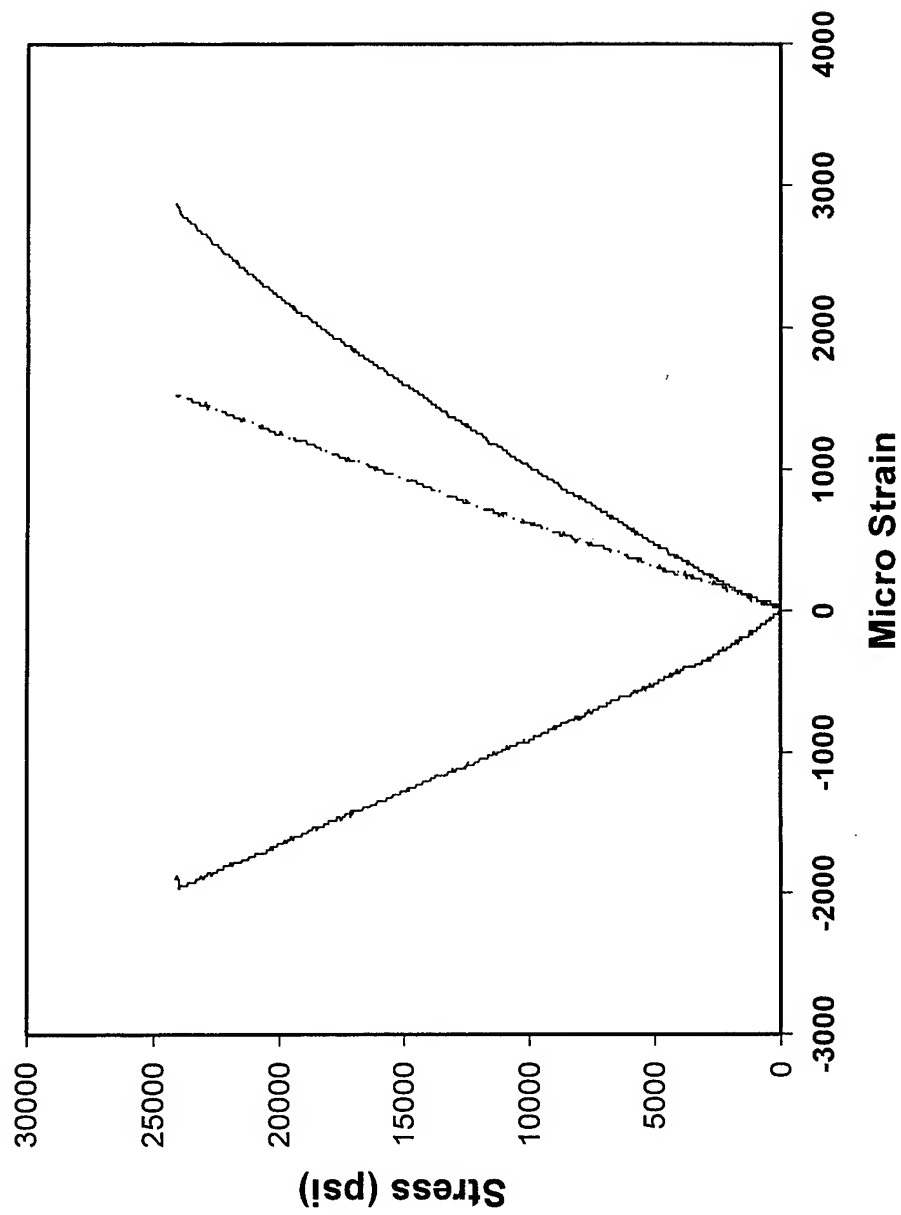
Figure 2.9 Uniaxial Test Result (Quasi-Iso Ply, Elevated Temperature)

36

0.01 in.

Kink Line

A magnified views of a kink band in the typical 0° ply or 90° ply

37
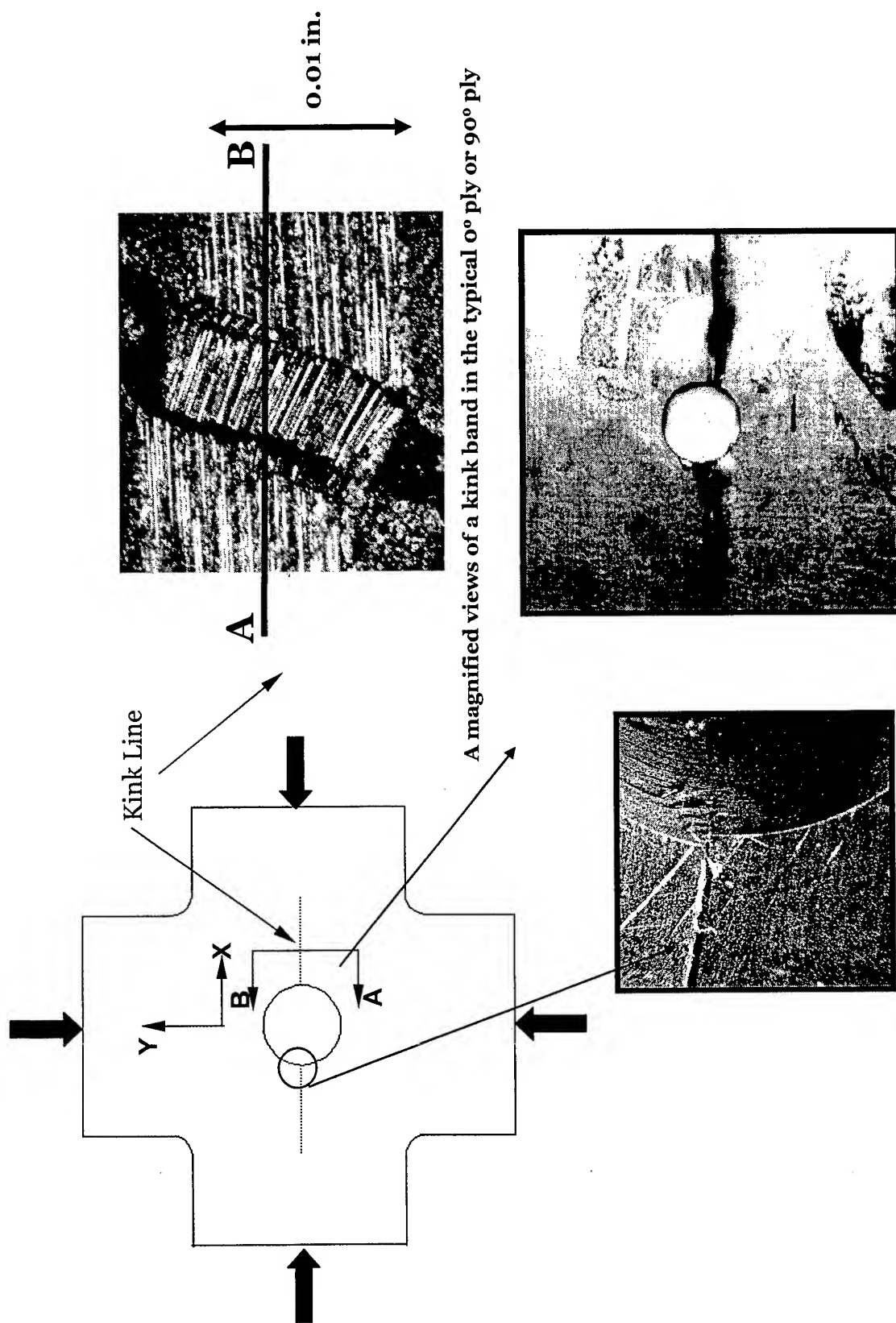
Figure 2.10 Cross-Ply Laminate Failure Mechanism (biaxial, room temperature)

**Center Line**

Z
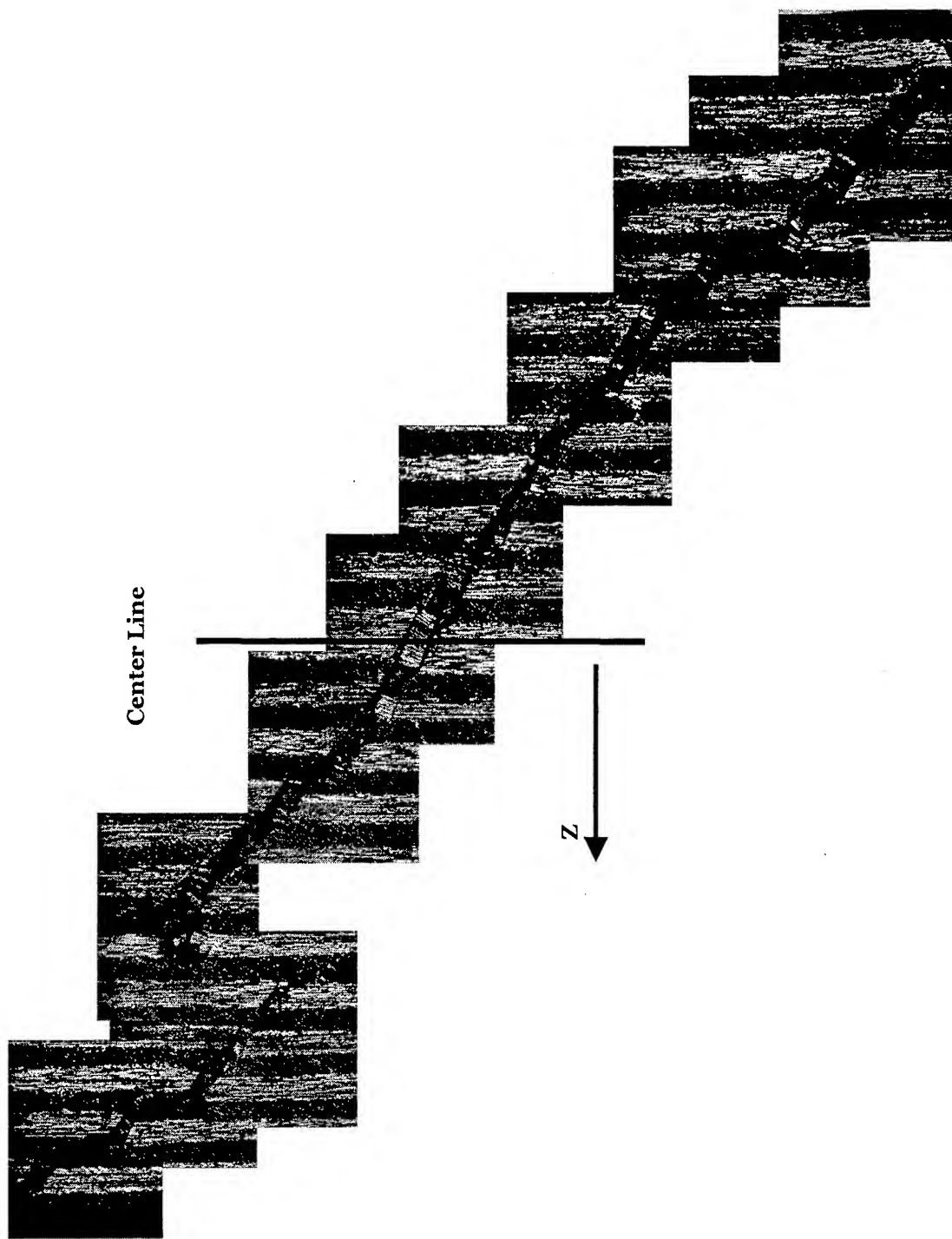
Figure 2.11 Out of Plane Kink Formation (Cross-Ply, elevated temperature, viewed along section AB

38

Shear Crack Splits the Laminate through the thickness

Shear Crack

0.005 in.
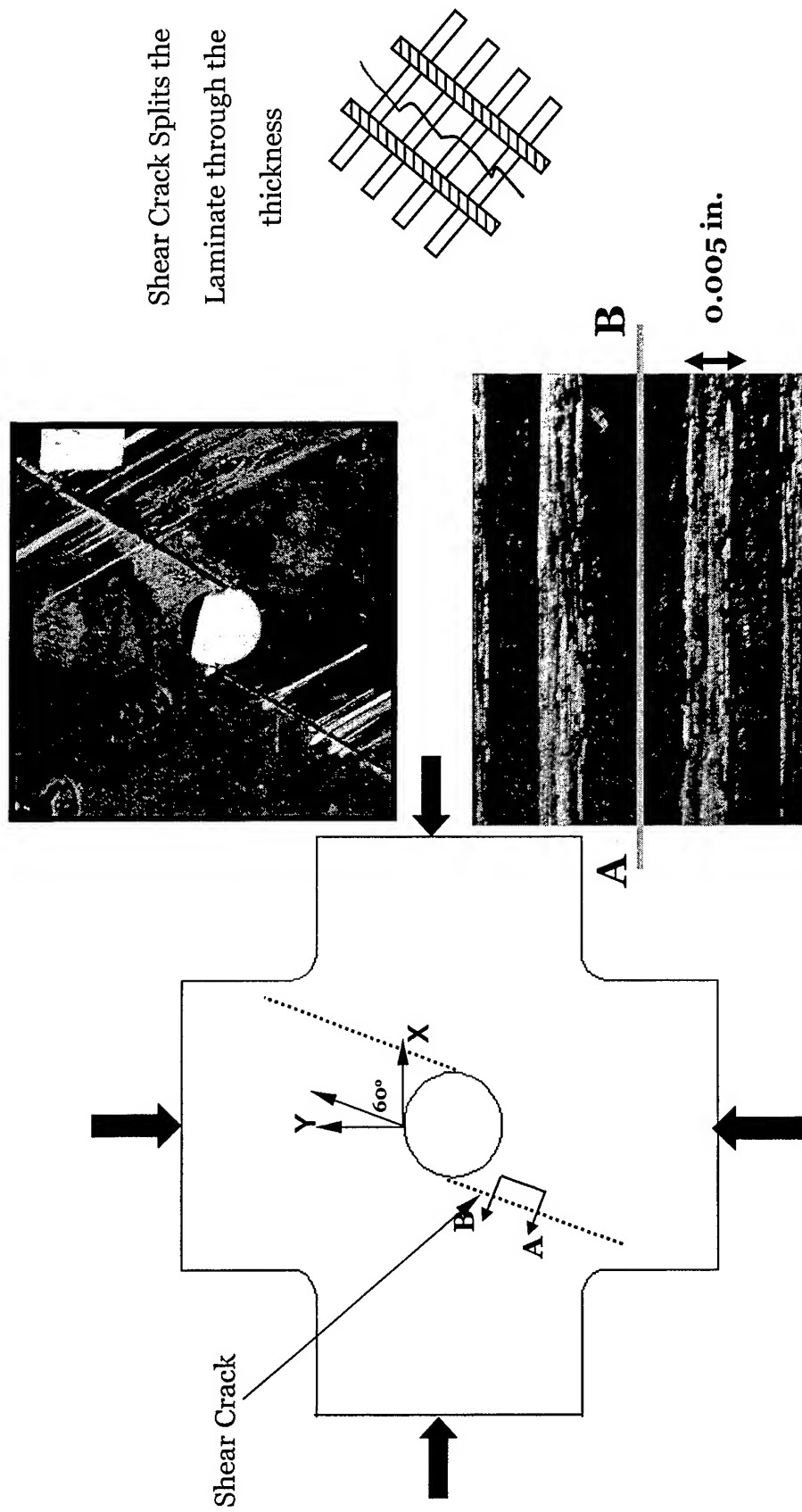
Figure 2.12 Angled Ply Laminate Failure Mechanism (biaxial, room temperature)

39
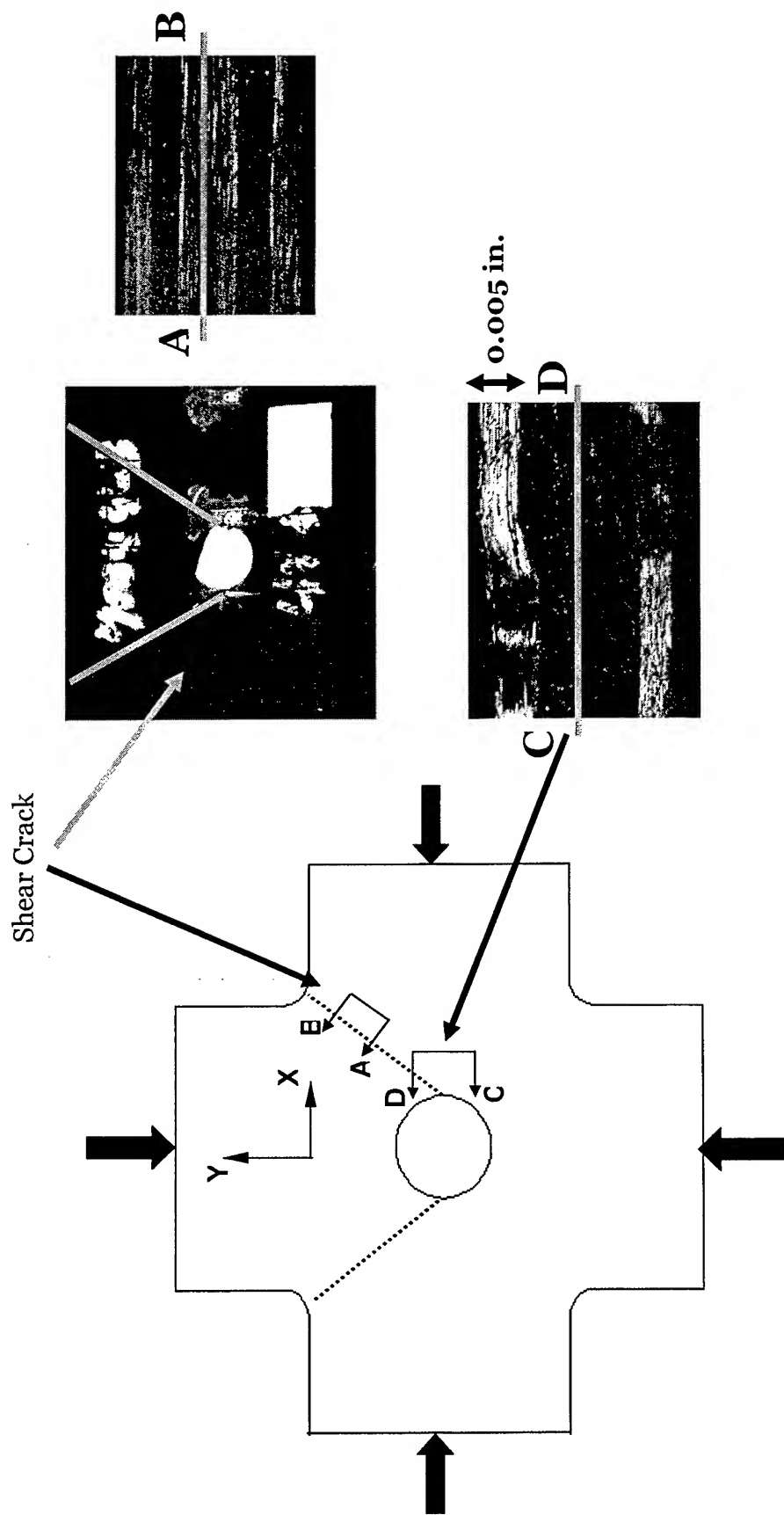
Figure 2.13 Quasi-Isotropic Laminate Failure mechanism (biaxial, room temperature)

40

## 2.11. References

1. Lekhnitskii S., "Theory of Elasticity of an Anisotropic body", Text, Godden-Day, 1968

2. Waas, A. M., and Schultheisz, C. R., 1995, "Compressive failure in Composites, Part II", *Progress in Aerospace Science*, Vol.32, pp. 43 – 78.

3. Starnes, J., Rhodes, M.D. , and Williams, J.G. , 1979, "Effect of Impact Damage and Holes on the Compressive Strength of a Graphite/Epoxy Laminate", *Nondestructive Evaluation and Flaw Criticality for Composite Materials*, edited by R. B. Pipes, ASTM STP 696, pp. 145-171.

4. Grape, J. and Gupta, V., 1995, Failure in Carbon / Polyamide Laminates under Biaxial Compression, *J. Composite Materials*, vol. 29, No. 14, pp1850-1872.

5. Waas, A. and Bacock, C.D., Observation of the Initiation and Progression of Damage in Compressively loaded Composite Plates Containing a Cutout, GALCIT SM Report 86-34(1986). See also GALCIT SM Report 85-12, by the same authors, 1985.

6. Waas, A., 1988, ``Compression Failure of Fibrous Laminated Composites in the Presence of Stress Gradients: Experiment and Analysis", Ph.D. thesis, California Institute of Technology.

7. Waas, A., Babcock, C.D. and Knauss, W.G. *1990*, "An Experimental Study of the Compression Failure of Fibrous Laminated Composites in the Presence of Stress Gradients", *International Journal of Solids and Structures*, Vol. 26, No. 9/10, pp. 1071-1098.

8. Guynn, E. G., and Bradley, W. L., 1989, ``A Detailed Investigation of the Micromechanisms of Compressive Failure in Open Hole Composite Laminates", *Journal of Composite Materials*, vol. 23, May, pp. 479-504.

9. Soutis, C., and Fleck, N.A., 1990, ``Static Compression Failure of Carbon Fiber T800/924C Composite Plate with a Single Hole", *Journal of Composite Materials*, Vol. 24, pp. 536-558.

10. A. Khamseh and A. Waas, Failure Mechanisms in Uniply Composite Plates under Uniaxial Compression, *ASME J. Materials and Technology*, October, 1992.

11. A. Khamseh and A. Waas, Failure Mechanisms of Composite Plates with a Circular Hole under remote Biaxial Planar Compressive Loads, ASME *J. Materials and Technology*, vol. 119, pp56-64, 1997

12. Soutis, C., Fleck, N. and Smith, F., Failure Prediction Technique for Compression Loaded Carbon Fiber-Epoxy Laminate with an Open Hole, *J. Composite Materials*, 25, pp1476- 1498, 1991

13. Soutis, C., Curtis, P. and Fleck, N., Compressive Failure of Notched Carbon Fiber Composites, *Proc. Royal Soc. London A*, 440, pp241-256, 1991.

# CHAPTER 3

# GENERALIZED PLANE STRESS ANALYSIS OF A NOTCHED

# LAMINATED COMPOSITES PLATE

## 3.1. Introduction

One of the main advantages of laminated composite materials is that their overall macroscopic material properties can be manipulated to provide useful characteristics for a specific purpose prior to the manufacturing process. The resulting laminate is usually macroscopically orthotropic. It is well accepted that, in spite of a few shortcomings, such as the ignorance of interlaminar stress components (from assumption of a plane stress state within each lamina), *Classical Laminated Plate Theory* (CLT) plays an essential role in obtaining solutions of macroscopic behavior of the laminate. The macroscopic means that a level of discretization that ignores the detailed structure of a single unidirectional lamina, but still one that incorporates the non-homogeneous nature of the composite in the thickness direction. The main assumptions of CLT are as follows:

1. Each layer of the laminate is homogeneous and orthotropic.

2. The laminate is thin with its lateral dimensions much larger than its thickness and is loaded in its plane only, i.e. the laminate and its layers are

assumed to be in a plane stress state, just as in classical plate theory [Timoshenko, Ref. 3.1].

3. All displacements are small compared with the thickness of the laminate.

4. Displacements are continuous throughout the laminate.

5. In-plane displacements vary linearly through the thickness of the laminate, i.e., $u$ and $v$ displacements in the x- and y- directions are linear functions of $z$, the coordinate normal to the plane of the laminate.

6. Transverse shear strains $\gamma_{xz}$, $\gamma_{yz}$ are negligible. This assumption and the preceding one imply that straight lines normal to the middle surface remain straight and normal to that surface after deformation.

7. Strain-displacement and stress-strain relations are linear.

8. Normal distances from the middle surface remain constant, i.e., the transverse normal strain $\varepsilon_z$ is negligible.

Thus, CLT treats each layer of the composite laminate as being a single layer of homogeneous and anisotropic material whose equivalent properties in terms of the constituents (fibers and matrix) are found by the rule of mixtures, the modified Halpine-Tsai equation [Ref. 3.2] or the generalized self consistent method [Ref. 3.3]. Following CLT, the relations between the inplane stress resultants and inplane strains can be conveniently derived along with the moment-curvature relations. Once these relations are obtained, the entire laminate can be characterized as being a single anisotropic and homogeneous structural element. While a complete account of CLT is beyond the scope of this thesis, it is relevant to point out that an important assumption in CLT is that each *lamina of the laminate* is in a *planar state of stress*.

The chief violators of this assumption, the stress components $\sigma_{zz}$, $\sigma_{yz}$, $\sigma_{xz}$, (z being the coordinate in the thickness direction) are found to persist in a singular fashion at a narrow boundary layer on the order of a *lamina thickness* close to any free edge of the laminate. This result known as the free edge effect has been a topic considered be many researcher. This effect was first exemplified by Pagano and Pipes [Ref. 3.4-3.5] who considered a particular boundary valve problem and used the finite difference method to obtain a numerical solution [Ref. 3.5]. This problem was re-considered by Wang [Ref. 3.6], who used linear elasticity theory to analyze each layer of the lamina and obtained a formal solution. In the period in between, other researchers [Ref. 3.7-3.12] have introduced various levels of sophistication in an attempt to establish the usefulness of knowing the detailed three-dimensional stress field within the boundary layer.

The presence of a singular stress field at a free edge is not surprising as it is well known that a stress singularity exists at the intersection of an interface (ie., the common boundary between two distinct materials along which continuity of tractions and displacements hold) with a free boundary (Bogy [Ref. 3.13]). However, to obtain the complete solution to a boundary valve problem, using anisotropic elasticity theory to analyze each lamina, for a laminate containing several laminae is a lengthy and cumbersome process. Indeed, it is fair to say that such analytical solutions exist only for very special cases of simple loading and geometry.

At present, the use of numerical techniques such as finite elements and finite difference play a major role in characterizing the free edge effect in composites. What must be kept in mind, however, is that in modeling the composite as

consisting of alternating layers of different materials, an artificially abrupt change of properties across an interface is introduced. In a real laminate used in the laboratory, such an abrupt change is not present. Rather, it is likely to find a continuous but rapidly varying function of the material properties through the thickness. However, an exact description of such a variation would have to incorporate information on a microscopic scale, i.e., on the fiber-matrix level within each lamina, and this is not easily amenable to analytical description. Thus, due to a lack of better modeling capability, it is assumed that the layers are perfectly bonded along an interface. This produces a singular state of stress at the free edge/interface deduced from a *linear elasticity analysis*. Away from the free edge, i.e., on the order of a lamina thickness, the CLT results are found to be prevailing.

A practically useful and technically important problem is the behavior of laminates with stress concentrations, because it is at these sites where damage is likely to initiate, resulting in life reduction due to damage growth around these stress concentrations. Stress distributions and stress concentrations around notches can be determined by linear elastic analysis, finite element methods, and experimental methods.

One approach to address the problems of damage initiation and growth is based on concepts of linear elastic fracture mechanics carried over from homogeneous isotropic materials. A second approach is based on actual stress distributions near the notch and makes use of simplified stress fracture criteria. According to the average stress criterion from the latter, failure occurs when the average stress within a characteristic region from the notch equals the strength of

the unnotched material. Experimental verification of this method showed satisfactory agreement in uniaxial tensile loading cases. Other approaches are based on the same logic, proposing a characteristic region where stress concentration is most dominant, then attempts to match local equivalent stress with various macroscopic failure criteria. A recent effort in this direction is described by Soutis [Ref. 3.14].

The problem with the utilization of these approaches in addressing failure due to remote compressive loading is that the above macroscopic averaged stress criteria cannot describe the semi-microscopic characteristics of compressive failure mechanisms such as kink banding, which are highly localized with each constituents (fiber and matrix) interacting with each other. All macroscopic description of these mechanisms ignore the essential details in the damaged material, just as, for example, continuum description of fluid mechanics fails to describe turbulent flow transition mechanism, where the required length scale needed to describe the phenomena is lacking.

Our objective is to propose a different approach in making the connection between the macroscopic composite lamina failure mechanism and the semi-microscopic compressive failure mechanism. But first, it is important to understand characteristics of stress concentration around a notch to establish the basis of our approach. Based on the theory of anisotropic elasticity [Ref. 3.15], the stress distributions around a circular hole in an infinite plate can be obtained.

In this chapter, the 48-ply laminate containing a circular hole is modeled along the lines of CLT as an equivalent and homogeneous anisotropic plate. Then, by dimensional considerations where the width and length of the plates are

47

several times the hole diameter, the two dimensional stress state of an infinite, homogeneous and anisotropic plate containing a circular cutout and subjected to a remotely applied planar state of compressive stress is developed (Figure 3.1). Based on this result, the variation of stress gradient for various hole size will be investigated. The severity of stress gradient, which is characterized by $\left.\dfrac{\partial \sigma_{xx}}{\partial y}\right|_{y=0}$ and the length scale associated with this gradient will be investigated.

An outline of the method used to obtain the stress, strain and displacement distribution will be given along the lines of Lekhnitskii [Ref. 3.15] who treated the similar problem for an elliptical cutout. The solution presented in [Ref. 3.15] will be used and specialized to the case of a circular hole as described in [Ref. 3.16]

## 3.2. Solution Outline

Defining the problem coordinates as in Figure 3.1., the equilibrium equations are, in the absence of body forces,

$$
\begin{aligned}
\frac{\partial \sigma_x}{\partial x} + \frac{\partial \sigma_{xy}}{\partial y} &= 0 \\
\frac{\partial \sigma_{xy}}{\partial x} + \frac{\partial \sigma_y}{\partial y} &= 0.
\end{aligned}
\tag{3.1}
$$

With the assumptions of small deformations, the strain-displacement relations are,

$$\varepsilon_x = \frac{\partial u}{\partial x}, \varepsilon_y = \frac{\partial v}{\partial y}$$
$$\varepsilon_{xy} = \frac{\partial v}{\partial x} + \frac{\partial u}{\partial y}$$

(3.2)

Then the single equation describing the compatibility between the three strain components $\varepsilon_x$, $\varepsilon_y$, $\varepsilon_{xy}$, is given by,

$$\frac{\partial^2 \varepsilon_x}{\partial x^2} + \frac{\partial \varepsilon_y}{\partial y} = \frac{\partial^2 \varepsilon_{xy}}{\partial x \partial y}$$

(3.3)

The coordinate axes are chosen conveniently to coincide with the axes of orthotropy of the laminate. With this choice, the *strain-stress* relation for a generalized plane stress state is

$$\varepsilon_x = \frac{\sigma_x}{E_x} - \frac{v_{yx} \sigma_y}{E_y}$$

$$\varepsilon_y = \frac{\sigma_y}{E_y} - \frac{v_{xy} \sigma_x}{E_x}$$

(3.4)

$$\varepsilon_{xy} = \frac{1}{G_{xy}} \sigma_{xy}$$

with,

$$\frac{v_{xy}}{E_x} = \frac{v_{yx}}{E_y}$$

A stress function F (x, y) defined in the manner described below is chosen such that (3.1) is satisfied identically.

49

# THIS PAGE IS MISSING IN ORIGINAL DOCUMENT

50

$$D_1 D_2 D_3 D_4 F = 0, \qquad\qquad (3.8)$$

where, $\mu_i$ are the roots of the characteristic equation associated with (3.6), namely,

$$\mu^4 + \left( \frac{E_x}{G_{xy}} - 2v_{xy} \right)\mu^2 + \frac{E_x}{E_y} = 0. \qquad\qquad (3.9)$$

The $\mu_i$ are called complex parameters. These can be considered as numbers that characterize the degree of anisotropy in the case of plane problems. Their values give a measure of departure from the isotropic case, for which always $\mu_1 = \mu_2 = i$, and $|\mu_1| = |\mu_2| = 1$, For an orthotropic material, there are three different cases of interest:

I: $\mu_1 = ai$, $\mu_2 = bi$ (purely imaginary and unequal)

II: $\mu_1 = \mu_2 = ai$ (equal and imaginary)

III: $\mu_1 = a + bi$, $\mu_2 = -a + bi$ (complex)

The above designations of cases follows from the fact that the roots of (3.9) can be categorized as $\mu_1, \mu_2, \overline{\mu_1}, \overline{\mu_2}$, where an overbar denotes a complex conjugate. Apart from four exceptional cases as noted in Lekhnitskii [Ref. 3.15], the roots of (3.9) are always complex. For materials considered for this thesis, cases (I) & (III) are of interest. In these cases, the solution to (3.8) can be written as

$$F = \sum_{i=1}^{4} F_i (x + \mu_i y) \qquad\qquad (3.10)$$

Where $F_i(x + \mu_i y)$ are functions of the argument $(x + \mu_i y)$. Let $z_1 = x + \mu_1 y$ and $z_2 = x + \mu_2 y$ denote complex quantities. Then the solution of (3.8) can be expressed as

$$F = \Re\left[F_1(z_1) + F_2(z_2)\right] \qquad (3.11)$$

Where $\Re$ denotes the real part of a complex quantity.

Introduce

$$\phi_1(z_1) = \frac{dF_1}{dz_1}$$
$$\phi_2(z_2) = \frac{dF_2}{dz_2} \qquad (3.12)$$

Then using (3.5) together with (3.4) and (3.2), one obtains

$$\sigma_x = 2\Re\left[\mu_1^2 \phi_1'(z_1) + \mu_2^2 \phi_2'(z_2)\right]$$

$$\sigma_y = 2\Re\left[\phi_1'(z_1) + \phi_2'(z_2)\right]$$

$$\sigma_{xy} = -2\Re\left[\mu_1 \phi_1'(z_1) + \mu_2 \phi_2'(z_2)\right] \qquad (3.13)$$

$$u = 2\Re\left[p_1 \phi_1(z_1) + p_2 \phi_2(z_2)\right] - \varpi y + u_o$$

$$v = 2\Re\left[q_1 \phi_1(z_1) + q_2 \phi_2(z_2)\right] + \varpi x + v_o$$

where $\omega$ characterizes a rigid body rotation, and $u_o$, $v_o$ denote rigid body displacements in the x, y plane. The quantities $p_1$, $p_2$, $q_1$, $q_2$ are given by

$$p_1 = \frac{1}{E_x} \mu_1^2 - \frac{v_{xy}}{E_x}$$

$$p_2 = \frac{1}{E_x} \mu_2^2 - \frac{v_{xy}}{E_x}$$

$$q_1 = -\frac{v_{xy}}{E_x} \mu_1 + \frac{1}{E_y} \frac{1}{\mu_1} \qquad (3.14)$$

$$q_2 = -\frac{v_{xy}}{E_x} \mu_2 + \frac{1}{E_y} \frac{1}{\mu_2}$$

Thus, the stress function $F$ has been expressed in terms of two unknown functions $F_1(x_1)$, $F_2(x_2)$. These functions are to be determined such that they satisfy the appropriate boundary conditions of the particular problem. Once this is achieved, a complete solution to the particular boundary value problem is obtained by using (3.12) and (3.13). Using the method described above, a collection of solved problems can be found in Lekhnitskii [Ref. 3.15], where the

complete generalized plane stress solution of an infinite plate containing an elliptical hole and loaded as shown in Figure 3.1 is also given. This solution is obtained as the superposition of two problems. First, a plate without a cutout under uniform far field compression is considered. This is designated the 'zero' problem. Then a second problem is considered where a plate with the elliptical cutout is considered, loaded on the cutout boundary by tractions which are equal and opposite to those found on a similar but fictitious elliptical boundary of the zero problem. This is designated the 'first' problem. The zero problem is straightforward and the solution is,

$$\sigma_x^o = -P\cos^2\phi$$
$$\sigma_y^o = -P\sin^2\phi$$
$$\sigma_{xy}^o = -P\sin\phi\cos\phi$$

$$(3.15)$$

$$u^o = P\left(\frac{\cos^2\phi}{E_x} - v_{yx}\frac{\sin^2\phi}{E_y}\right)x$$

$$v^o = P\left(\frac{\sin^2\phi}{E_x} - v_{xy}\frac{\cos^2\phi}{E_y}\right)y$$

The 'first' problem is more involved and requires obtaining $F_1(z_1)$ and $F_2(z_2)$ such that the stresses decay to zero at large distances form the cutout. The solution as obtained by Lekhnitskii [Ref. 3.15], is given below.

$$\phi_j(z_j) = (-1)^{(j+1)} \frac{1}{(\mu_1 - \mu_2)} \sum_{m=1}^{\infty} (\bar{b}_m - \mu_j \bar{a}_m) \cdot \xi_i^{-m}$$

$$\xi_j = \frac{z_j + \sqrt{z_j^2 - a^2 - \mu_j^2 b^2}}{(a - i\mu_j b)} \qquad (3.16)$$

$$z_j = x + \mu_j y, \, j = 1, 2$$

with,

$$\bar{b}_1 = \frac{P}{2} \cos\phi (a\sin\phi - ib\cos\phi)$$

$$\bar{a}_1 = -\frac{P}{2} \sin\phi (a\sin\phi - ib\cos\phi) \qquad (3.16b)$$

$$\bar{a}_m = \bar{b}_m = 0, m \geq 2.$$

Substituting (3.16a and b) in (3.13), the stresses and displacements associated with the first problem are obtained. Thus, the complete solution to the original boundary value problem is

$$\sigma_x = \sigma_x^0 + \sigma_x^1$$

$$\sigma_y = \sigma_y^0 + \sigma_y^1$$

$$\sigma_{xy} = \sigma_{xy}^0 + \sigma_{xy}^1 \qquad (3.17)$$

$$u = u^o + u^1$$

$$v = v^o + v^1$$

This solution can now be specialized to the case simulating the present experimental situation by setting

$$\phi = 0 \text{ and } a = b = \text{radius of circular hole}$$

Let 'a' denote the radius of the circular hole. Then,

$$\sigma_x^o = -P,$$
$$\sigma_y^o = 0,$$
$$\sigma_{xy}^o = 0 \qquad\qquad (3.18a)$$
$$u^o = -P\left(\frac{1}{E_x}\right)x,$$
$$v^o = -P\left(\frac{-\nu_{xy}}{E_x}\right)y$$

$$\overline{b}_1 = i\frac{P}{2}a \qquad\qquad (3.18b)$$
$$\overline{a}_1 = 0$$

$$\phi_j(z_j) = (-1)^{(J+1)}\frac{iPa^2}{2(\mu_1-\mu_2)}\left(\frac{(1-i\mu_j)}{z_j+\sqrt{z_j^2-a^2(1-\mu_j^2)}}\right)$$

$$(3.18c)$$

$$\phi_j(z_j) = (-1)^{(J+1)}\frac{iP}{2(\mu_1-\mu_2)(1+i\mu_j)}\left(\frac{z_j}{z_j+\sqrt{z_j^2-a^2(1+\mu_j^2)}}\right)$$

Here $i$ is defined as $i^2 = -1$.

## 3.3. Results

Using (3.13), (3.15), and (3.17), it was possible to calculate any stress component distribution (and corresponding displacement distribution) around the cutout. The result for the displacements and some of the stress components was incorporated in a finite element analysis (Figure 3.5) for use as the loading condition for a micromechanics based response analysis to be explained in chapter 4.

It is our objective in this chapter to understand the characteristics of the dominant stress gradients at the hole edge. The loading case considered is uniform compression at the far field edge in the $x$ direction as shown in Figure 3.1. Only the variation in $\sigma_x$ was considered in this chapter, because this component of compressive stress is the most dominant cause of local failure at the hole edge, which was observed from our experimental work. In the case of equibiaxial loading, the method of superposition is used to obtain the variation of $\sigma_x$.

In Figure 3.2, the origin of the coordinate is at the hole center, and the $\sigma_x(0,y)$ distribution to the point where $\zeta = \dfrac{\sigma_x}{\sigma_o}$ becomes 1.1 (110% of far field loading) is indicated. All length dimensions are non-dimensionalized by the hole diameter. A typical stress distribution around the hole edge is as shown in Figure 3.3. As can be seen in Figure 3.3, the local stress peaks at the hole edge then starts to die out as y increases. The dashed line indicates equibiaxial remote compression loading and the solid line indicates uniaxial compression. It is an interesting fact that the

stress distribution in non-dimensional form is approximately independent of the hole size. This observation implies a characteristic length scale associated with the stress concentration effect, based on geometrical similarity. For the case of cross ply $[0/90]_{12s}$ laminates under uniaxial compression, this characteristic length scale was $l_{cr}^u = {y_{1.1}}/{d_r} = 1.28$. For the case of an equibiaxial loading,

$$l_{cr}^u = {y_{1.1}}/{d_r} = 1.33.$$

Previous research reported in Whitney & Nuismer [Ref. 3.17] and Nuismer & Whitney [Ref. 3.18], attempt to characterize the hole size effect through the point stress criterion (PSC) and the average stress criterion (ASC). According to the PSC, failure occurs when the dominant tensile strain $\sigma_x(0, y)$ at some distance $y = d_o$ away from the hole reaches the unnotched tensile strength of the material (note that PSC and ASC were introduced in the context of tensile loading, but in principle would be applicable for compression loading as well). On the other hand, the ASC is based on the assumption that failure occurs when the average value of $\sigma_x(0, y)$ over some fixed distance $a_o$, from the hole edge reaches the unnotched tensile strength $\sigma_o$ of the material, i.e.

$$\frac{1}{a_o} \int_R^{R+a_o} \sigma_x(0, y)\, dy = \sigma_o \qquad (3.19)$$

Notice that these criteria are transparent to the details of the failure mechanism observed via our experimental results as described in chapter 2. They are based on averaged macroscopic values of stress that do not reflect deformation mechanisms at the fiber/matrix level. Furthermore, these criteria

can produce the same results for differently stacked laminates (i.e. laminates with different lay-ups, but with the same macroscopic averaged mechanical properties).

While the stress concentration factor is independent of the size of the hole, the stress gradient factor (G.F.) as defined in (3.20) is dependent on the hole size. The G.F. is defined as

$$\left(G.F.\right)^{-1} = \left.\frac{\partial \zeta}{\partial \tilde{y}}\right|_{\tilde{y}=1} \qquad (3.20)$$

where, $\zeta = \dfrac{\sigma_x}{\sigma_o}$ and $\tilde{y} = \dfrac{y}{d_r}$.

G.F. indicates the severity of the gradient as one moves away from the hole edge along the $y$ axis. A larger G.F. indicates a smaller hole while a smaller G.F. indicates a larger hole for a given material. Furthermore, for laminated composite materials, G.F. is, in general also a function of mechanical properties, but for isotropic material, G.F. is only influenced by the hole size. In Figure 3.4, we have shown a plot of G.F. as a function of hole size. In Figure 4.10, we have indicated the experimental result of Khamseh & Waas [Ref. 4.2] for uniply composite laminates under uniaxial compression, scaled appropriately. Notice that the trend of failure strength is similar. In other words, G.F. is a reasonable indicator of the trend in failure as a function of hole size. However, G.F. alone is insufficient to provide an absolute means of compressive strength, unless at least one point on the curve can be calibrated against some known experimental data or an analytical mechanism based prediction.

The approach advocated in this thesis is a hybrid-local-global model, where 'global' indicates resultant stress, strain and displacement distribution calculated using CLT and 'local' indicates a detailed analysis carried out at the fiber/matrix level. The local analysis is the subject of the next chapter.

## 3.4. Figures
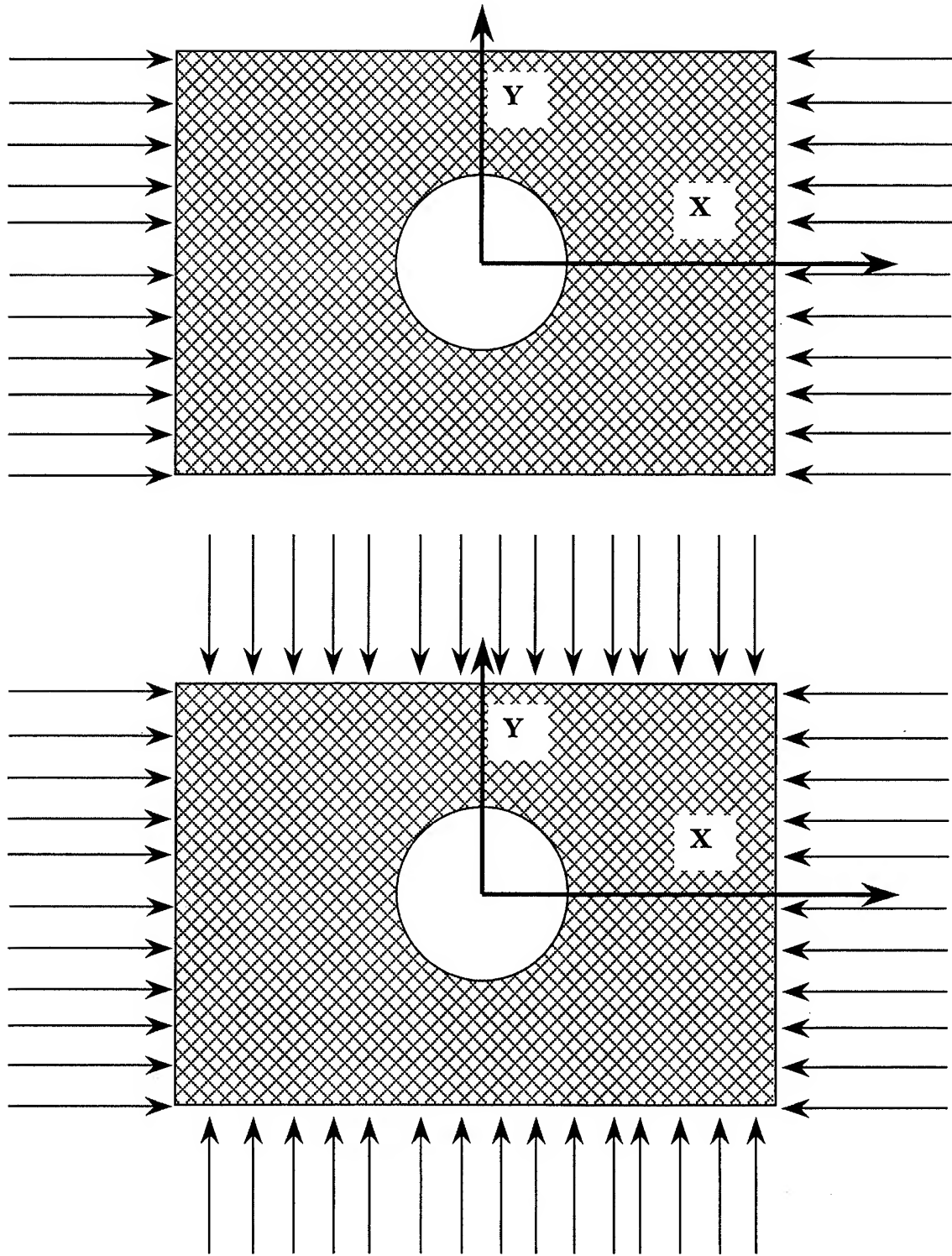


**Figure 3.1 Uniaxial and Biaxial loading case**
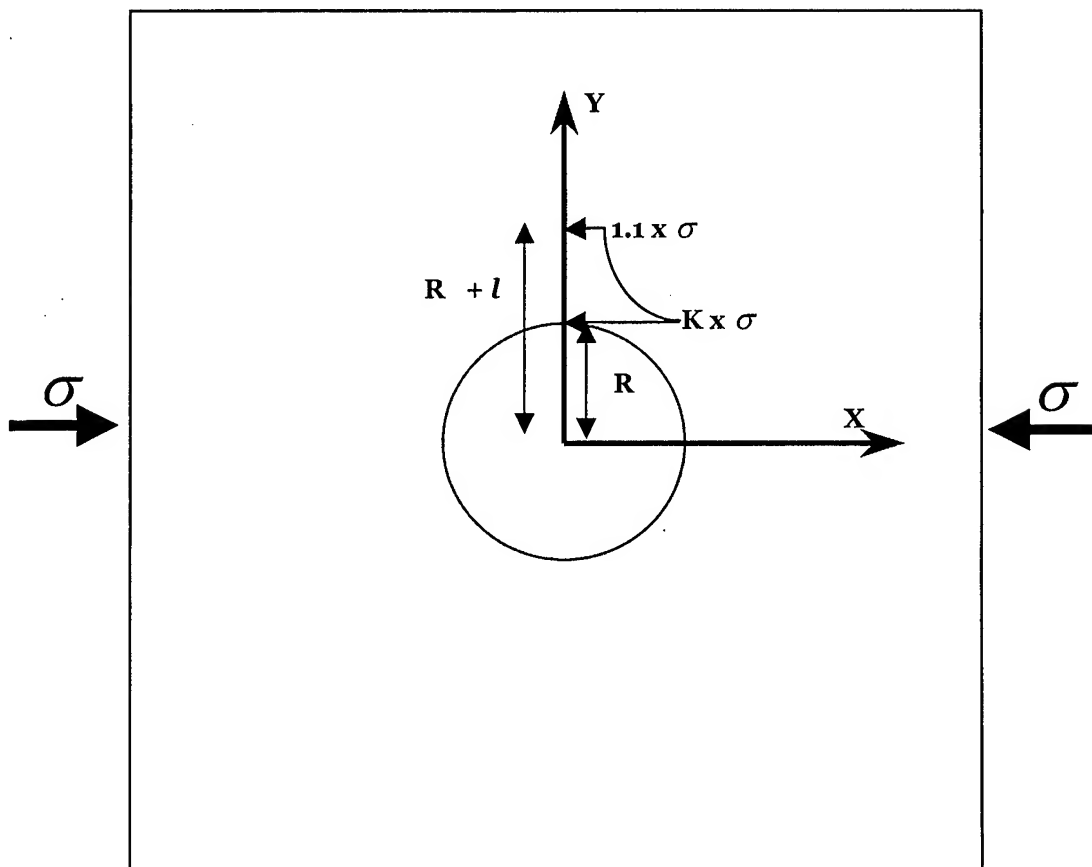
**Figure 3.2 Stress Gradient Definition**

# Nondimensionalized Stress Distribution
## Crossply
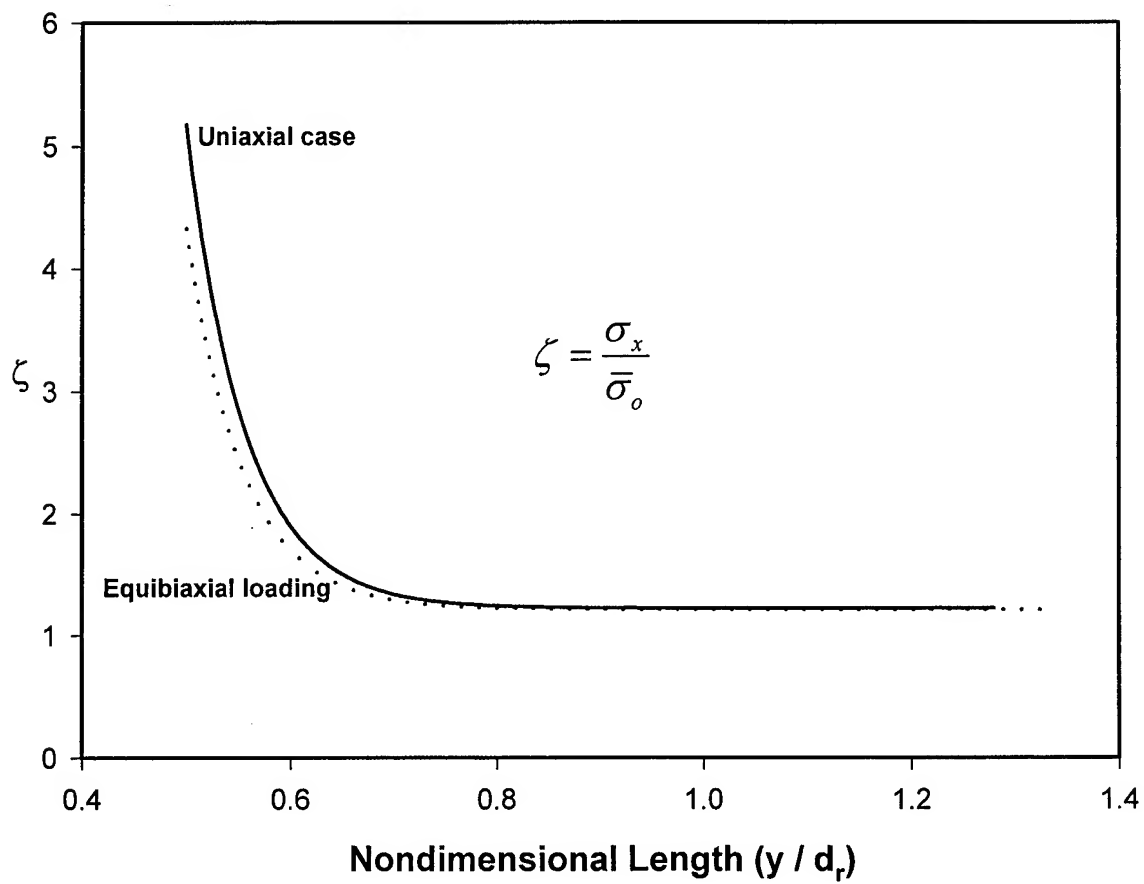


Figure 3.3 Nondimensional Stress Gradient for Cross-ply Laminates ($d_r$ = 2 R)

# Gradient Factor vs Hole Size $(0/90)_{12s}$
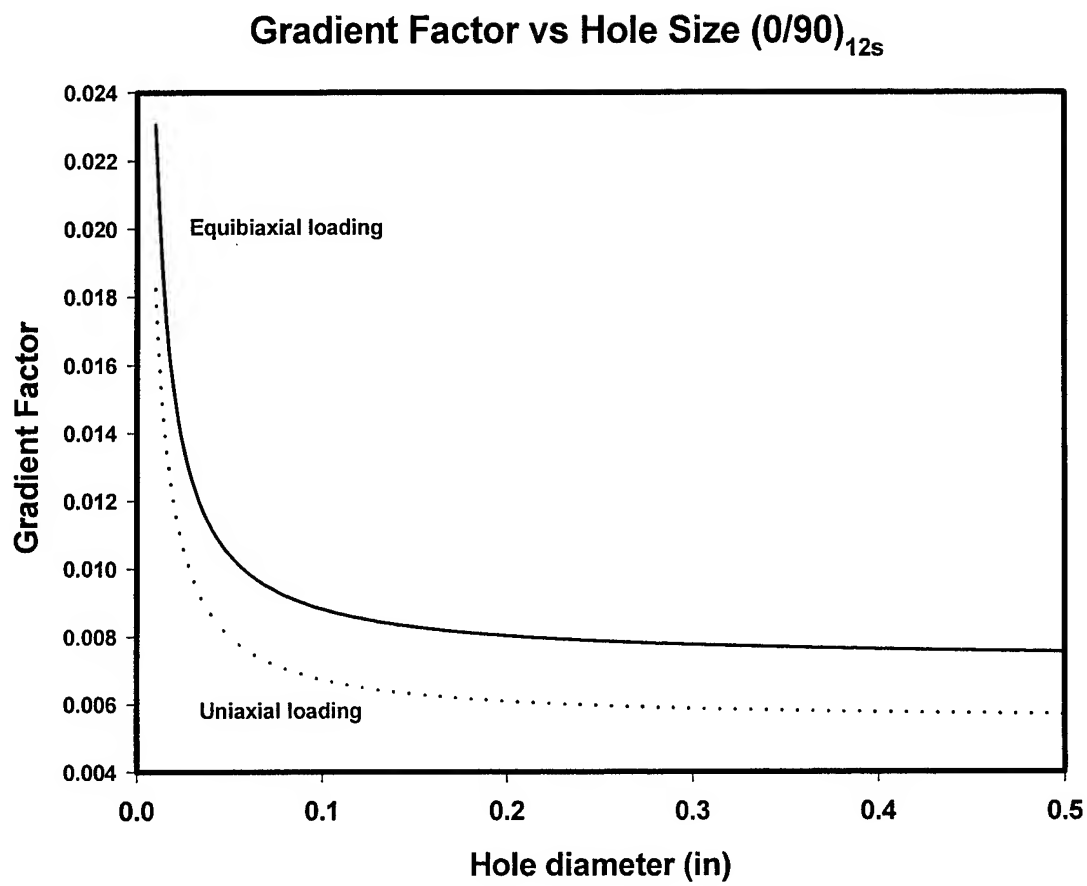


Figure 3.4 G.F. Distribution
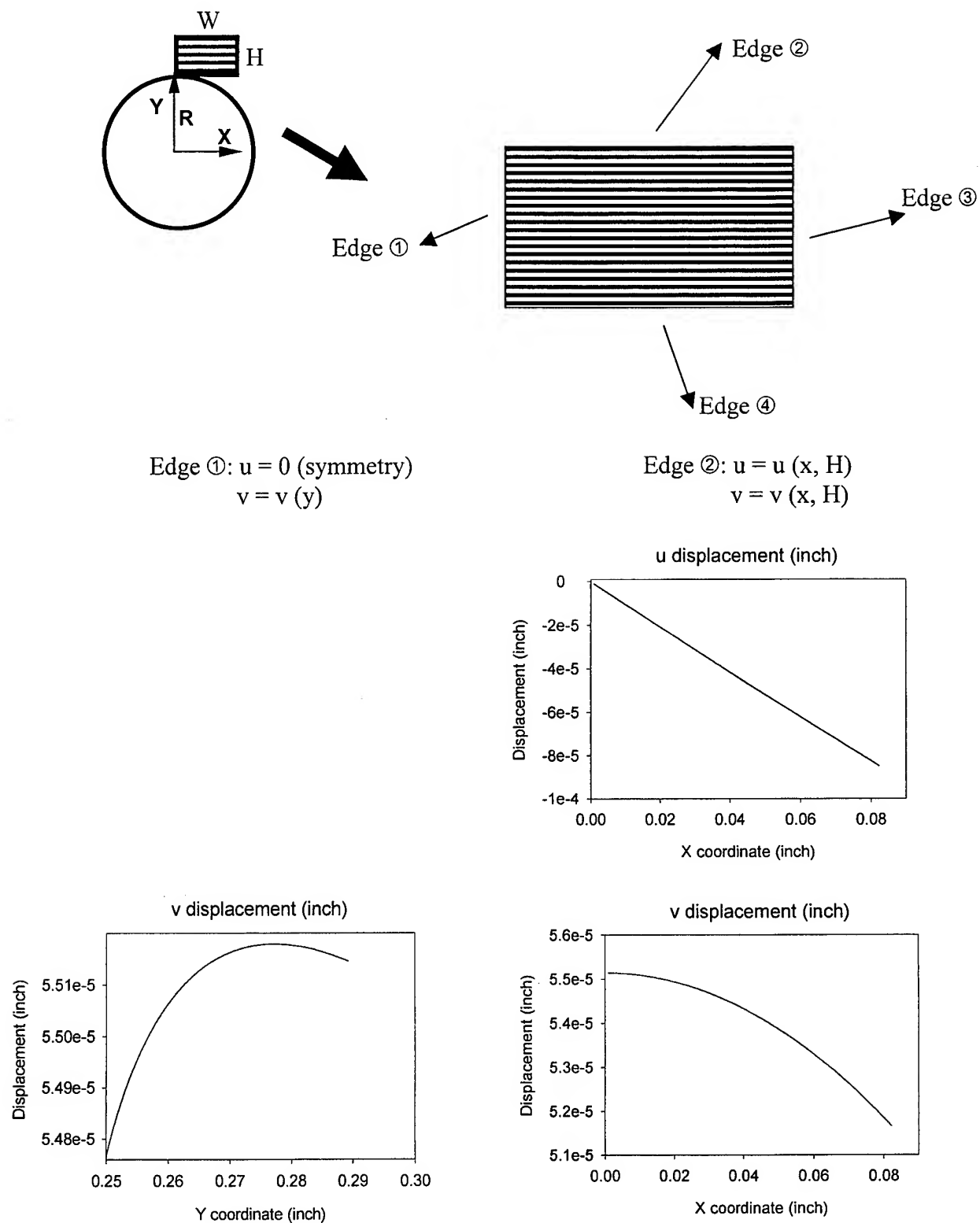
Edge ①: u = 0 (symmetry)        Edge ②: u = u (x, H)

       v = v (y)                          v = v (x, H)

**Figure 3.5 Typical Result incorporated to FEA Model (cross ply, uniaxial compressive loading 10 Ksi)**

65

Edge ③: u = u (W, y)
v = v (W, y)

Edge ④: u = u (x, R)
v = v (x, R)
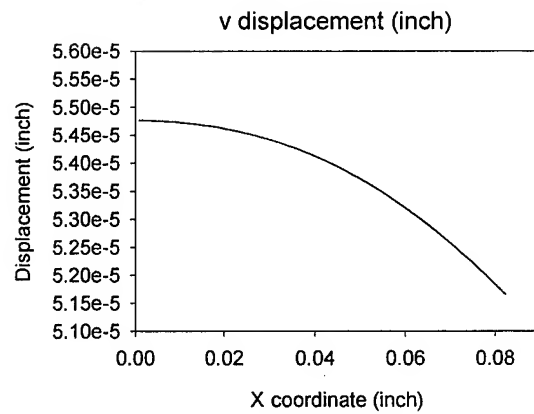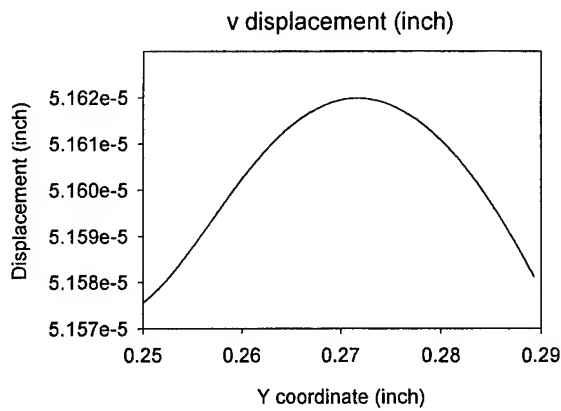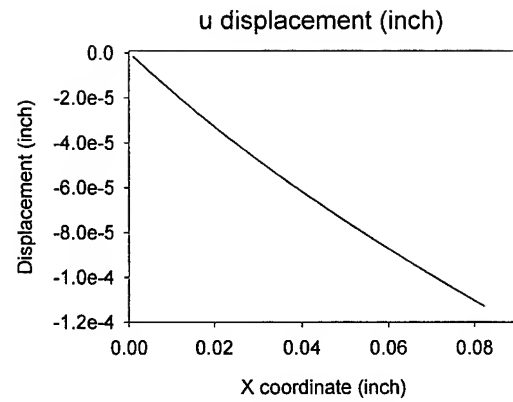
u displacement (inch)

u displacement (inch)

v displacement (inch)

v displacement (inch)

**Figure 3.5 Typical Result incorporated to FEA Model (cross ply, uniaxial compressive loading 10 Ksi), Continued**

66

## 3.5. References

1. Timosheko, Stephen, 1959, "Theory of Plate and Shells", McGraw Hill

2. J.C. Halphin and S.W. Tsai, 1969 "Effects of Environmental Factors on Composite Materials," AFML-TR 67-425

3. C.C. Chamis and G.P. Sendecky, 1968, "Critique on Theories on Predicting Thermoelastic Properties of Fibrous Composites," *J. Compos. Mater.*, 2 (3), 332

4. Pagano, N.J. and Pipes, R.B., 1973, "Some Observations on the Interlaminar Strength of Composite Laminates", *Int. J. Mech. Sci.*, Vol. 15, 679-698

5. Pagano, N.J. and Pipes, R.B., 1974,"Interlaminar Stresses in Composite Laminates- An approximate Elasticity solution", J. App.Mech., Vol. 41, 668-672

6. Wang, S. S. and Yuan F.G., 1983, "A Singular Hybrid FEM Analysis of Boundary Layer Stresses in Composite Laminates", *Int. J. Solids & Struct.* , Vol. 19, 825-837

7. Tang, S., 1975," A Boundary layer Theory-Part 1: Laminated Composites in plane Stress", *J. Comp. Matls.* , Vol. 9, 33-41

8. Tang, S. and Levy, A., 1975, "A Boundary layer Theory-Part 2: Extension of laminated Finite Strip", *J. Comp. Matls,* Vol. 9, 42-52

9. Rybicki, E.F., 1976, "Three Dimensional Stress Analysis of a Laminated Plate Containing an Elliptical Cavity", AFML-TR-76-32

10. Raju, LS and Crews, J.H., Jr., 1982, "Three Dimensional Stress Analysis of a (0/90)s and (90/0)s Laminates with a Central Circular Hole", *Comp. Tech. Review*", Vol. 4. 116-125

11. Ericsson K., Persson L., Carlsson L. and Gustavsson A., 1984, "On the Prediction of the Initiation of Delamination in a (0/90)s Laminate with a Circular Hole", *Int. J. Eng. Sci.* , Vol. 22, 57-75

12. Delale F., 1984, "Stress Analysis of Multi-layered Plates around circular Cutouts", *Int. J. Eng. Sci.*, Vol. 22, 57-75

13. Bogy, D.B., 1969, "Edge Bonded Dissimilar Orthogonal Elastic Wedges Under Normal and Shear Loading", *J. App. Mech.*, Vol. 40, 460-466

14. Soutis, C., Curtis, P.T. and Fleck, N.A., Compressive Failure of Notched Carbon Fiber Composites, Proc. Royal Soc. London A, 1991, 440, 241-256

15. Lekhnitskii, S. G., 1963, "Theory of Elasticity of an Anisotropic Elastic Body"

16. Waas, A., Compression Failure of Fibrous laminated Composites in the Presence of Stress Gradient: Experiment and Analysis, Ph.D. thesis, California Institute of Science and Technology.

17. Whitney, J. M. and Nuismer, R. J., 1974, "Stress Fracture Criteria for Laminated Composites Containing Stress Concentrations,", *Journal of Composite Materials*, Vol. 8, 253-265

18. Nuismer, R. J. and Whitney, J. M., 1975, "Uniaxial Failure of Composite Laminates Containing Stress Concentrations," in *Fracture Mechanics of Composites*, ASTM STP Vol. 593, 117-142, American Society for Testing and Materials, Philadelphia

# CHAPTER 4

# MICROMECHANICS-BASED FINITE ELEMENT MODEL FOR COMPRESSIVE FAILURE OF NOTCHED LAMINATES UNDER REMOTE COMPRESSIVE LOAD

## 4.1. Introduction

This chapter is based on the publication by Ahn and Waas [Ref. 4.1], which was concerned with a micromechanics based finite element analysis for the failure of notched single ply (uniply) model laminates. Experimental results obtained by Khamseh and Waas [Ref. 4.2] formed the basis of this model. This chapter sets the stage for the chapter 7. In chapter 7, the model presented here is extended to analyze multidirectional laminates, with a view to explaining the experimental data presented in chapter 2. The reader can skip this chapter and chapter 5 (a micromechanics analysis of $(\pm\theta)_{ns}$ angle ply laminates) and go onto chapter 6 uninterrupted.

Of concern in the present chapter is the development of a micromechanics based model to predict the onset of failure in laminated composite plates containing a stress raiser in the form of a circular hole. The development of the model relies on previous experimental work described in Khamseh and Waas [Ref. 4.2], which provides experimental data for the compressive strength of

uniply notched composites as a function of notch size. Because of the importance of the experimental work that led to the development of the model presented here, a brief description of the experimental findings reported in Khamseh and Waas [Ref. 4.2] will be explained next.

## 4.2. Experimental Summary

Khamseh and Waas [Ref. 4.2] experimentally studied the effect of notch size on the compressive strength of laminated plates. Specially prepared uniply laminates were studied. A single lamina of graphite/polymer was embedded between two transparent ULTEM polymer sheets and cured according to the manufacturer's recommendations. The measured properties of the uniply laminate (UL) are given in Table 4.1. The transparent nature of the UL provides a convenient means of measuring details pertaining to the dominant failure mechanism of kink banding. Kink band width, length and extent were measured without having to deply the laminate. Specimens measuring $L = 1.68$, $S = 1.68$, and $t = 0.275$ (all in inches, Figure 4.1), were prepared with a single centrally located circular cutout of varying diameter inserted with a diamond drill. Remote uniaxial loading along the zero fiber direction ($x$-axis) and remote biaxial loading (along the $x$-axis and $y$-axis) were studied. Failure initiation was detected via holographic interferometry for uniaxial loading that measured out of plane deformation. The corresponding strains were obtained via surface strain gages and the far-field load on the specimen corresponding to failure initiation was

measured via a load cell. For biaxial loading, initiation strains were obtained via strain gages placed near the cutout edge.

The failure mechanism for the laminates was determined to be kink banding at the hole edge followed by delamination near the failure site, resulting in the propagation of the damage into the interior of the specimen (uniaxial). For biaxial loading, post-experiment microscopic examination revealed, both, fiber/matrix debonding and a shifted kink band. Thus, from the photomicrograph alone it cannot be conclusively stated whether kink banding proceeds or precedes fiber/matrix debonding. The transparent nature of the thermoplastic sheet revealed (in several specimens that were loaded to failure by kink banding and immediately unloaded) that no delamination was associated with the failure initiation. This finding establishes that kink banding (uniaxial) and fiber/matrix debonding with a shifted kink band (biaxial) precedes delamination failure; such a conclusion could not be definite, merely hypothetical, with opaque graphite-epoxy laminates. For hole sizes smaller than 0.1040 in. the failure site shifts away from the hole edge and begins at the free lateral edge. In these situations, failure occurs globally (delamination of the thermoplastic/ply interface throughout the specimen) without any kink banding.

Optical scanning of damaged sections for those specimens that failed by kink banding revealed three-dimensional kinking patterns. That is, during kink banding the 0° fibers undergo large rotations both inplane ($xy$) and out of plane ($xz$). Of the several samples with the same hole size that had failure initiated at the hole edge, at least one sample was examined under an optical microscope. The results of the sectioning study are shown in Figure 4.2(a) and Figure 4.2(b)

as photomicrographs where kink banding near the hole edge is shown for the uniaxial and biaxial cases, respectively. Table 4.2 and Table 4.3 provide a comparison between experiment and analysis for remote uniaxial and remote biaxial loads.

The experimental results summarized above indicate that when laminates containing 0° plies are loaded in compression, the fibers kink with a long wavelength inplane mode and a short wavelength out of plane (through the thickness) mode. The critical strain values for all specimens were measured via surface strain gages placed at the hole edge. The far field failure stress values were computed as the failure load (the load at which strain gage readings indicate a drop in value) on the specimen (monitored through the load cell) divided by the specimen cross sectional area in contact with the loading apparatus. The results obtained by Khamseh and Waas [Ref. 4.2] substantiate and confirm earlier results obtained by Waas and Babcock [Ref. 4.3], Waas et al. [Ref. 4.4]. In these investigations, opaque carbon fiber reinforced notched laminated plates were used.

The main objective of the present chapter is to show that it is possible to use micromechanics as a basis to obtain the remote loads corresponding to failure initiation near the notch. Such an approach offers the possibility of designing the microstructure of the material to delay the onset of failure initiation. A parametric study to understand the effect of different fiber volume fractions and the effect of different fiber and mechanical properties on the observed and predicted kink banding is relegated to a later investigation. The micromechanics based modeling is described next.

72

## 4.3. Micromechanical modeling

The finite element method (FEM) is used for the solution of the micromechanics model. A mesh of a region adjacent to the hole edge was generated using the Hypermesh® Pre/Post processing software as shown in Figure 4.3. In choosing this micro-region, features of the two dimensional linear elastic stress and strain field for a laminated plate containing a circular cutout and loaded remotely (Lekhnitskii [Ref. 3.15]), were used to aid in selecting the mesh size. Symmetry with respect to loading and geometry were also used in arriving at the initial mesh size. The two dimensional elastic stress and strain fields show a marked gradient that depends only on the size of the cutout. These gradient fields persist for distances that are about one hole radius away from the cutout edge. Experimental observations have revealed that the region of kink banding is confined to distances within the gradient field. Furthermore, surface strain gages placed remotely from the hole (i.e. at distances that are several radii away) indicated no change in value corresponding to the inception of kink banding. Thus in the present setting, for analytic purpose, it is possible to assume that kinking is a localized event, not affecting the strain state of the laminate in the far-field (regions that are removed from the location of the cutout). Obviously, the finite element results must eventually verify that such an assumption is reflected in the solution it produces. I will return to this point later in this chapter. The FEM mesh corresponds to the middle ply of the plate specimen only, i.e., the graphite/epoxy ply sandwiched between two thick ULTEM outer layers, as the focus of the FEM was to model the dominant inplane

kink banding failure associated with the fibrous layer. Previous work (Waas et al., [Ref. 4.4] and Soutis and Fleck [Ref. 4.5]) has shown that kink band width and geometry are influenced by a number of factors, such as the location of the zero plies within a laminate, the total thickness of a zero ply, the mechanical properties of the fibers and resin, and the stress state within the zero ply. In the present numerical study, a major focus is on capturing the effect of the stress and strain gradient in influencing compressive failure via kink banding, by adapting a 2D planar model to capture the in-plane deformation associated with kink banding.

For the FEM analysis, a rectangular mesh containing 22,650 elements (4 noded quadrilateral plane stress) and 23,028 nodes with two degrees of freedom (x, y displacements) per node was chosen. Both, a first and second order plane stress element were used and after obtaining results for several runs, it was deemed that either of the two elements provided similar information; of course, approximately twice as many elements were needed with the first order element to achieve the same result, however, the use of a first order element was unavoidable due to limitation in modeling and applying non-homogeneous traction boundary conditions. To avoid shear locking, it was necessary to use 2 rows of elements for each fiber and matrix.

The initial mesh size (termed 'baseline model') corresponds to a rectangular region which is 300 fiber diameters ($d_f$) in length and 142 fiber diameter in width. The elements were of length 2 $d_f$, and width 0.5 $d_f$, such that two layers of elements constitute a single fiber. The matrix was also modeled with two adjacent elements, albeit the two matrix element differed in width from the two fiber

elements, taking into account the difference in thickness of the matrix such that the fiber volume fraction ($V_f$), corresponded to the specimen (57%). Starting with this initial mesh, convergence of the results was checked by incrementally increasing the mesh size until no substantial change in the salient features associated with kink banding was discerned (Figure 4.4 - 4.5). This process was carried out for several hole sizes, corresponding to those studied experimentally as well as for larger hole sizes corresponding to current experimental work. The results of a mesh sensitivity study is shown in Figure 4.6, for a configuration with $d/L = 0.3$. In this figure, the terminology indicated in the legend corresponds to those shown in Table 4.4, where important indicators of the salient features associated with such a study are tabulated. Since the initial mesh size corresponding to each hole size was chosen to be sufficiently large so that the stress gradients have diminished at the remote boundaries of the microregion, it was not surprising to find that the results obtained with this initial mesh were already within a few percent of the values obtained with increasing mesh size. In addition, since the cutout size is the only characteristic length of concern, the mesh size used to obtain converged results for various cutout sizes scaled with the size of the cutout. That is, a small cutout size has steeper gradients than a larger cutout size and thus, a smaller microregion can be used for the FEM analysis (and was used) corresponding to a small cutout size.

In the context of Figure 4.3, and Figure 4.7, where H is the height of the microregion, it was found that $H/d$ = constant, was satisfied to obtain converged results, where d is the diameter of the cutout.

For the elastic pre-kinking analysis, material properties obtained from the experiment were used as an input to determine the stresses and the displacements via a closed form solution as described in Lekhnitskii [Ref. 3.15], for an equivalent homogeneous and orthotropic plate of infinite extent remotely loaded by uniform tractions. On the boundaries of the mesh (Figure 4.8), the displacement fields obtained from the prekinking analysis were enforced as boundary values. For each cutout size, two response analyses were conducted; kink banding that is symmetric about the y-axis, i.e. kinking displacements that satisfy $u(x) = u(-x)$ and $v(x) = v(-x)$, and anti-symmetric kink banding, i.e. $u(x) = u(-x)$ and $v(x) = - v(-x)$, where $u$ and $v$ are the displacements in the $x$ and $y$ directions, respectively. For the symmetric case, the following boundary values were enforced (Figure 4.3): edge AB; $u = 0$, $v = v_p$, along edges BC, CD, and DA; $u = u_p$, $v = v_p$ (where the subscript $p$ refers to the values from the displacements obtained from the prekinking analysis). For the anti-symmetric case, the boundary conditions were the same along edges BC, CD, and DA, but along edge AB; $u = 0$, $v = 0$. Analyses corresponding to both cases were carried out and it was found that the case corresponding to anti-symmetric boundary conditions resulted in a slightly smaller maximum load and plateau load values. Consequently, results presented in the chapter for the response analysis correspond to anti-symmetric boundary conditions.

The linear elastic stress field that persists in the early stages of loading, corresponding to the above geometry is non-uniform because of the cutout. This non-uniformity is a function of the cutout size. For small cutouts, the stress and

strain gradient associated with the elastic prekinked solution characterize the dominant features of the kink banding that is seen in the experiment.

The displacements on the remote boundaries of the microregion were applied in an incremental fashion using the Riks algorithm as available in ABAQUS® [Riks, Ref. 4.6] and incorporating geometrical and material nonlinearity. The basis of this method is to use the load magnitude as an additional unknown and thus to control the increments taken along the load-displacement response curve. This approach provides solutions regardless of whether the response shows stable or unstable behavior.

The matrix was modeled as an elastic-plastic isotropic solid obeying $J2$ incremental theory of plasticity with isotropic hardening. The stress-strain curve for the matrix was generated by employing a standard uniaxial compression test of the pure matrix and is shown in Figure 4.9. However, the properties of the pure resin are not the same as those in the composite laminate as has been noted before by a number of investigators [Kyriakides et al., Ref. 4.8], [Soutis and Fleck, Ref. 4.5].

One way to reflect the in-situ state of the matrix is to use the results of a shear test on the unidirectional composite material and back out the resin properties as has been done in Kyriakides et al. [Ref. 4.8]. However, a more fundamental issue is to recognize the role of residual stresses in the resin caused during manufacturing. Since the Poisson's ratio of the fibers is much smaller than the resin Poisson's ratio, this mismatch results in a state of residual stress in the fibers and resin at room temperature. These stresses can contribute to the difference in properties seen in pure resin tests as contrasted against those that

are inferred from tests on a unidirectional composite sample. A shear test to obtain the in-situ resin material properties is described in chapter 6 in connection with the multidirectional laminates examined experimentally in this thesis.

In carrying out the response analysis, the entire boundary loads (and displacements) on the microregion were increased incrementally via the Riks method. Thus, this corresponds to proportional loading. The assumption here is that the boundary loading on the microregion is unaffected at the initiation and early stage of kink formation via fiber rotation, since the microregion is chosen to be large enough compared with the length scale associated with the stress and strain gradients. That is, kinking is a localized event and does not affect areas remote from the cutout as seen in the experiments of Khamseh and Waas [Ref. 4.2].

During the loading, the resultant horizontal force (in the x-direction) as a function of remote boundary displacement on edge AB was recorded. A typical plot of this is as indicated in Figure. 4.7 for uniaxial loading, where the resultant load is normalized with respect to the height, H of the microsection. Similar plots were generated for biaxial loading conditions as well and are not presented here for the sake of brevity.

## 4.4. Results and Discussion

As can be seen from the plots of Figure 4.7, the calculated resultant force per unit length in the $x$-direction (RF1 / H) versus load proportionality factor, LPF (i.e., the factor by which the boundary displacements applied in the first step of the incremental Riks analysis is multiplied) curves all display similar features. Initially, the curve is linear, followed by an unstable unloading path from a maximum load, that eventually asymptotes to a constant value.

The maximum load is referred to as a limit load while the constant value is referred to as a plateau load. If small initial geometrical imperfections associated with fiber waviness are included, then a family of curves can be generated as a function of initial imperfection magnitude. Such a family of curves is shown in Figure 4.7 where curves generated with three imperfection magnitudes are shown along with the response obtained in the perfect case for uniaxial loading. The imperfection shapes were generated by carrying out a linear eigenvalue analysis of the microregion and obtaining the eigenmode shapes. Next, the maximum amplitude of fiber waviness associated with the mode shapes was set at a fraction of the fiber diameter, $d_f$, to correspond to different imperfection magnitudes. These are indicated in Figure 4.7. As the imperfection size increases, the limit load decreases and eventually disappears. Then the RF1-LPF curve shows a smooth increase from zero to the same plateau load value that is obtained with the perfect case. This finding is an important result, namely that the plateau load is independent of the imperfection size and can be obtained by analyzing the case corresponding to the geometrically perfect mesh. This is observed to be true in

79

the uniaxial cases as well as the remote biaxial cases. Examination of the deformed shapes of the microregion and stress and strain values of the matrix material corresponding to the maximum load indicate that the matrix is fully plastic near the hole (near point A of the microregion) as well as along the edges and within the kink band that is to follow subsequently, while the matrix elements far away (near the points B, C, and D of the microregion) are still elastic (strains of approximately 0.027, see Figure 4.9). Thus, the use of the Lekhnitskii [Ref. 3.15] elasticity solution to characterize the far-field stresses and strains are justified. Furthermore, important quantities from the FEM results, such as the maximum load and plateau load are only mildly sensitive to the size of mesh employed as shown in Table 4.4, and also in Figure 4.6, where the effect of employing different size microregions has been established. This mesh independence is not surprising and is to be expected on physical grounds, since the problem under consideration is one, where the stress and strain gradients die out with distance away from the cutout. The gradients are determined by the cutout size only and thus, the problem has the requisite length scale dictated by the geometry of the configuration analyzed.

Notice that the non-uniformity in the prekinking stress field coupled with a progressively decreasing instantaneous shear modulus of the matrix material provides the necessary synergy to initiate the evolution of kink banding. Beyond the limit load, both RF1 and LPF decrease (the Riks algorithm can capture unstable post buckling behavior) and this decrease as can be seen for the deformed configurations of the mesh is due to deformation localization, close to the edge of the hole. The remote (far-field) loads on the specimen corresponding

80

to the limit load and the plateau load are tabulated in Table 4.2, as a function of hole size for uniaxial loading, while Table 4.3 provides a similar comparison for biaxial loading, and it appears that predictive far-field loads for kink banding (without regard to modeling fiber/matrix debonding) are in reasonable agreement with experiment, suggesting that the energy release associated with fiber/matrix debonding is small compared to the plastic energy associated with kink banding. Experimentally, whether fiber/matrix debonding precedes kink banding cannot be conclusively stated via post-experiment microscopic examination of failed specimens that showed a fiber/matrix debond and a kink band on the same photomicrograph. This suggests that kink banding occurring at a location slightly skewed with respect to the x-y axis at the hole edge (i.e., not at approximately 90 deg. as would be the case with uniaxial loading), could drive fiber/matrix debonding failure and not vice-versa. This aspect necessitates further experimental investigation.

In Table 4.2 and Table 4.3, the measured experimental results for the far-field stress corresponding to failure initiation is also indicated. The agreement between experimentally measured far field failure initiation values and predicted values based on the plateau load are seen to follow the same trend over a significant range of hole sizes, although the FEA predictions are seen to be higher throughout. A plot of the far-field stresses corresponding to failure initiation is shown in Figure 4.10 and Figure 4.11, which also provides a comparison with experimental data. In the biaxial case, the larger of the two applied far-field stresses are used to present the data in Figure 4.10.

81

It is unclear why the biaxial data based on the plateau load seem to agree a lot better than the corresponding uniaxial data in the comparison presented in Figure 4.10 and Figure 4.11. This better agreement may be due to the fact that the biaxial specimens revealed experimentally both fiber/matrix debonding and kink banding, thus the experimental data account for both these mechanisms, while numerically, perhaps a higher maximum load and a lower plateau load would be predicted if one was to accommodate the possibility of capturing both of these mechanisms using one model. It must be noted that throughout this chapter, the numerical results presented correspond to converged results as far as mesh size is concerned. A discussion of this aspect was given earlier. It is not at all surprising to obtain fast numerical convergence in the present problem because the event under investigation is truly local and scales with the size of the cutout, which is the only structural length scale of importance.

The micromechanics model that is introduced here considers a two-dimensional analysis of an essentially three-dimensional phenomenon. Furthermore, it uses the uniaxial stress-strain response of the pure matrix. As will be shown in chapter 6, the pure matrix response tends to overestimate the mechanical properties of the in-situ matrix. As a result, predicted values for the limit load are much higher than the corresponding experimentally measured failure initiation loads. Despite these shortcomings, it appears that misalignment and/or nonuniformities in the prekinking stress field coupled with a nonlinear shear response of the matrix whose modulus is continually decreasing leads to the type of deformation localization that is observed in experiment. The presence of the cutout introduces a natural length scale that is reflected in the gradients

associated in the prekinking stress field. Therefore, even without an initial geometrical imperfection, it becomes possible to simulate kink banding. The present problem can be contrasted against the uniform prekinking deformation situations that have been analyzed earlier Budiansky and Fleck [Ref. 4.7] and Kyriakides et al. [Ref. 4.8]. In the present study and in those earlier studies, however, an essentially three-dimensional situation has been modeled using a two dimensional approach. Thus it appears that other possible modeling omissions, such as the presence of fiber ends within the matrix and the three-dimensional random packing of the fibers (Kyriakides and Ruff [Ref. 4.15]), may have only a weak influence on the overall outcome of the initiation of kink banding.

A complete characterization of the 3D-stress field in a laminated composite plate containing a cutout has been recently done by Iarve [Ref. 4.9]. Incorporation of that work in the context of the present analysis is left as a future task. In Iarve's work, the pre-kinking stress field accounts for the 3D stress state near the cutout, whereas in the present analysis, this stress state is assumed two dimensional. Soutis et al. [Ref. 4.10-4.11] collectively referred to as SFS have previously introduced predictive models for failure initiation in unidirectionally compressed notched composites. To use the SFS, one needs as input the unnotched strength of the laminate and the fracture toughness associated with kinking (obtained via separate additional material characterization tests). Recent work by Soutis [Ref. 4.12] has shown that the input parameters for the SFS could be deduced from the in-plane fracture toughness and the unidirectional unnotched compressive strength, although this requires two additional pieces of

data. Unlike SFS, the present micromechanics based model directly captures the salient features of the deformation localization; the only parameters that are needed as input are the material properties of the constituents (elastic and plastic properties of the matrix which are obtained via a single uniaxial test, and the fiber Young's modulus), the geometry and the stacking. The effect of stacking (i.e. plies other than zero plies) is accounted for via the calculation of the prekinking elastic displacement field which is influenced by the number, type, constitutive property and thickness of the layers in the laminate. These influences enter through the computation of the in-plane stiffness, which are needed to implement the Lekhnitskii [Ref. 3.15] solution for the prekinking stress and strain fields.

In the SFS, the unnotched compressive strength of the laminate is needed as input, and it is not entirely clear that a macroscopic value of unnotched laminate strength may capture the same features of the failure mechanisms near a cutout edge. For example, it is quite possible for an unnotched laminate to fail by a mechanism other than kink banding, while the corresponding notched laminate may in fact still fail by kink banding owing to the presence of the notch that introduces a well defined location (due to the stress and strain concentration) for the failure to initiate. This does not imply that stress gradients are necessary for kink banding, however, the mechanics of kink banding appears to scale with features associated with the stress and strain gradients as has been presented here via a numerical analysis, and before [Khamseh and Waas, Ref. 4.2] via an experimental study. Further experimental work is required to shed more light on the issue of modeling the mechanics of a kinked zone as a crack with a linear

traction-crack closure law. The latter forms a strong basis for the SFS model. Using the SFS model, impressive agreement between experiment and analysis is reported in Soutis, Fleck, and Smith [Ref. 4.11]. In passing, it is relevant to note the recent work of Soutis and Tenchev [Ref. 4.13] who have introduced a property degradation model for microbuckling failure in laminates, and Soutis, Filou and Pateua [Ref. 4.14], who examined failure of laminated plates under biaxial compression-tension.

## 4.5. Concluding Remarks

A new non-empirical micromechanics based two-dimensional finite element model is introduced for predicting the initiation of failure in a laminated fiber composite plate that contains a circular cutout and loaded in multiaxial compression. Based on previous experimental work by the author and a number of other investigators, it is now established that fiber composites containing cutouts fail by kink banding occurring close to the cutout edge when subjected to compression (uniaxial), while fiber/matrix debonding is seen to occur with kink banding in specimens that are biaxially loaded. Exploiting the fact that this initial manifestation of damage is a *localized* event (i.e. in experiments surface strain gages placed remote from the cutout, are unaffected by the initial kink band that forms near the cutout-see Khamseh and Waas [Ref. 4.2, 4,16]), the commercial Finite Element package ABAQUS has been used to analyze this local event. Elastic material properties of the constituents and the full uniaxial stress-strain curve of the matrix material are needed as input. As will be discussed in chapter 6 and chapter 7, the in-situ matrix properties do a much better job of capturing the actual matrix response that needs to be used in this type of an analysis.

Consequently, much better agreement with experimental data is reported in chapter 7, based on the limit load.

The combination of a progressively decreasing modulus for the matrix and a nonuniform prekinking stress field whose gradients are uniquely related to the cutout size are sufficient to fully characterize the kink banding. The present model leads to reasonably good predictions for the load carrying capacity of composite plates containing cutouts when loaded in multiaxial compression. The finite element predictions of the salient features of the failure initiation event are found to compare favorably with experimental data. The present model provides a useful predictive tool for design engineers. Additionally, the model may also be used in an inverse manner. The model predictions can be used to understand how to delay kinking failure, for example, by affecting the matrix shear stress-strain response via chemical synthesis of the polymer matrix or by the addition of appropriate inclusions to the matrix.

## 4.6. Tables and Figures

| | $E_{11}$ (ksi) | $E_{22}$ (ksi) | $\nu_{12}$ | $G_{12}$ (ksi) |
|---|---|---|---|---|
| Experiments | 904.3 | 574.6 | 0.36 | NA |
| Theory, Modified rule of mixture | 1017.8 | 548.6 | 0.37 | 186.7 |

**Table 4.1 Laminate material Property**

| Specimen | Hole Size d/$L$, ($d/2$) inches | Exp. Far Field Stress in x direction (psi) | FEA Prediction Based on Plateau Load (psi) |
|---|---|---|---|
| 1 | 0.062, 0.0520 | 6,600 | 6,646 |
| 2 | 0.103, 0.0864 | 4,833 | 5,320 |
| 3 | 0.144, 0.1207 | 4,275 | 4,859 |
| 4 | 0.198, 0.1660 | 3,800 | 4,525 |

**Table 4.2 Comparison of FEA predictions with experiment (Uniaxial Loading)**

| Specimen | Hole Size $d/L$, $(d/2)$ inches | Exp. Far Field Stress in x direction (psi) | FEA Prediction Based on Plateau Load (psi) |
|---|---|---|---|
| 1,2 | 0.062, 0.0520 | 10,400, 10,800 | 10,507 |
| 3,4 | 0.103, 0.0864 | 9,600, 10,000 | 9,846 |
| 5,6 | 0.144, 0.1207 | 9,000 | 9,215 |
| 7,8 | 0.198, 0.1660 | 7,500, 7,000 | 7,730 |

Table 4.3 Comparison of FEA predictions with experiment (Biaxial Loading)

| Mesh Used | Dimensions X length x Y length | Imperfection Magnitude (maximum deflection in Y) | Maximum Resultant Stress in Microregion (Ksi) | Plateau Stress in Microregion (Ksi) |
|---|---|---|---|---|
| Baseline | 300 $d_f$ x 142 $d_f$ | 1.81 $d_f$ | 37 | 29 |
| Mesh A | 375 $d_f$ x 142 $d_f$ | 1.81 $d_f$ | 37 | 28 |
| Mesh B | 300 $d_f$ x 177 $d_f$ | 1.81 $d_f$ | 37 | 27 |
| Mesh C | 375 $d_f$ x 177 $d_f$ | 1.81 $d_f$ | 37 | 26 |
| Mesh D | 450 $d_f$ x 213 $d_f$ | 1.81 $d_f$ | 37 | 29 |

Table 4.4 Results of the mesh convergence study. $d/L$ = 0.3, $d/2$ = 0.25 in.
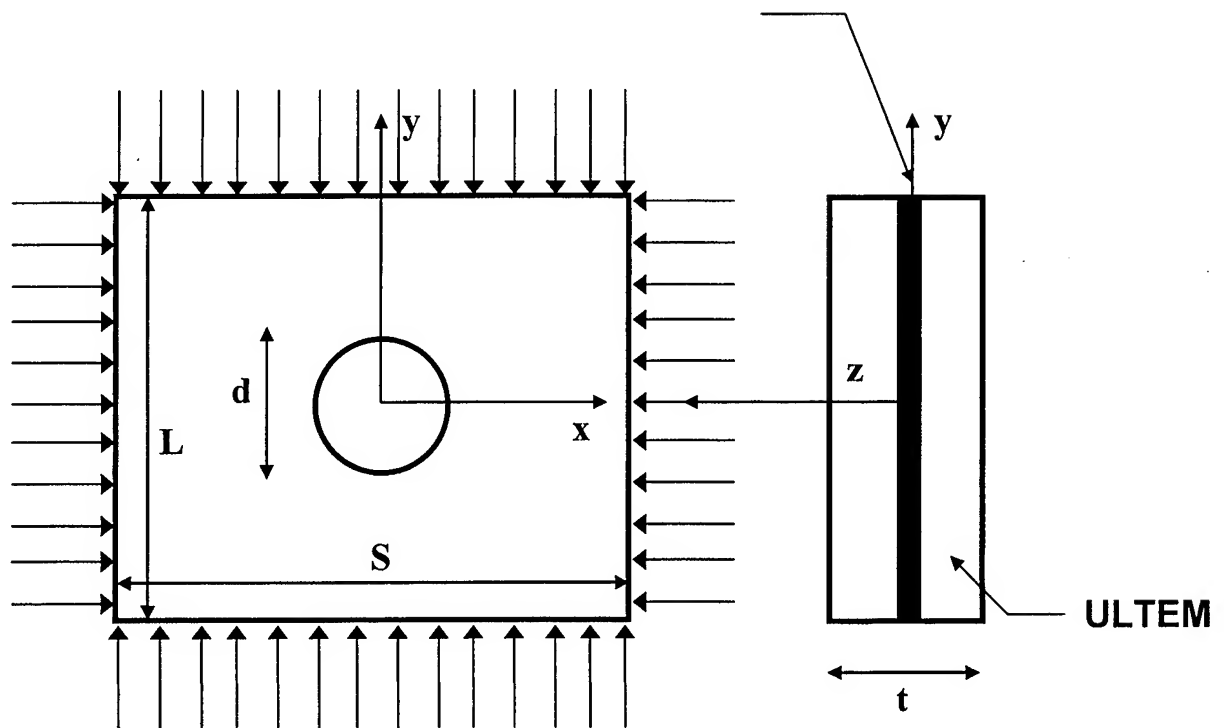
# Graphite / Polymer Single Ply
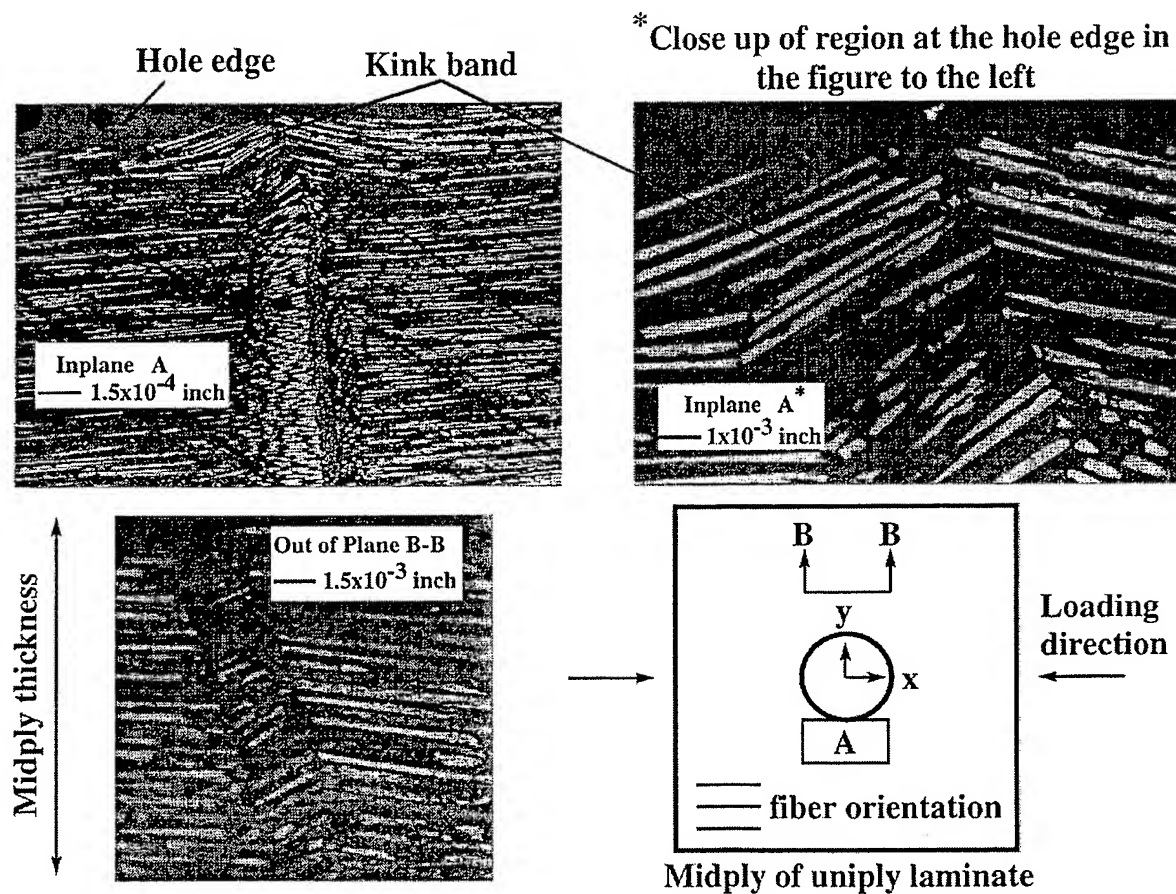


**Figure 4.1 Test Specimen**

Hole edge    Kink band

*Close up of region at the hole edge in
the figure to the left

Inplane A
—— $1.5 \times 10^{-4}$ inch

Inplane A*
—— $1 \times 10^{-3}$ inch

Midply thickness

Out of Plane B-B
—— $1.5 \times 10^{-3}$ inch

B    B

y

x

Loading
direction

A

—— fiber orientation

Midply of uniply laminate

**Figure 4.2 Photomicrograph of typical kink band locations; a) uniaxial loading
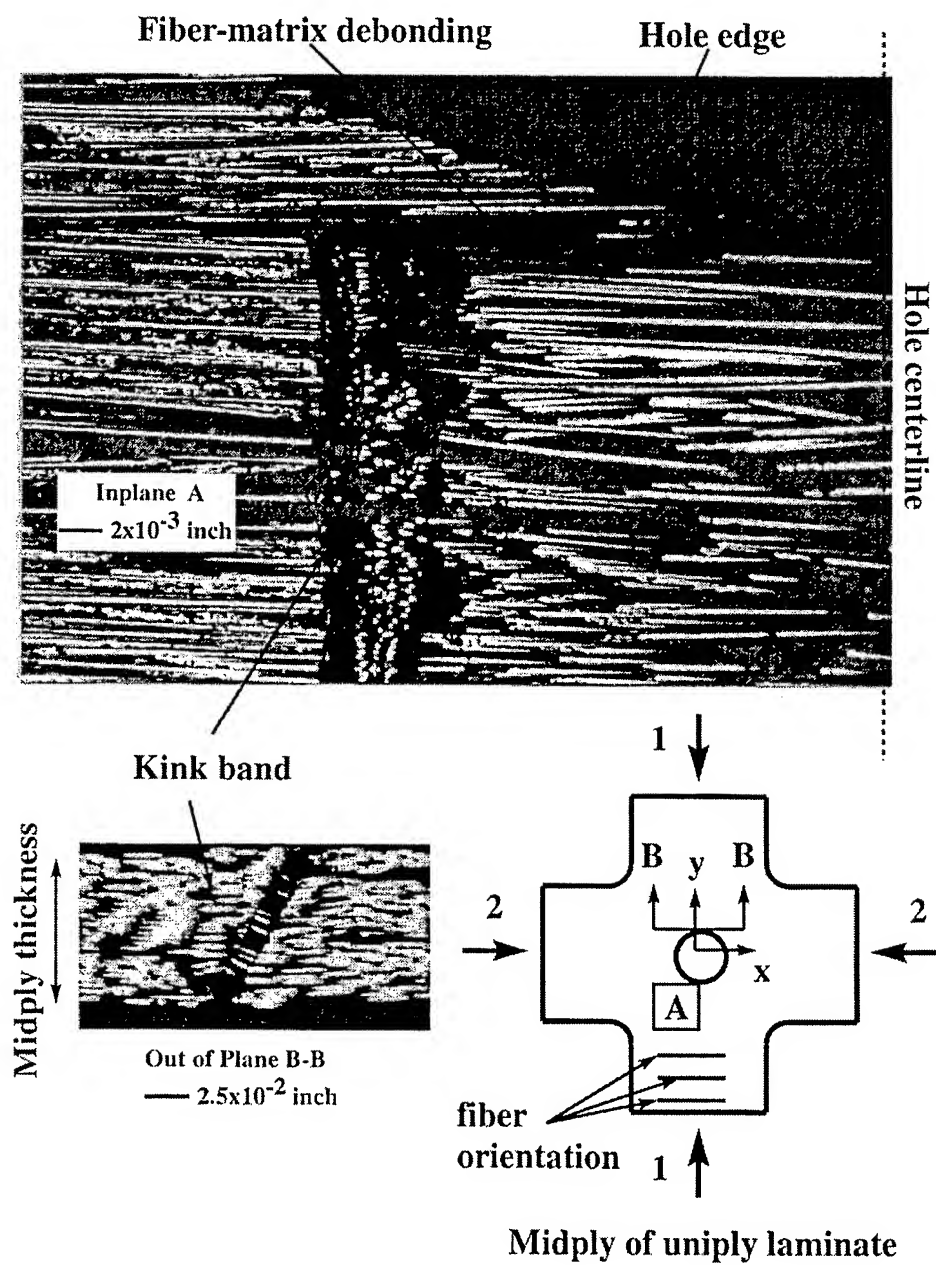[Ref. 4.2]**

Figure 4.2 Photomicrograph of typical kink band locations; b) biaxial loading [Ref. 4.2], continued
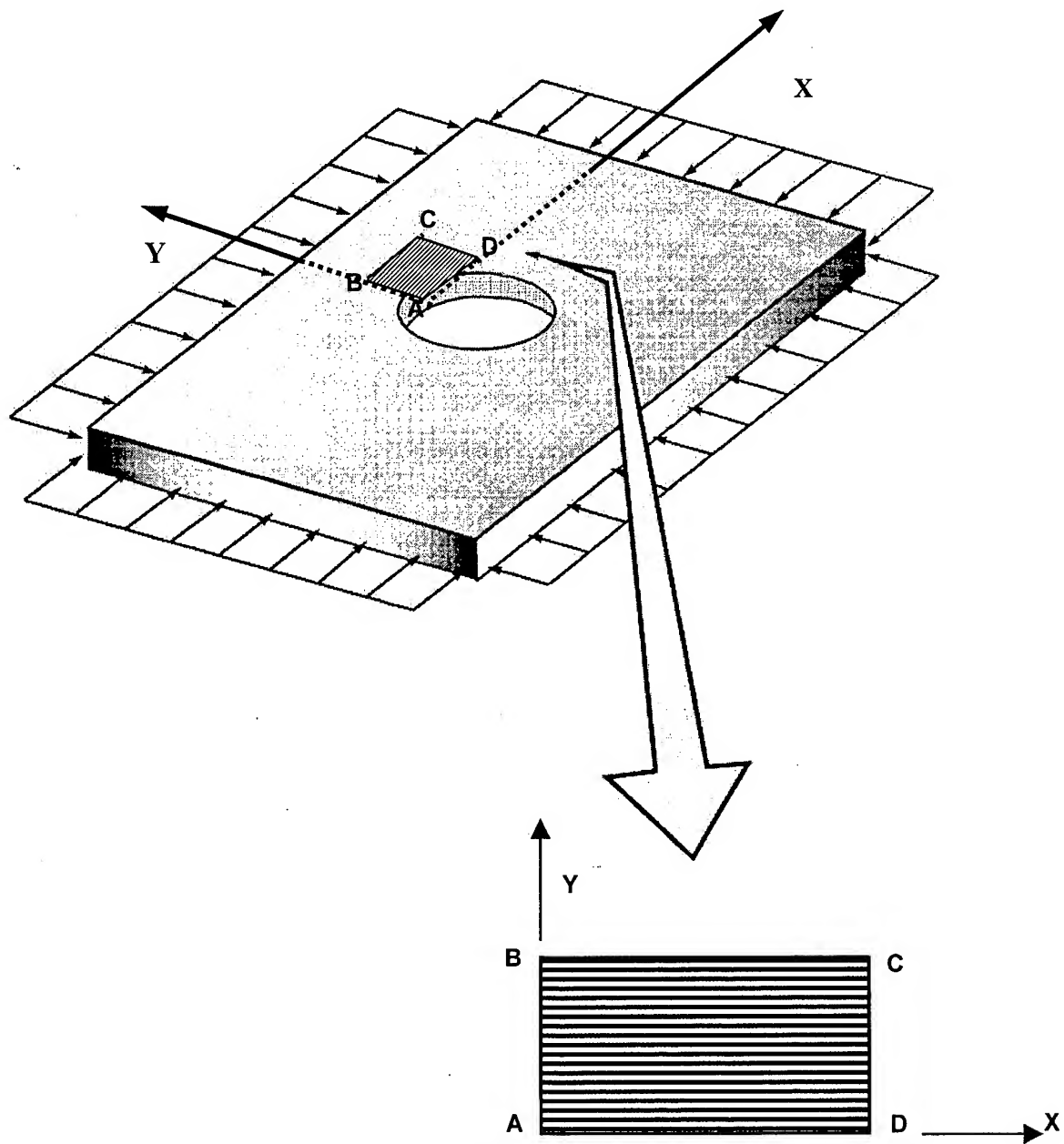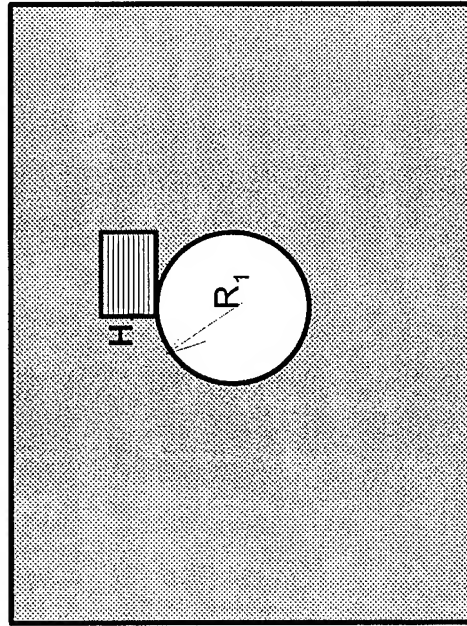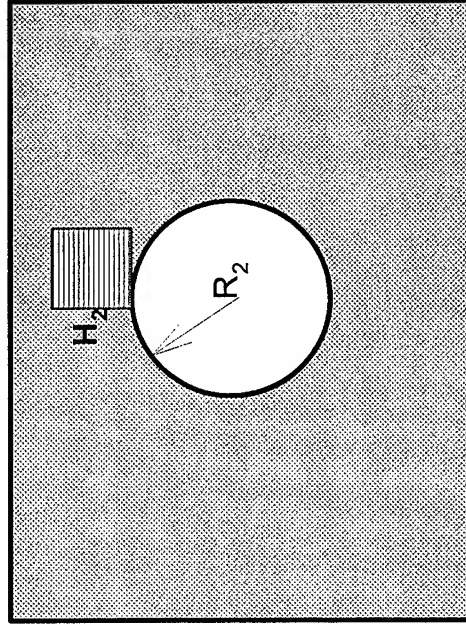
91

**Figure 4.3 Region Studied by FEA**

**Scaled model**

$H_2$

$R_2$

$H_2 = K_u \times R_2$ (uniaxial)

$H_2 = K_b \times R_2$ (biaxial)

**Baseline Model**

$H$

$R_1$

$H / R_1 = K_u$, (Uniaxial)

$H / R_1 = K_b$, (Biaxial)

**Figure 4.4 Mesh Sizing**

93

| Hole Aspect Ratio (2R / L) | W = 300 $d_f$ , H = 142 $d_f$<br>Mesh Result (psi) | Scaled Mesh Result (psi) | Test Result (psi) |
|---|---|---|---|
| 0.062 | 6,646 | 6,646 (b = 142 $d_f$) | 6,600 |
| 0.103 | 6,500 | 5,320 (b = 235 $d_f$) | 4,833 |
| 0.144 | 6,100 | 4,859 (b = 329 $d_f$) | 4,275 |
| 0.198 | 5,828 | 4,525 (b = 453 $d_f$) | 3,800 |

* **Lower bound for maximum Far Field Stress (0.1 % imperfection : max 2.5 $d_f$ waviness)**

$$H_{ref} / R_{ref} = K$$

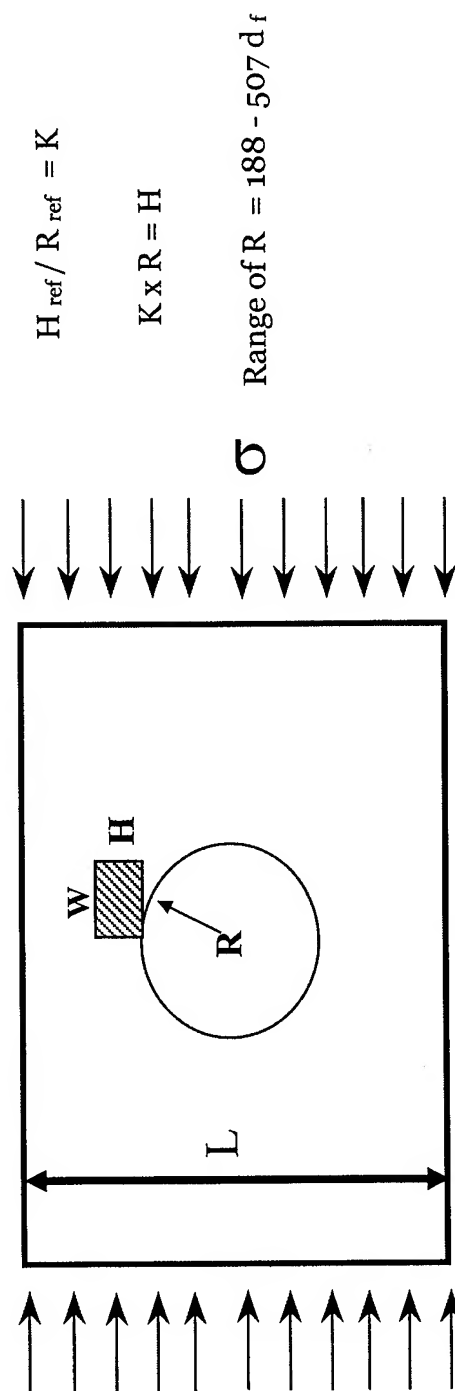$$K \times R = H$$

Range of R = 188 - 507 $d_f$
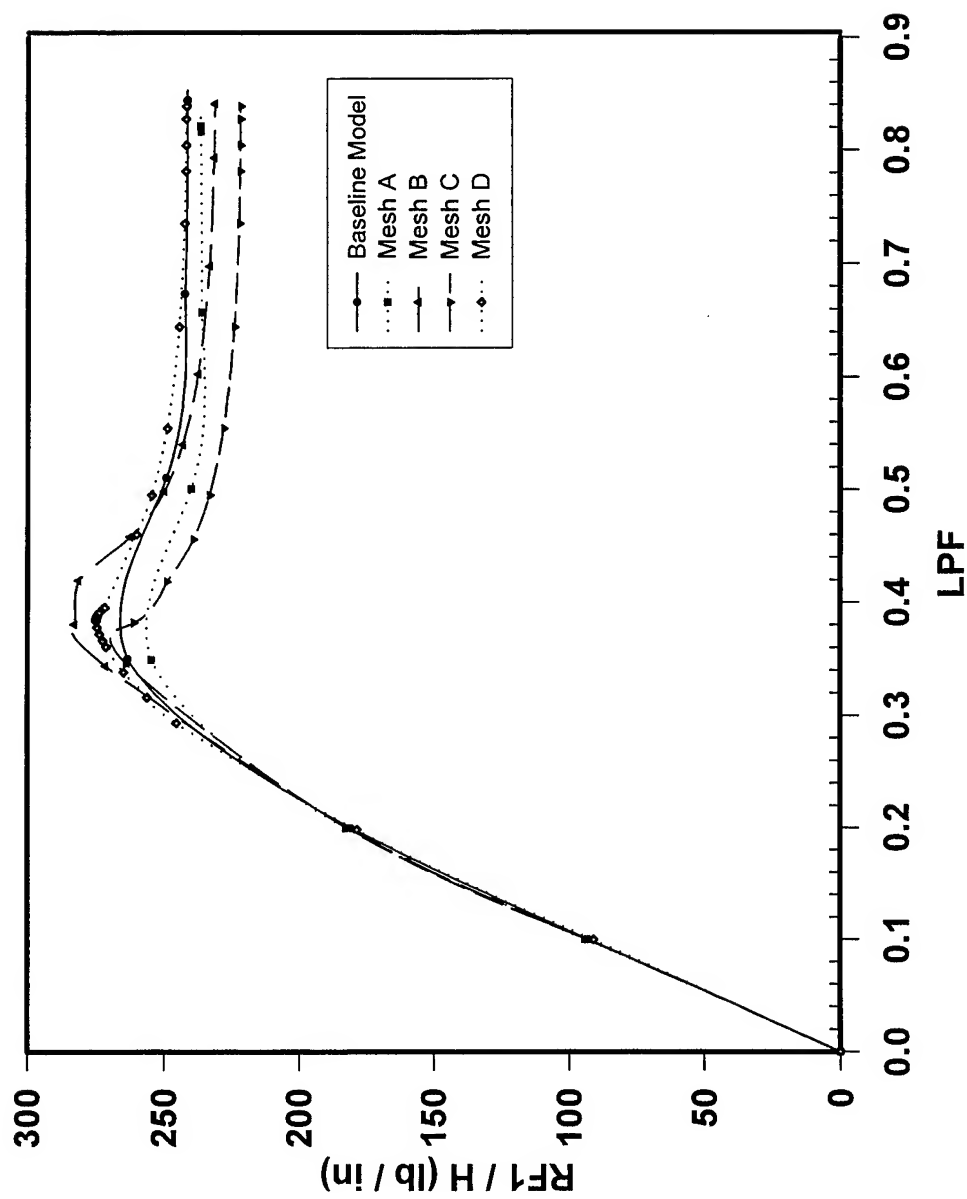


**Figure 4.5 Mesh Sizing Detail (Uniaxial)**

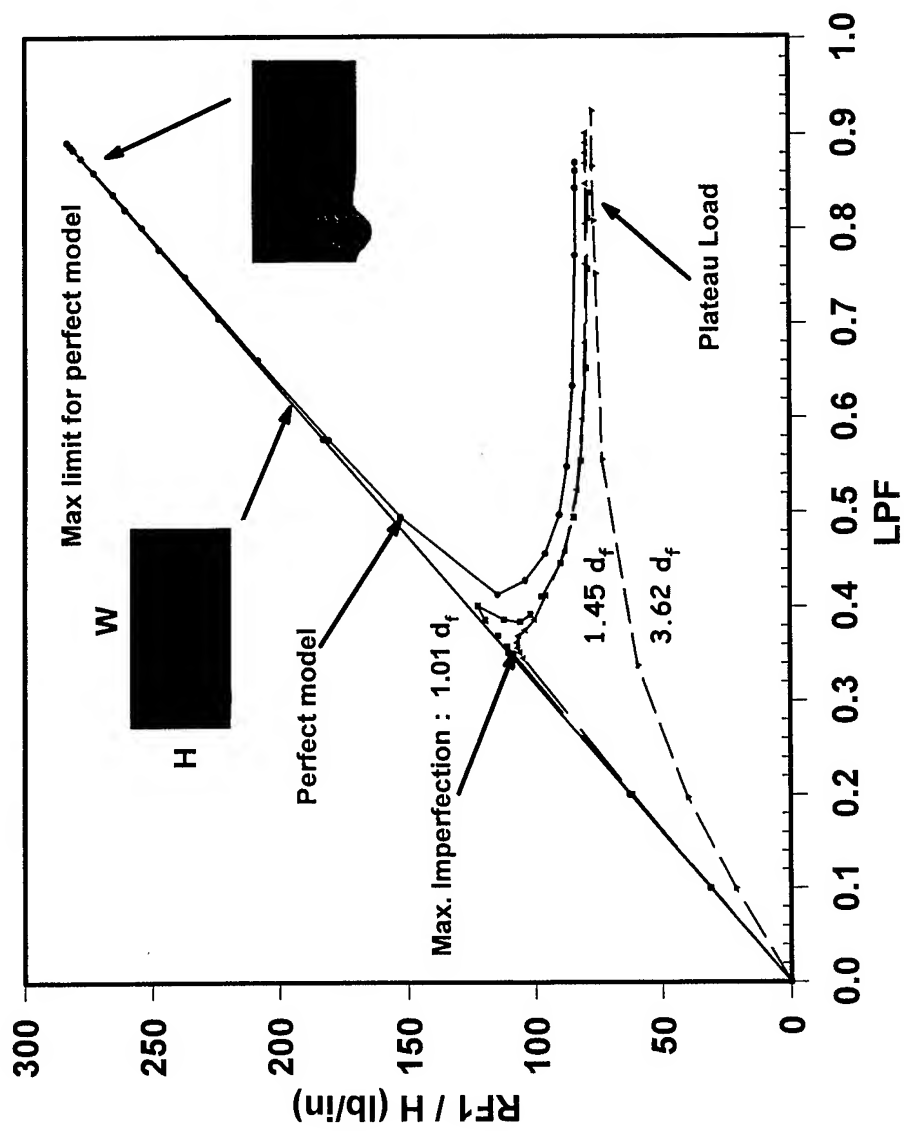Figure 4.6 Effect of Mesh Size on Load-Shortening Behavior of Micro-region

95

Figure 4.7 Typical response curves showing trend between total resultant homogenized reaction force (RF1 / H) vs. Load Proportionality Factor (LPF), for the uniaxial case

96

**Specify u(x), v(x)**

**Specify u(y), v(y)**

**Specify Equilibrium Traction**

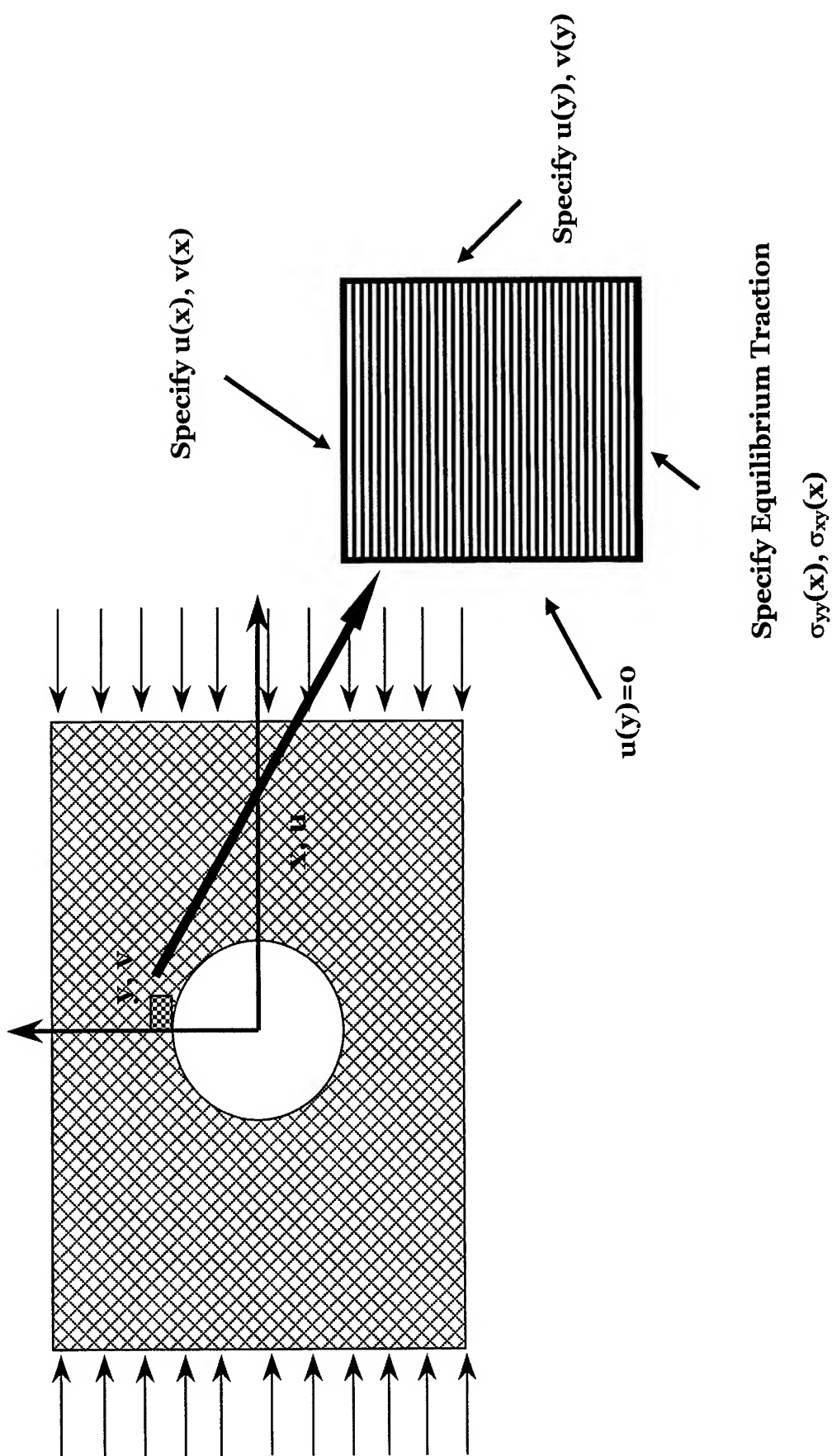$\sigma_{yy}(x)$, $\sigma_{xy}(x)$

u(y)=0

Figure 4.8 FEA Model Boundary Condition (displacement distribution follows Figure 3.5, traction forces were estimated from the result of static analysis based on displacement distribution in Figure 3.5)
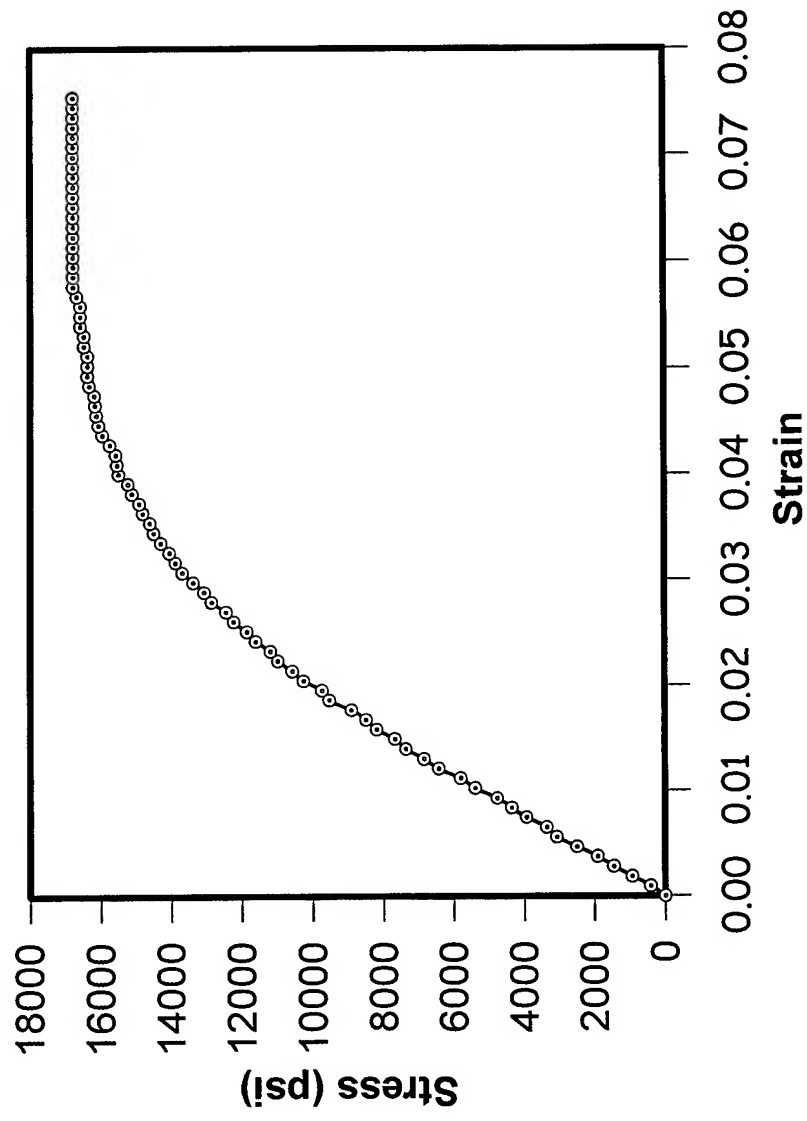
97

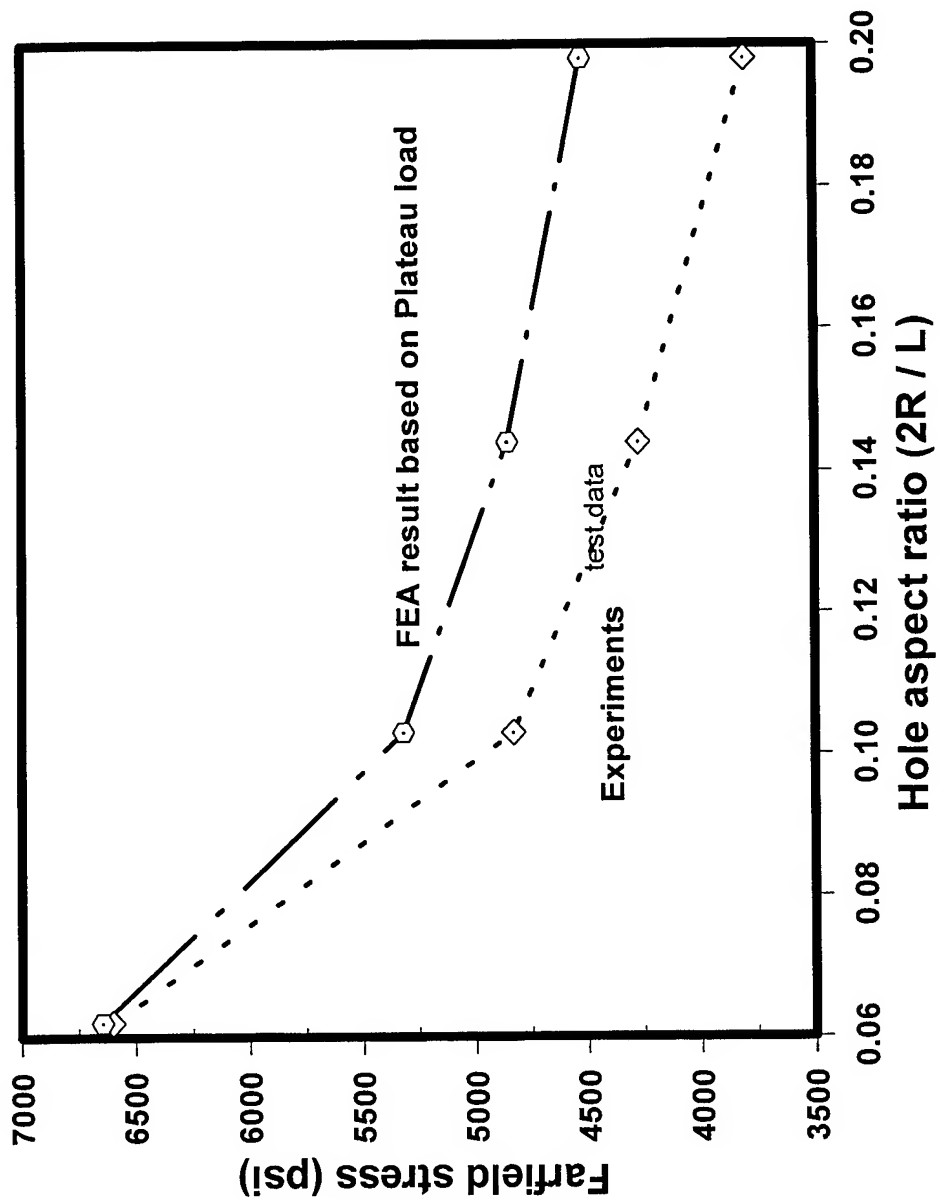Figure 4.9 Uniaxial Compression Stress-Strain Curve for the Matrix Material

98

Figure 4.10 Uniaxial Experimental Result vs. Present Analysis of the Uniply Test Specimens Studied by Khamseh and Waas [Ref. 4.2]
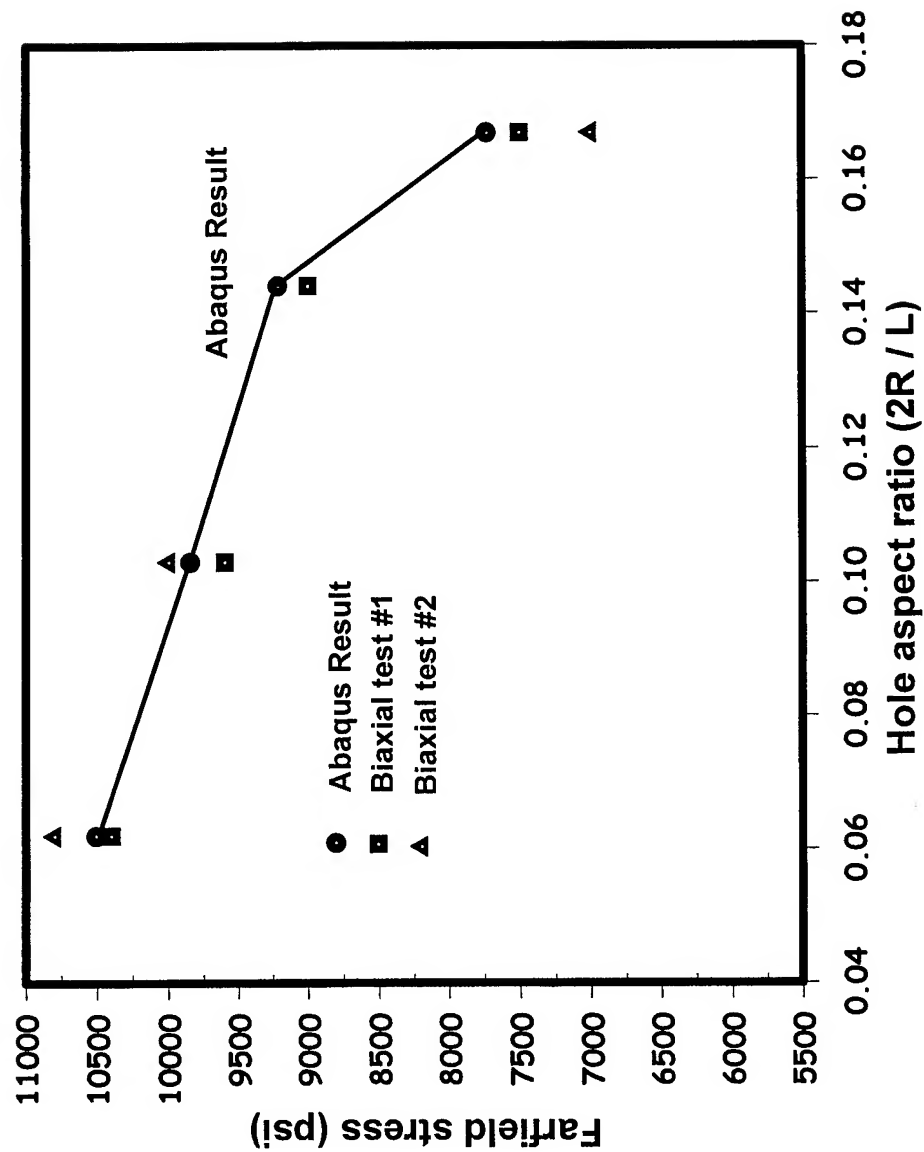
Figure 4.11 Biaxial Experimental Result vs. Present Analysis of the uniply test specimen studied by Khamseh and Waas [Ref. 4.2]

100

## 4.7. References

1. Ahn J. H. & Waas A. M., 1999, "A Micromechanics-Based Finite Element Model for Compressive Failure of Notched Uniply Composite laminates Under Remote Biaxial Loads", *Journal of Engineering Materials and Technology*, Vol. 121, 360-366.

2. Khamseh A. R. & Waas A. M., 1992, "Failure mechanisms in Uniply Composite Plates under Uniaxial Compression", ASME *Journal of Engineering Materials and Technology*, Oct., Vol. 114 650-659

3. Waas A. M., Babcock Jr., C. D., 1986, "Observation of the Initiation and Progression of Damage in Compressively Loaded laminated Plates" GLACIT SM Report 86-34, CALTECH Aeronautics Department, Pasadena, CA 91125

4. Waas A. M., Babcock jr. C. D. & Knauss W. G., 1990, "An Experimental Study of Compression Failure of Fibrous Laminates in the Presence of Stress Gradient", Int. J. Solids and Structure, Vol. 26, No. 9/10, 1071-1098

5. Soutis C. & Fleck N. A., 1990, "Static Compression Failure of Carbon Fiber T800/924C Composite Plate with a Single Hole", J. Composite Materials, Vol. 24. 536-558

6. Riks E., 1972, " The Application of Newton method to the Problems of Elastic Stability", ASME Journal of Applied Mechanics, Vol. 39, 1060-1066

7. Budiansky, B. & Fleck, N. A., 1993, "Compressive Failure of Fiber Composites", J. Mech. Phys. Of Solids, Vol. 41, No. 1, 183 – 200.

8. Kyriakides, S., Arseculeratne, R., Perry, E. J., and Liechti, K. M., 1995, "On the Compressive Failure of Fiber Reinforced Composites", *Int. J. Solids Structures*, Vol. 32, No. 6/7, 689-738

9. Iarve, E., 1997, "3D Stress Analysis in Laminated Composites with Fasteners based on the B-Spline Approximation", *Composites*: A, Vol. 28A, 559-571

10. Soutis, C., Curtis, P., and Fleck, N., 1991, Compressive Failure of Notched Carbon Fiber Composites, Proc. Royal Soc., London, Series A, Vol. 440, 241-256

11. Soutis, C., Fleck, N., and Smith, F., 1991, "Failure Prediction Technique for Compression Loaded Carbon Fiber-Epoxy Laminate with an Open Hole", J. Composite Materials, Vol. 25, 1476-1498

12. Soutis, C., 1997, "The Compressive Behavior of GFRP Laminates", ASTM STP1242, 168-176

13. Soutis, C., & Tenchev, R., 1995, "A Property Degradation Model for Fiber Microbuckling Failure in Composite Laminates", Sci. and Eng. Of Comp. Matrls. , 27-34

14. Soutis, C., Filou, A., and Pateau, R., 1998, "Strength Prediction of CFRP Plates with a Hole Under Biaxial Compression-Tension", AIAA/ASME/ASCE/AHS/ASC Structures, Structural Dynamics and Materials Conference, AIAA CP98-1701,AIAA Headquarters, VA

15. Kyriakides, S., and Ruff, A. E., 1996, "Aspects of the Failure and Post Failure of Fiber Composites in Compression", *J. Composite Materials,* in Press.

16. Khamseh, A. R., and Waas, A. M., 1997, "Failure Mechanisms of Composite Plates with a Circular Hole under remote Biaxial Planar Compressive Loads", *ASME Journal of Engineering Materials and Technology,* Vol. 119, 56-64

# CHAPTER 5

# MICROMECHANICS MODEL TO PREDICT FAILURE OF ANGLE PLIES AS A FUNCTION OF PLY ANGLE

## 5.1. Introduction

In chapter 4 of this thesis, the kink banding failure mode was analyzed by using a micromechanical based finite element analysis using test results for uniply specimen studied by Khamseh and Waas [Ref. 4.2]. The input data for that model were the fiber mechanical properties, the uniaxial stress-strain response of the matrix, the fiber geometric properties, the spacing between fibers and the stacking sequence of the laminate. In chapter 2 of this thesis, it was stated that the dominant mode of failure for the angle ply and quasi-isotropic laminates was a fiber/matrix interface failure. Thus, in general, for laminates where zero plies co-exist with other angle plies or where there are no zero plies, the possibility of fiber / matrix interface failure must be incorporated into any predictive analysis capability. The objective of this chapter is to develop a micromechanics based finite element analysis of angle ply laminates that are loaded uniformly in compression. Because the dominant loading in compression is with respect to the fiber direction, the stress states within a single lamina, in the material principal coordinate directions now involve $\sigma_1$ (in the fiber direction), $\sigma_2$ (perpendicular to

the fiber direction) and $\tau_{12}$ (shear) (Figure 5.1). Thus, the onset of instability of such an angle ply occurs in the presence of a combined planar stress state. The main hypothesis used in the failure analysis of angle ply lamina is that the different types of failure modes seen in the experiments with angle ply lamina are associated with a structural instability in the presence of material nonlinearity that manifests itself in the form of kink banding, inplane matrix shearing and matrix compression failure. As will be shown, the failure mode undergoes a transition between these three dominant failure mechanisms as a function of ply angle. Thus, as presented here, for the first time, a non-empirical mechanics based model that is able to provide an interpretation for the different mechanisms of failure is introduced. The intention of this chapter is to expand on the effect of ply angle on the failure mode. This chapter is not intended as model for the notched angle ply laminate experimental results. Instead, this chapter uses experimental data available elsewhere [Shuart, Ref. 5.3]. The reader may skip this chapter and proceed with an uninterrupted reading of this thesis.

## 5.2. Previous Work

Previous work examined failure of angle ply laminates by focusing on the macroscopic state of shear in a compressively loaded laminate. Rosen [Ref. 5.1] and Kim [Ref. 5.2] conducted analytical and experimental studies respectively of angle ply laminates and found that shear failure mechanisms were significant. Shuart [Ref. 5.3] conducted a careful and systematic experimental study on the compression failure of $(+\theta/-\theta)_{ns}$ multidirectional laminates. Shuart [Ref. 5.3] was

able to identify the transition of failure between kink banding (which he also called fiber brooming, since sometimes the laminate broke along the band which was formed near the boundary of the loaded edge), inplane matrix shearing and matrix compression. No unifying model was introduced to capture the different regimes of failure. Instead, different models were constructed to explain the different failure mechanism, which changes as a function of ply angle. However, a complete set of experimental data was presented to show the different mechanisms of failure. Shuart's experimental data for laminate failure have been used here as a benchmark for the trends to be expected when investigating compressive failure of angle ply lamina. In analyzing angle ply lamina, the same material properties will be used for the matrix as used in chapter 4 for the uniply material study, to obtain a complete set of results for the angle ply lamina. Shuart's work did not include neat resin properties, however the shear stress vs. shear strain curve for a $(\pm 45)_{ns}$ laminate was provided. At the time of completing the finite element analysis reported here-in, we were not aware of Shuart's work, thus, the material properties corresponding to the G30-500 BASF Fiber/F155 Epoxy prepeg which was used in the uniply test specimen of Khamseh and Waas [Ref. 4.2] was used. However, for comparison purpose, the matrix shear stress-strain curve of the AS4/3502 system have been included, backed out of the $(\pm 45)_{ns}$ shear stress-shear strain data reported in Shuart [Ref. 5.3], using the procedure described in chapter 6. In that same figure (Figure 5.8, to be discussed later), the neat resin properties of the F-155 epoxy are also included. It is the

105

latter properties in conjunction with a $J2$ small strain flow theory of plasticity that was used to model the matrix, for the results reported here.

## 5.3. Mechanical Model for Compressive Response of an Angle ply Lamina

The configuration studied is as shown in Figure 5.2, where an angle-ply laminate $(+\theta/-\theta)_{ns}$ is subjected to uniform compression loading. The (x, y) axis denotes lamina principal axis, and the (1, 2) axis denotes principal material axis. A microregion with dimension H x L is of interest for the finite element analysis. First, the compliances of a lamina in the $x$-$y$ coordinate frame are related to the principal compliances in the 1-2 coordinate frame by

$$S_{xx} = m^4 S_{11} + n^4 S_{22} + 2m^2 n^2 S_{12} + m^2 n^2 S_{66}$$

$$S_{yy} = n^4 S_{11} + m^4 S_{22} + 2m^2 n^2 S_{12} + m^2 n^2 S_{66}$$

$$\text{(5.1)}$$

$$S_{xy} = m^2 n^2 S_{11} + m^2 n^2 S_{22} + \left(m^4 + n^4\right) S_{12} - m^2 n^2 S_{66}$$

$$S_{ss} = 4m^2 n^2 S_{11} + 4m^2 n^2 S_{22} - 8m^2 n^2 S_{12} + \left(m^2 - n^2\right)^2 S_{66}$$

where, $m = cos\ \theta$, $n = sin\ \theta$. Next, classical lamination theory is used to find the laminate engineering properties $E_{xx}$, $E_{yy}$, $G_{xy}$ and $v_{xy}$. Using these and a loading condition of unit compressive stress in the $x$ direction, the laminate strain can be found from

$$\begin{bmatrix} \varepsilon_{xx} \\ \varepsilon_{yy} \\ \gamma_{xy} \end{bmatrix} = \begin{bmatrix} \dfrac{1}{E_{xx}} & -\dfrac{V_{xy}}{E_{xx}} & 0 \\ \dfrac{V_{xy}}{E_{xx}} & \dfrac{1}{E_{yy}} & 0 \\ 0 & 0 & \dfrac{1}{G_{xy}} \end{bmatrix} \begin{bmatrix} \sigma_{xx} = -1 \\ \sigma_{yy} = 0 \\ \sigma_{xy} = 0 \end{bmatrix} \tag{5.2}$$

Having obtained the strain in the $x$-$y$ coordinate frame, it is necessary to transform the laminate strains to the $1$-$2$ coordinate frame, since the finite element analysis is carried out in the principal material coordinates. This is achieved via (5.3) and (5.4), which show the necessary transformation.

$$\begin{bmatrix} \varepsilon_{11} \\ \varepsilon_{22} \\ \dfrac{1}{2}\gamma_6 \end{bmatrix} = [T] \begin{bmatrix} \varepsilon_{xx} \\ \varepsilon_{yy} \\ \dfrac{1}{2}\gamma_{xy} \end{bmatrix} \tag{5.3}$$

Where [T] is,

$$[T] = \begin{bmatrix} m^2 & n^2 & 2mn \\ n^2 & m^2 & -2mn \\ -mn & mn & m^2 - n^2 \end{bmatrix} \tag{5.4}$$

In the finite element analysis that follows, the microregion is fixed at the origin of the principal material coordinate frame, since the displacements are measured with respect to this point. Then, the displacement fields corresponding to the strain state (5.3) and (5.4) are given by

$$u(x,y) = \varepsilon_{11}\left(x - \frac{w}{2}\right) + \frac{\gamma_{12}}{2}\left(y - \frac{H}{2}\right)$$

$$v(x,y) = \varepsilon_{22}\left(y - \frac{H}{2}\right) + \frac{\gamma_{12}}{2}\left(x - \frac{w}{2}\right) \tag{5.5}$$

Using (5.5), the displacements corresponding to the node location of the boundary of the microregion were computed, to be used in the finite element analysis that follows.

## 5.4. FEA Modeling

The region to be analyzed using the FEA is as shown in Figure 5.2, where a rectangular domain of dimension H (120 $d_f$ : fiber diameter) x L (70 $d_f$) of alternate layers of fiber and matrix are considered in a plane-strain setting. The matrix layers have a thickness that provide the correct overall fiber volume fraction, $V_f$ = 55 %, in the present case.

The fiber is modeled as an elastic solid with the properties as indicated in Table 5.1 and the matrix is modeled as a elastic-plastic isotropic solid which undergoes finite deformation, obeying the J2 flow theory of plasticity with isotropic hardening. The uniaxial stress-strain response of the matrix is as indicated in Figure 5.3. The fiber and matrix layers are discretized with the CPS4 finite element using the commercial code ABAQUS®. The total number of degree of freedom for the model is approximately 5,754, which consist of 1,498 fiber and 1,242 matrix elements.

To compute the displacement data on the boundaries of the microregion, the far-field loading on the angle ply was assumed to be a uniform compression stress ($\sigma_x$ = -1, $\sigma_y$ = 0, $\tau_{12}$=0). Then, the displacements are calculated using the procedure described earlier. In particular, the displacements fields $u(1,2)$, $v(1,2)$ on the boundary of the microregion were computed.

First, a linear static analysis of the microregion when subjected to displacement loading on the boundary was performed. Nodal equilibrium reaction forces at the boundaries were computed from this run. Next, using the Riks method [Ref. 4.6] option available in ABAQUS® [Ref. 5.4], a nonlinear response analysis of the microregion was conducted, using the boundary nodal forces that are equal and opposite to the model reaction forces computed via the linear static run. As loading proceeds, the boundaries of the microregion undergo large rotations. To use nodal force loading, the multi point constraint option (MPC) provided in ABAQUS® was used on the boundaries AB and CD. In effect, this allows the boundaries to remain straight yet undergo the correct global rotation and deformation, while maintaining the equilibrium with the applied boundary loads. During the loading, the boundaries BC and DA of the microregion must be left free to deform into any shape that is in conformity with equilibrium requirements. Thus, deformation localization into bands within the microregion is allowed to develop, yet overall force equilibrium is maintained in the far field. Since the MPC option was used and the microregion size also influences the observed results, a scaling and mesh sensitivity study were also carried out by systematically increasing the overall size of the microregion and performing the analysis as explained before (Figure 5.7).

## 5.5. FEA Results and Interpretation

The results of the static run were verified using the solution of the corresponding linear elastic solution. Load-response analyses were performed for

all 13 different configuration (5° to 65° angle plies). RIKS analysis was performed, where the solution was sought to a proportional loading case, including the possibility of unstable behavior.

As can be seen from the plots (Figure 5.4), the calculated resultant force in the x-direction ($\sigma_x$) - average strain ($\delta_x / L$) curves all show all similar features, but with different interpretations. Initially, the curve is linear, followed by an unstable unloading path from a maximum load for small ply angles ($5° < \theta < 30°$), that eventually asymptotes to a constant value. This result can be explained in conjunction with experimental observations, where a substantial drop in the load accompanies kink band formation at the failure. This result also confirms various experimental results for unidirectional lamina (0° lamina). As the fiber angle increases, the dominant loading is changed from fiber compression to shear deformation, where the matrix state of shear continuously increases in proportion. Now, the shear property of the matrix becomes dominant. Of course, the matrix layers are also subjected to axial compression and transverse compression, but it is the behavior in shear that is useful for interpreting the experimental results. As the ply angle increases, the initial slope of the response curve decreases for the ply angle range ($5° < \theta < 30°$, Figure 5.4), as expected. In addition, the maximum load decreases and the unstable unloading path becomes stable beyond $\theta = 45°$ (Figure 5.5). That is, an abrupt load drop is no longer the case in an experimental setting. Instead, the slope beyond the load maximum indicates stable unloading and corresponding deformation localization into diffused broad bands. Further, in the range of $40° < \theta < 45°$, the initial linear

slope starts to increase. Beyond $\theta = 45^\circ$. The compression transverse to the matrix begins to carry more loads, and the loads on the fiber tend to decrease.

Beyond $\theta = 65^\circ$, a maximum load is no longer observed ($\theta = 70^\circ$ case plotted in Figure 5.5), instead, the loading becomes transverse compression. Response curves indicate a gradual "yield" like behavior of the matrix. In these cases, one immediately sees that the fibers no longer provide additional stiffening to the matrix, since the predominant loading occurs transverse to the fibers. Thus the matrix bears the "brunt" of the load. The plastic behavior of the matrix totally governs the deformation in these cases.

A plot of the maximum (limit) load as a function of ply angle is shown in Figure 5.6. Shuart's experimental data are also indicated for comparison. Two other curves, one corresponding to the limit load obtained with a larger mesh (the dimensions of the region were increased by a factor of 1.25) and the plateau load corresponding to the original baseline mesh are also indicated. The implications of these results and the result of a mesh sensitivity study are discussed next.

## 5.6. Discussion

As is evident in Figure 5.6, the trends predicted by the present analysis based on the plateau load agree with the trends exhibited in the experimental results of Shuart. However, the plateau load is dependent on the size of the region that is meshed. As the size of the mesh region increases, the plateau load decreases, but the maximum (limit) load stays fixed as shown in Figure 5.7. Also note that as the

size of the mesh region increases, the rate at which the plateau load decreases is diminishing. On the other hand, the limit load is a mesh size independent quantity.

In chapter 2, where the notched composites were studied, a physically induced strain gradient was dominating and influential in revealing a mesh size independent result for both the limit load and the plateau load. By contrast, here we have a case of uniform loading, but with coupling between axial and shear deformation. Thus, there is no intrinsic length scale to fix the size of the region in which deformation localizes. However, the initiation of this process is governed by the tangent shear modulus of the matrix, and thus, this maximum (limit) load is independent of the size of the microregion. On the other hand, the plateau load is indicative of the post-localized response that is governed by the width and extent of the region of localization.

Figure 5.8 shows the comparison between Shuart's matrix property and the matrix property that we used. If we scale the limit load result we obtained with the ratio $\dfrac{\left(\tau_{yield}\right)^{P}}{\left(\tau_{yield}\right)^{S}}$, where $\tau_{yield}$ is the yield stress and superscripts are placed to indicate the in-situ stress of 3502 epoxy (Shuart) and p to indicate present (chapter 2). The scaled result compared to the experimental results of Shuart are as shown in Figure 5.9. The comparison is very good. A complete analysis, incorporating the in-situ stress-strain curves of 3502 epoxy is planned for a later time.

Figure 5.10 indicates two series of deformed micro-regions corresponding to $\theta = 30°$ and $\theta = 65°$ and Figure 5.11 indicates the response of FEA model at very low angle (5°) where steep load drop is observed. Notice that, for small angles, the bands of localization are narrow, while as the angle increases the bands are diffused and broad. Just as observed by Shuart, the mechanism of compressive failure at low angles involves kink banding, leading to specimen splitting across the kinked band, while for larger angles (intermediate $30° < \theta < 50°$), there is a transition in the failure mode where kinking does not occur. Instead fiber/matrix interfacial failure dominates. At these angles, the interfacial shear stress is larger than at smaller angles. Thus, this stress component in conjunction with any irregularities at the fiber/matrix interface (such as voids, partial debonding) leads to the onset of interfacial fiber/matrix failure. A complete analysis of this mode (which incorporates computing the energy release rates), necessitates a fracture mechanics based analysis with an accurate knowledge of the critical interfacial energy release rate (measured via suitable experiments as has been done in Song and Waas [Ref. 5.9]). This aspect is not considered in the present thesis, but the reader is referred to Song and Waas [Ref. 5.9] for further details.

## 5.7. Tables and Figures

| Material | $E_{11}$ (Msi) | $\nu_{12}$ | $G_{12}$ (Msi) | Thickness (in) |
|---|---|---|---|---|
| G30-500 BASF Fiber | 33 | 0.25 | 13.2 | $2.756 \times 10^{-4}$ |

**Table 5.1 Fiber Properties**

## Ply angle vs. Stress
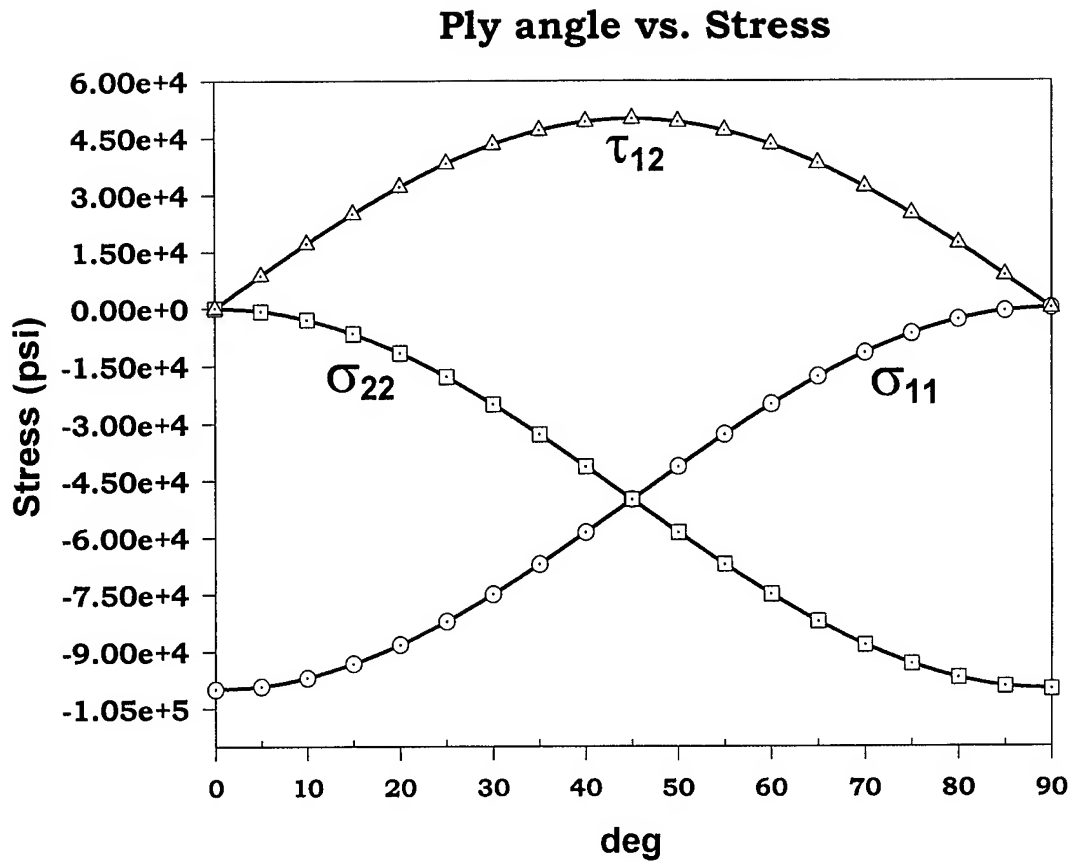


$$
\begin{pmatrix} \sigma_{11} \\ \sigma_{22} \\ \sigma_{12} \end{pmatrix} = \begin{pmatrix} (\cos\theta)^2 & (\sin\theta)^2 & 2\cos\theta\sin\theta \\ (\sin\theta)^2 & (\cos\theta)^2 & -2\cos\theta\sin\theta \\ -\cos\theta\sin\theta & \cos\theta\sin\theta & 2(\cos\theta)^2 - 1 \end{pmatrix} \begin{pmatrix} \sigma_{xx} \\ 0 \\ 0 \end{pmatrix}
$$
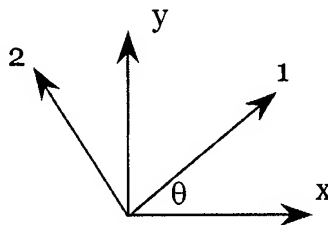
**Figure 5.1 Effect of stress distribution as a function of fiber angle**

$\sigma_x$
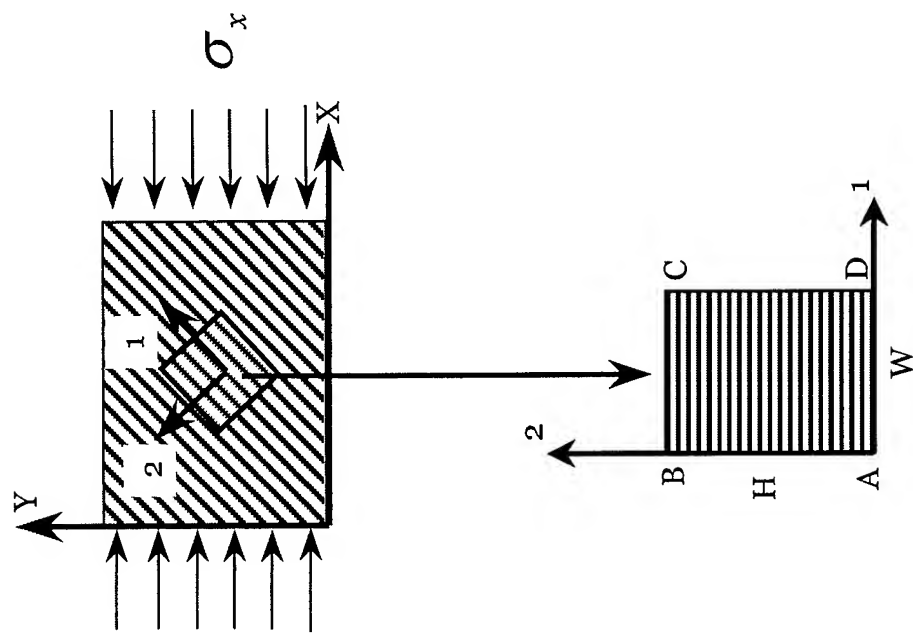
$H = 120\,d_f \quad W = 70\,d_f$

Figure 5.2 Angle ply under uniform compression

116
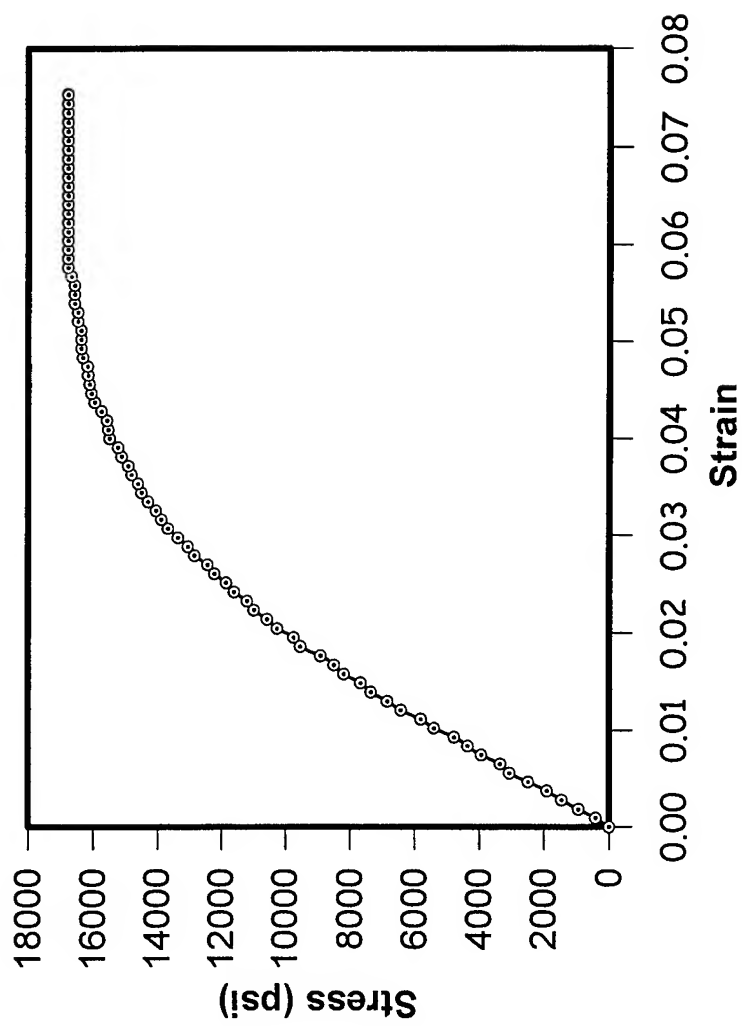
Figure 5.3 Uniaxial stress-strain response of F155 epoxy

117
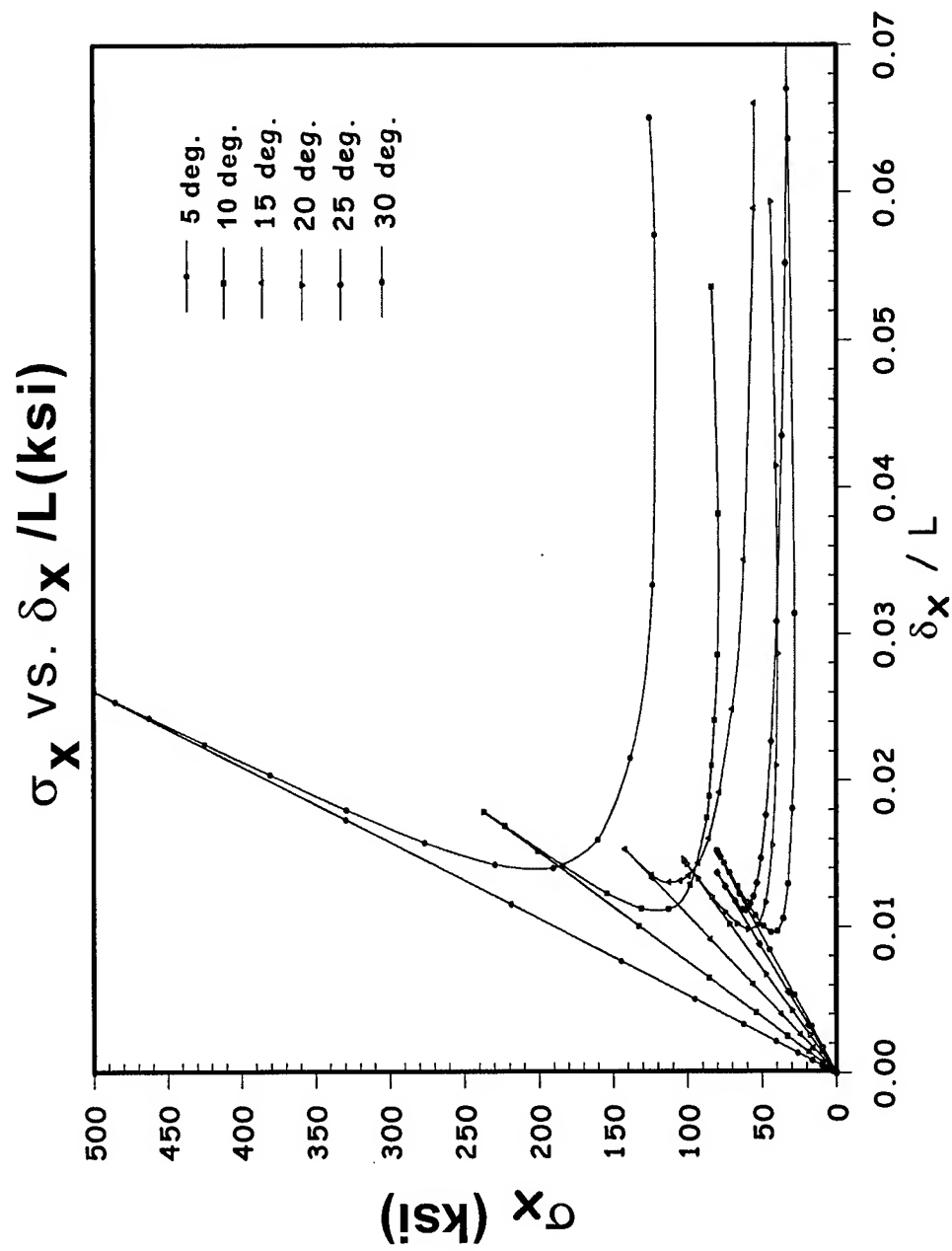
Figure 5.4 Typical response result (5 – 30 degree)

118

$\sigma_x$ vs $\delta_x / L$ (ksi)
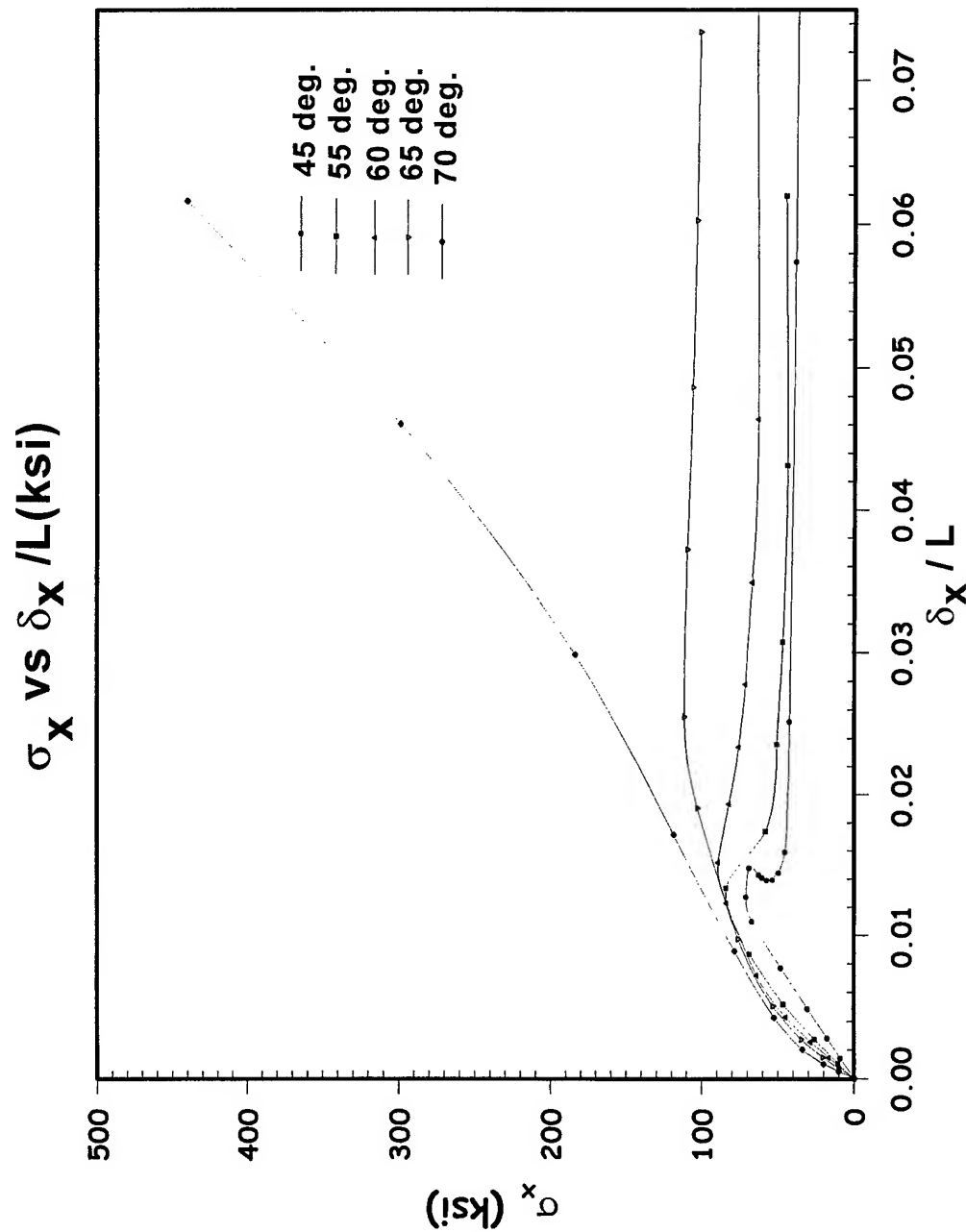
Figure 5.5 Response plots for ply angles in the range of 45 – 70 degree

119
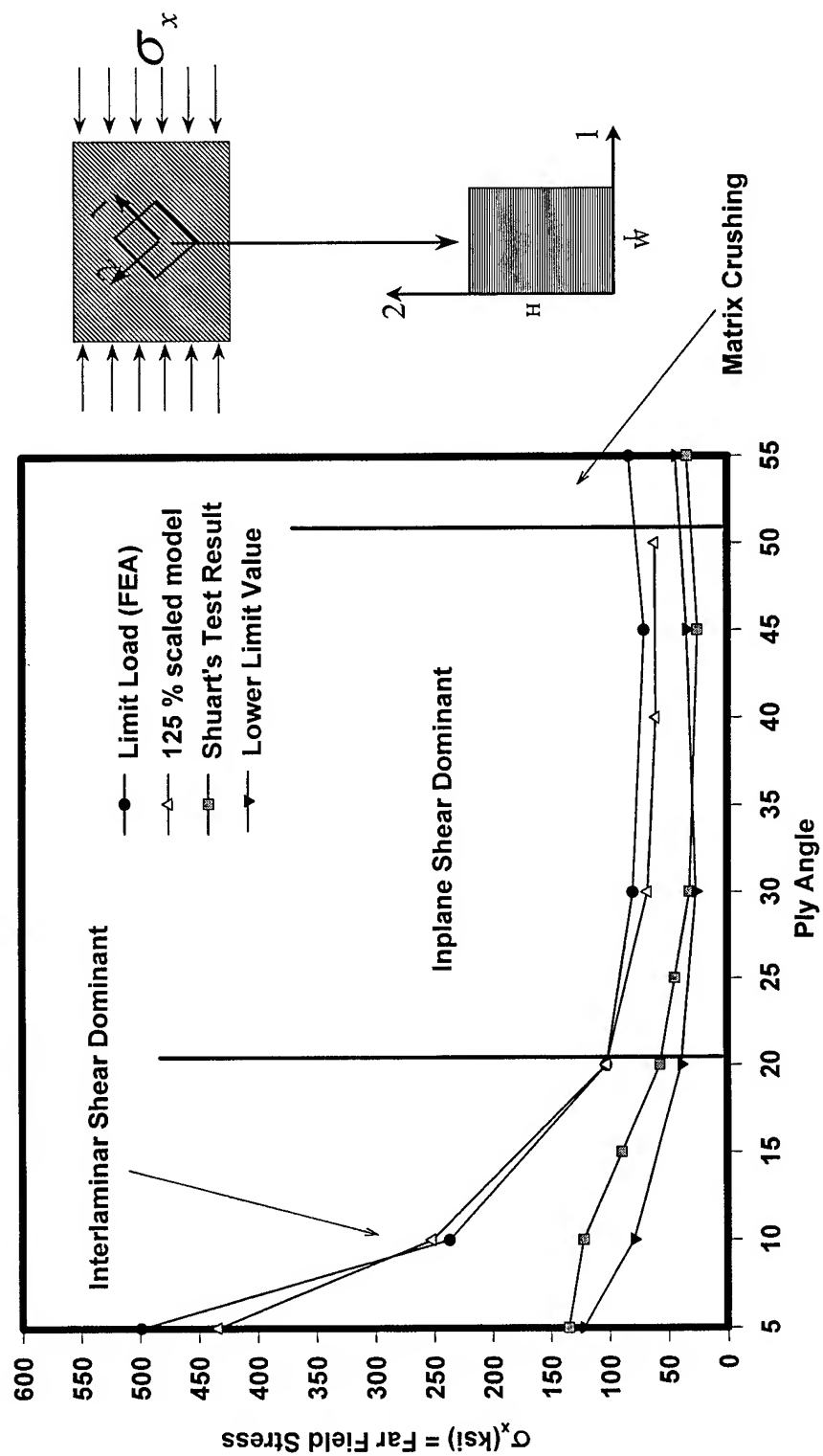
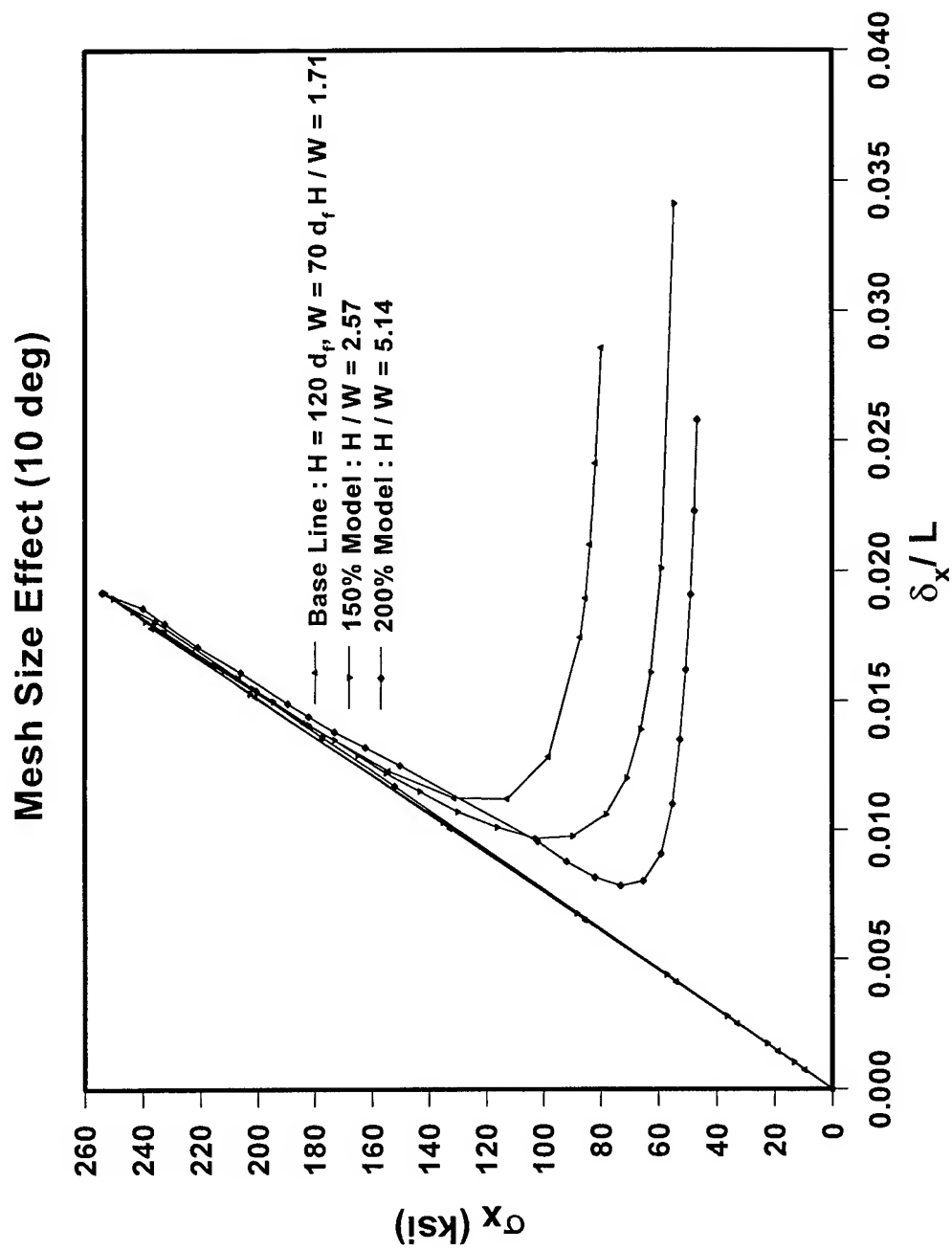Figure 5.6 FEA result and comparison with Shuart's test data
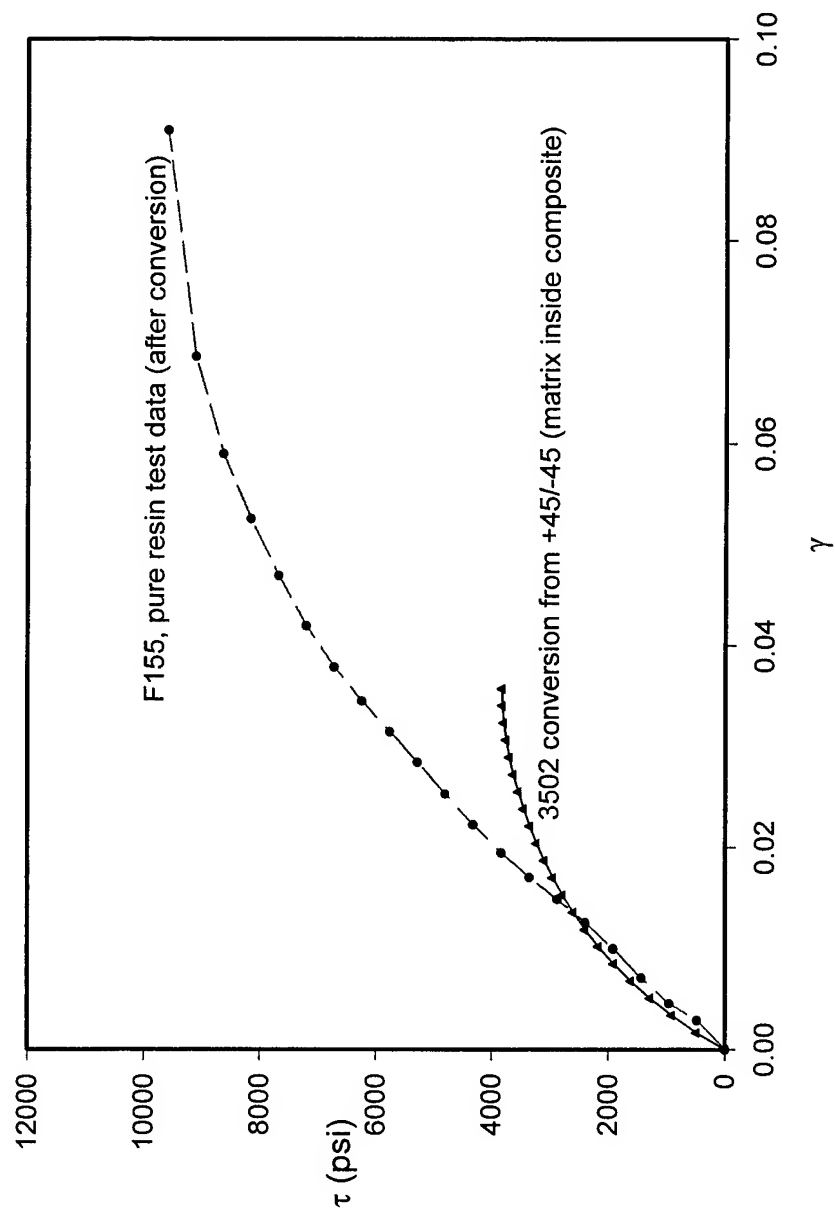
120

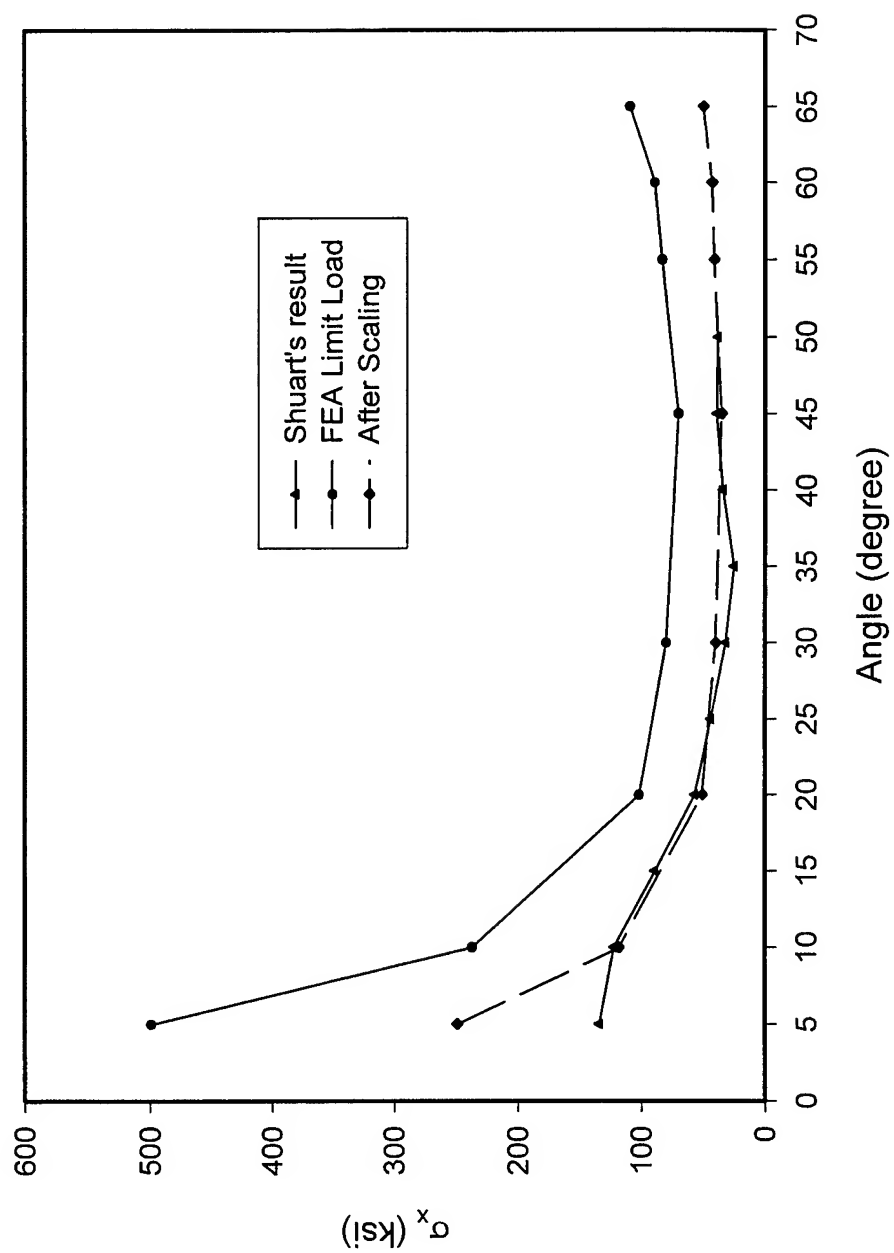Figure 5.7 Effect of mesh size

# F-155 & 3502 Epoxy

F155, pure resin test data (after conversion)

3502 conversion from +45/-45 (matrix inside composite)

$\tau$ (psi)

$\gamma$

**Figure 5.8 Shear response comparison**

Figure 5.9 A comparison of the scaled FEA result against Shuart's test data

123

θ = 30°

θ = 65°
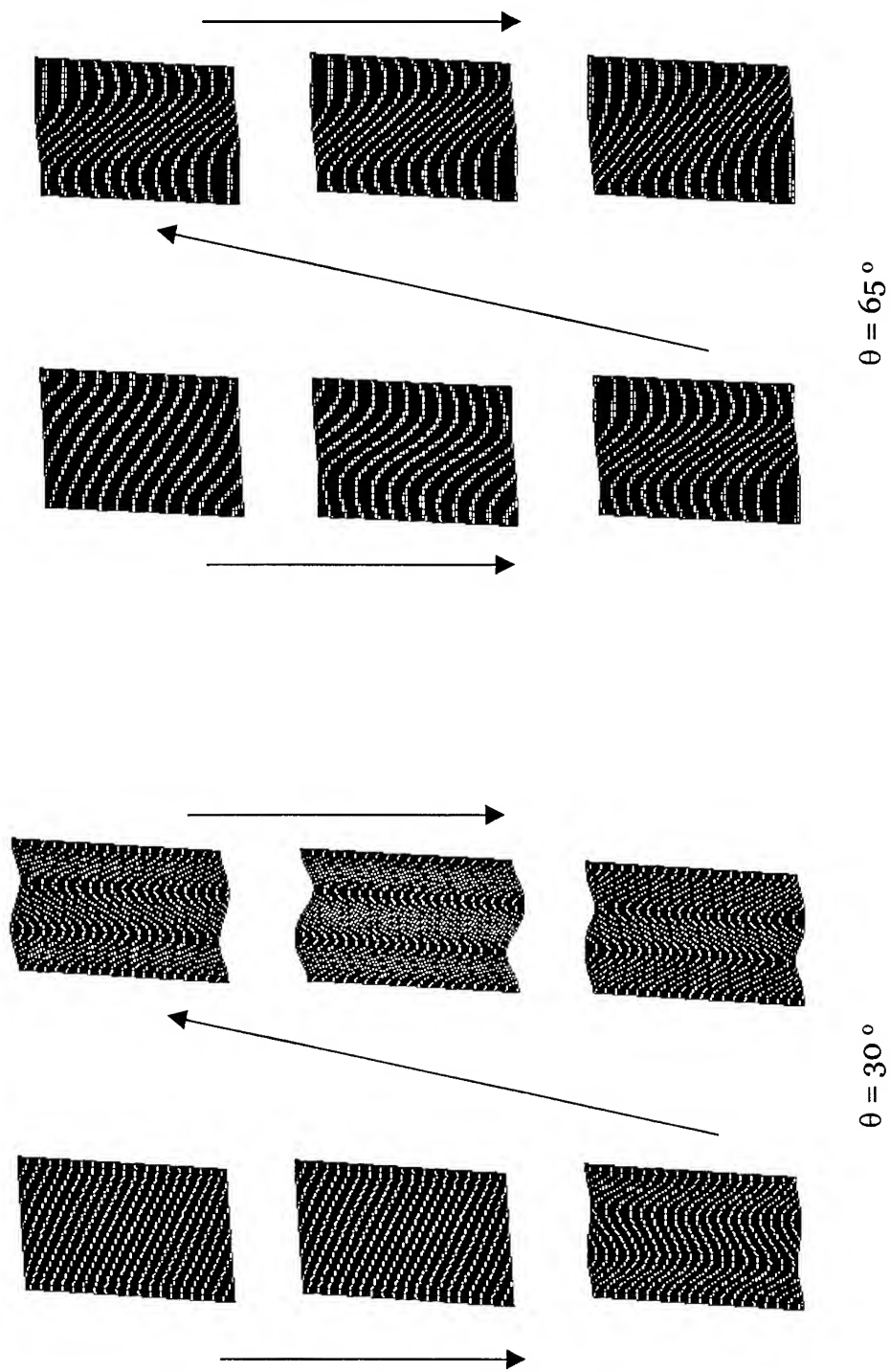
Figure 5.10 Typical deformed shape ( θ = 30°, θ = 65°)

124
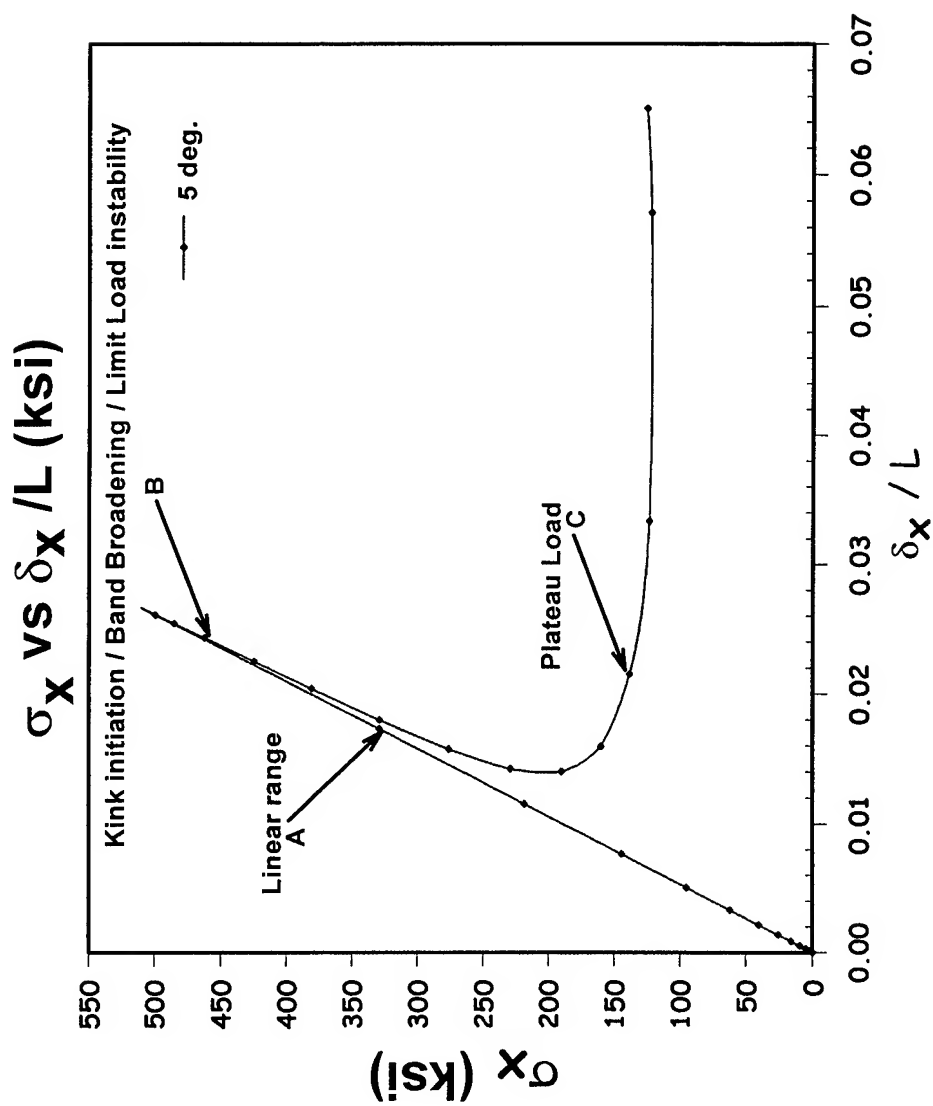
Figure 5.11 Response & deformed shape for (θ = 5°)

125
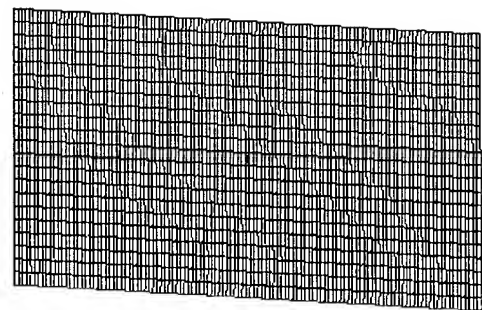
A
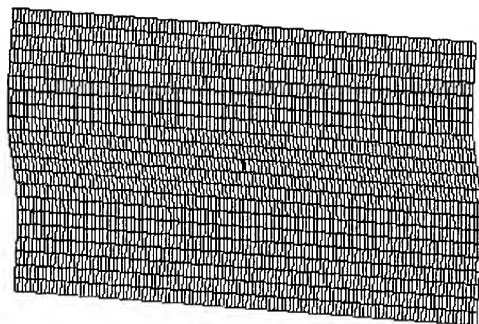
B
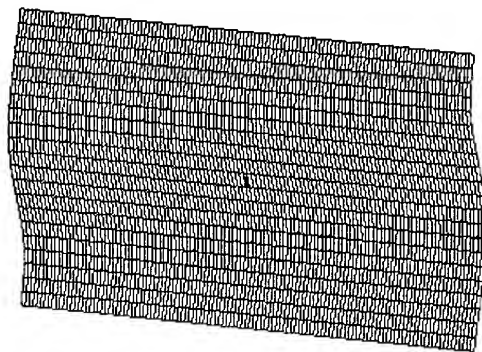
C

**Figure 5.11 Response & Deformed Shape for (θ = 5°), Continued**

126

## 5.8. References

1. Rosen B. W., 1972, "Mechanics of Composite Strengthening", *Fiber Composite materials*, American Society for Metals, Metals Park, OH, 37-75

2. Kim R.Y., "On the Off-Axis and Angled-Ply Strength of Composites", Test Methods and Design Allowables for Fibrous Composites, ASTM STP 734, edited by C. C. Chamis, American Society for Testing and Materials, Philadelphia, PA, 91-108

3. Shuart Mark J., 1988, "failure of Compression-Loaded Multidirectional Composite laminates", *AIAA Journal Vol. 27 No. 9*, 1274-1279

4. ABAQUS® Version 5.8, Reference Manual, 1998, Vol. 1,

5. Zimmerman R. S., Adams D. F., and Walrath D. E., 1984, "Investigation of the Relations between Neat Resins and Advanced Composite mechanical properties, Vol. 1 – Results", *NASA CR-172303*

6. Shuart M. J. and Williams J. G., 1986, "Compression Behavior of ±450 – Dominated Laminates with a Curcular Holr or Impact Damage", AIAA Journal, Vol. 24, 115-122

7. Hahn H. T. and Williams J. B., 1984, "Compression Failure Mechanisms in Unidirectional Composites", NASA TM 85834

8. "D 3410-75 Standard Test Method for Compressive Properties of Unidirectional or Cross-ply Fiber-Resin Composites", 1982, *Annual Book of ASTM Standards, Part 36*, American Society for Testing and Materials, Philadelphia, PA, 1982, 872-880

9. S.J. Song and A. Waas, 1995, " An energy based model for mixed mode failure of laminated composites", *AIAA Journal*, vol. 33, No. 4, 739-745,

# CHAPTER 6

## MATRIX CHARACTERIZATION

### 6.1. Background

Polymers used as matrix materials are referred to as resins. The matrix resin generally consists of 40 to 55 % by volume of a composite material. The main functions of the matrix within the composite are maintaining the composite structure, aligning the reinforcements, acting as a stress transfer medium, and protection of fibers from abrasion and corrosion. The limitation of a composite may well be a function of the matrix used, especially where the matrix shear property or bonding characteristics are important (multidirectional composite).

Thermal stability and the maximum service temperature of a composite are largely determined by the matrix properties. In general, any condition that lowers the glass-transition temperature $T_g$, of the matrix is detrimental to the composite. The glass transition temperature defines the transition between the soft rubbery state of a polymer and its more stiff, or glassy, state. The latter state occurs below the glass transition temperature and is suited for the matrix to transfer loads to the fibers, provide support against fiber buckling, and maintain alignment of the fibers. When operating above the glass transition temperatures the matrix becomes soft and does not perform these functions well.

The two basic classes of resins used in contemporary composites are thermosets and thermoplastics. Thermosets undergo an irreversible chemical change when they are heated or cured. If they are heated again after they have been cured, they will retain their shape until they begin to thermally decompose at high temperature. On the other hand, thermoplastics reversibly melt when heated and solidify when cooled. Once they have been initially melted to form the composite, they can be reshaped by heating above a lower forming temperature. Thermoplastic composites can be reshaped once they have been placed into service. A third derivative of the above two classes of resins is called a toughened thermoset. This is achieved by introducing additives that increases the toughness of the virgin resin.

The reasons for popularity of thermosets are their low melting viscosity, good fiber impregnation, and low processing temperatures. They are also cheaper in cost compared to thermoplastic resins. Epoxy resins are the most popular choice for the advanced composite materials due to their excellent mechanical properties, their retention of mechanical properties when operating in hot and moist environments, and their good chemical resistance. They also have good dimensional stability and exhibit good adhesion to a variety of fibers. However, epoxies cure very slowly and several hours may be required for complete curing. In order to increase the poor toughness of epoxies, new classes of toughened epoxies have recently been introduced. The matrix material of the laminates used in chapter 2 belongs to this class.

As explained in chapter 3, the matrix has a strong influence on several mechanical properties of the composite such as transverse modulus and strength,

shear properties and properties in compression. When composites are subjected to compressive loads, the fibers act as long columns and microbuckling of the fibers can occur. For very low fiber volume fractions ($V_f < 0.4$), fiber microbuckling may occur even when the matrix stresses are in the elastic range. Fiber microbuckling can even be driven due to thermal residual stresses in a low fiber volume fraction composite. However, at higher volume fractions ($V_f > 0.4$), fiber microbuckling may be preceded by matrix "yield" and/or constituent debonding and possibly matrix microcracking.

Compressive failure of a unidirectional composite loaded in the fiber direction may be initiated by transverse splitting of the composite. This occurs when the strain energy released upon splitting exceeds the energy required to create new interfacial surface area. Splitting is driven by pre-existing interfacial cracks that are activated upon compression or tensile loading. Shear failure is another mode of composite failure under compression. This mechanism occurs when the matrix layers between fibers loose their shear carrying capability. It coincides with local shear "yielding" of the matrix.

The important mechanisms for failure of composites under compression are as follows,

1). Transverse splitting failure due to pre-existing flaws (Figure. 6.1)

2). Fiber microbuckling where (Figure 6.2, 6.3)

   a). Matrix is elastic.

   b). Matrix yielding, following the buckling or prior to it.

   c). Constituents debonding, prior to or after buckling.

3). Shear failure, where the matrix locally looses its shear stiffness (Figure 6.4)

The objective of this chapter is to provide a test scheme and appropriate characterization to extract the in-situ response of the matrix material in a fiber composite.

## 6.2. Matrix Characterization

To characterize the matrix, basic tests of the matrix material (simple compression, shear, etc) can be used. However, as stated earlier, residual stresses due to the constraint placed by the fibers reduce the in-situ matrix to behave differently than a pure matrix, cured separately without the fibers. There are two ways to account for this situation. One approach is to solve for the residual stresses and include them in subsequent analysis. Such an approach is prohibitive because of the large number of fibers, the non-uniform packing of the fibers and the uncertainty associated with the fiber/matrix interface that would render such calculation impractical. On the other hand, one can perform tests on the composite and design schemes to extract the matrix properties from the resulting stress-strain plots. The latter approach is adopted in the present works. As stated in chapter 4, Kyriakides et al. [Ref. 4.8] have adopted a similar scheme for characterizing the matrix.

The following tests were performed with a view to characterizing the matrix

1. Simple compression test of a pure matrix coupon at room and high temperature (Figure 6.5).

2. $(+45/-45)_{ns}$ composite specimen compression test at room and high temperature (Figure 6.6).

The result obtained from test 1 reflects the uniaxial stress-strain response of the pure matrix and interpretation is straightforward. The result of test 2 does not lend itself to such straightforward interpretation, however, it is a standard (ASTM D 3518-76) method by which the shear stress-shear strain response of the matrix can be obtained.

Several composite specimens with $[+45/-45]_{12s}$ lay-up were prepared for the second test. Cross-ply specimens left over from the biaxial experiments were used to prepare the required specimens. When this specimen is under uniaxial compression (Figure 6.6), $\bar{\sigma}_x$, the stresses acting on a lamina element at 45° to the $x$- axis shown are

$$\sigma_1 = \frac{\bar{\sigma}_x}{2} + \tau_{xy}$$

$$\sigma_2 = \frac{\bar{\sigma}_x}{2} - \tau_{xy} \qquad (6.1)$$

$$\tau_6 = \frac{\bar{\sigma}_x}{2}$$

The in-plane lamina strains are

$$\varepsilon_1 = \varepsilon_2 = \frac{\bar{\varepsilon}_x + \bar{\varepsilon}_y}{2} \qquad (6.2)$$

$$\gamma_6 = \bar{\varepsilon}_x - \bar{\varepsilon}_y$$

Where, $\bar{\varepsilon}_x, \bar{\varepsilon}_y$ are the axial and transverse strains in the coupon measured with two strain gages. From test data corresponding to 6.1 and 6.2, it is possible to generate the lamina level shear stress / strain plot for a unidirectional lamina (Figure 6.7). The slope of the shear stress-strain plot

(Figure 6.7) will give a plot for $G_{12}(\gamma)$ of the lamina. This is shown in Figure 6.8. Using $G_{12}(\gamma)$, it is possible to convert $G_{12}(\gamma)$ to $G_m(\gamma)$ (matrix) using the Halphin-Tsai relation given below (6.3)

$$G_{12} = G_m \frac{1 + \xi_2 \cdot \eta_2 \cdot v_f}{1 - \eta_2 \cdot v_f}$$

where,
(6.3)

$$\eta_2 = \frac{G_{12f} - G_m}{G_{12f} + \xi_2 G_m} \quad \text{and} \quad \xi_2 = 1 \text{ for random packing of fibers}$$

Combining the above two expressions, the matrix tangent shear modulus is obtained as,

$$G_m = G_{12} \frac{\left(G_{12f} + G_m\right) - v_f\left(G_{12f} - G_m\right)}{\left(G_{12f} + G_m\right) + v_f\left(G_{12f} - G_m\right)} \qquad (6.4)$$

Figure 6.8 indicates the variation of the in-situ matrix tangent shear modulus as a function of shear strain, as well as the lamina tangent shear modulus $G_{12}(\gamma)$, as a function of temperature. From these figures, the shear stress-shear strain of the matrix is computed as shown in Figure 6.9(a).

The next step is to express the matrix uniaxial stress-strain response inferred from the data shown in Figure 6.9, by assuming that the inelastic response of the matrix follows the *J2* flow theory of plasticity with isotropic hardening.

## 6.3. Uniaxial Response Extracted from Shear Response Data

According to the Prandtl-Reuss elastic-plastic equation with a Mises-Heneky yield condition, the ratio of the increment of each plastic strain component to its corresponding deviatoric stress component remains constant, that is [Ref. 6.2],

$$d\varepsilon_{ij}^{p}\big/\hat{\sigma}_{ij} = d\lambda \qquad (6.5)$$

The work conjugate measures of effective stress and incremental plastic strain appropriate for the Mises yield conditions are,

$$\bar{\sigma} = \sqrt{\frac{1}{2}\left[\left(\sigma_{11}-\sigma_{22}\right)^{2}+\left(\sigma_{22}-\sigma_{33}\right)^{2}+\left(\sigma_{33}-\sigma_{11}\right)^{2}\right]+3\left(\tau_{12}^{2}+\tau_{23}^{2}+\tau_{31}^{2}\right)}$$

$$(6.6)$$

$$d\bar{\varepsilon}^{p} = \sqrt{\begin{array}{l}\frac{2}{9}\left[\left(d\varepsilon_{11}^{p}-d\varepsilon_{22}^{p}\right)^{2}+\left(d\varepsilon_{22}^{p}-d\varepsilon_{33}^{p}\right)^{2}+\left(d\varepsilon_{33}^{p}-d\varepsilon_{11}^{p}\right)^{2}\right]+ \\ \frac{4}{3}\left[d\varepsilon_{12}^{p^{2}}+d\varepsilon_{23}^{p^{2}}+d\varepsilon_{31}^{p^{2}}\right]\end{array}}$$

For materials deformed beyond the elastic range, it is convenient to express the total strain increment in terms of two components, the elastic strain increment and the plastic strain increment [Ref. 6.2]. Then,

$$d\varepsilon_{ij} = d\varepsilon_{ij}^{e} + d\varepsilon_{ij}^{p} \qquad (6.7)$$

The plastic strain can be expressed as $d\varepsilon_{ij}^{p} = \hat{\sigma}_{ij}d\lambda$, where the proportionality factor $d\lambda$ can be evaluated from a suitable test of the matrix material as sown below. In the present case is the shear response data. Thus, write,

$$\gamma = \gamma^{e} + \gamma^{p} = F(\tau) \qquad (6.8)$$

then, we can differentiate the above equation to obtain,

$$d\gamma = \frac{d\tau}{G} + d\gamma^{p} = \frac{d\tau}{G} + f'(\tau)d\tau \quad (6.9)$$

G is the elastic shear modulus, which can be inferred from the linear portion of the curve in Figure 6.9. In addition, the plastic term can be evaluated by using polynomial regression fit to the test data and manipulating this as shown below,

134

$$d\lambda = \frac{d\varepsilon_{12}^p}{\hat{\sigma}_{12}} = \frac{d\gamma^p}{2\tau} = \frac{1}{2}\frac{d\gamma^p}{d\tau}\frac{d\tau}{\tau} = \frac{1}{2}\frac{f'(\tau)}{\tau}d\tau = \frac{3}{2}\frac{d\bar{\varepsilon}^p}{\bar{\sigma}} \qquad (6.10)$$

The equivalent stress during plastic deformation is $\bar{\sigma} = \sqrt{3}\tau = \sigma_{11}$. Thus,

$$
\begin{aligned}
d\varepsilon_{11} &= \frac{d\sigma_{11}}{E} + \frac{2}{3}\sigma_{11}d\lambda = \frac{d\sigma_{11}}{E} + \frac{2}{3}\sigma_{11}\left[\frac{1}{2}\frac{f'(\tau)}{\tau}d\tau\right] \\
&= \frac{d\sigma_{11}}{E} + \frac{2}{3}\sigma_{11}\left[\frac{1}{2}\frac{f'\left(\frac{\sigma_{11}}{\sqrt{3}}\right)}{\frac{\sigma_{11}}{\sqrt{3}}}\frac{1}{\sqrt{3}}d\sigma_{11}\right] = \frac{d\sigma_{11}}{E} + \frac{1}{3}f'\left(\frac{\sigma_{11}}{\sqrt{3}}\right)d\sigma_{11}
\end{aligned}
\qquad (6.11)
$$

Finally, the resulting simple compression response relation becomes,

$$\varepsilon_{11} = \int_0^{\varepsilon_{11}} d\varepsilon_{11} = \frac{\sigma_{11}}{E} + \int_0^{\sigma_{11}} \left(\frac{1}{3}\right) f'\left(\frac{\sigma_{11}}{\sqrt{3}}\right)d\sigma_{11} \qquad (6.12)$$

where $E = 2G(1+\nu)$. This result will be discussed in the next section.


## 6.4. Results and Discussion

The results obtained in the manner described above are rather illuminating for a number of reasons. One immediately sees that the in-situ matrix response is markedly different than that would be obtained by the mechanical response from a pure matrix specimen. Figure 6.10 shows this comparison at room temperature and at high temperature.

The pure matrix tests exaggerate the salient features of the in-situ matrix response curve, since there is no constraint for the matrix to flow, when tested in a virgin state. On the other hand, the in-situ behavior shows an earlier "yield" point. In the linear range, the constraint manifests itself as an apparent increase

(artificial) in the elastic stiffness. But this increase, also contributes to an earlier "yield" in the in-situ matrix behavior. Since we need the apparent in-situ matrix behavior, characterizing the matrix in the manner described above is more appropriate for the micromechanics based finite element modeling that will be described in chapter 7. The modeling and results presented in chapter 2, used the pure matrix uniaxial stress-strain curve obtained experimentally and thus, it is not surprising that the failure stress based on the limit load was seem to over-estimate the experimental values.

## 6.5. Figures
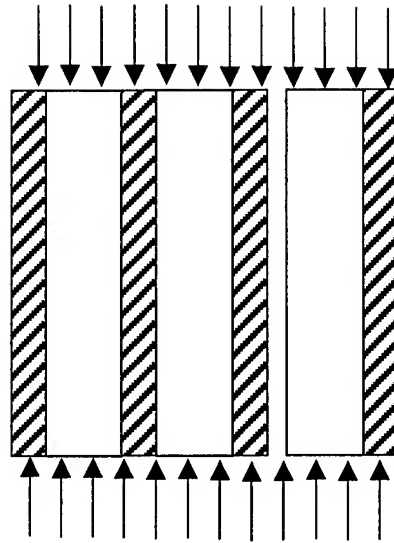


**Figure 6.1 Transverse Tensile Failure Mode**
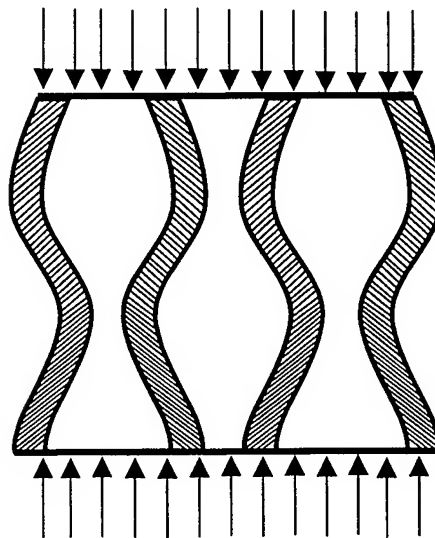


**Figure 6.2 Out of phase mode of fiber microbuckling**
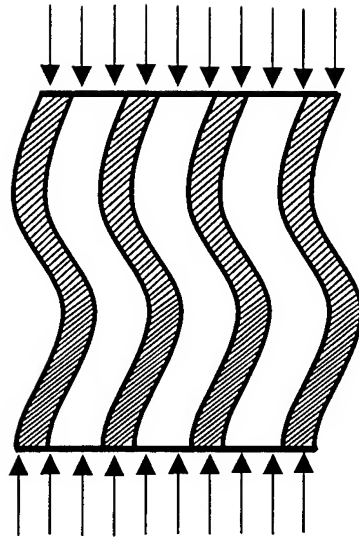
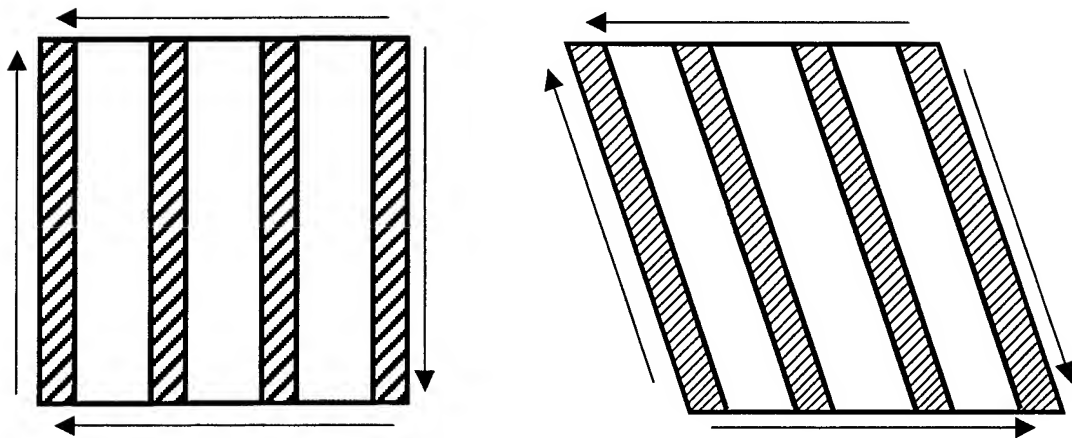**Figure 6.3 In phase mode of fiber microbuckling**



**Figure 6.4 In-Plane Shear Failure Mode**

138

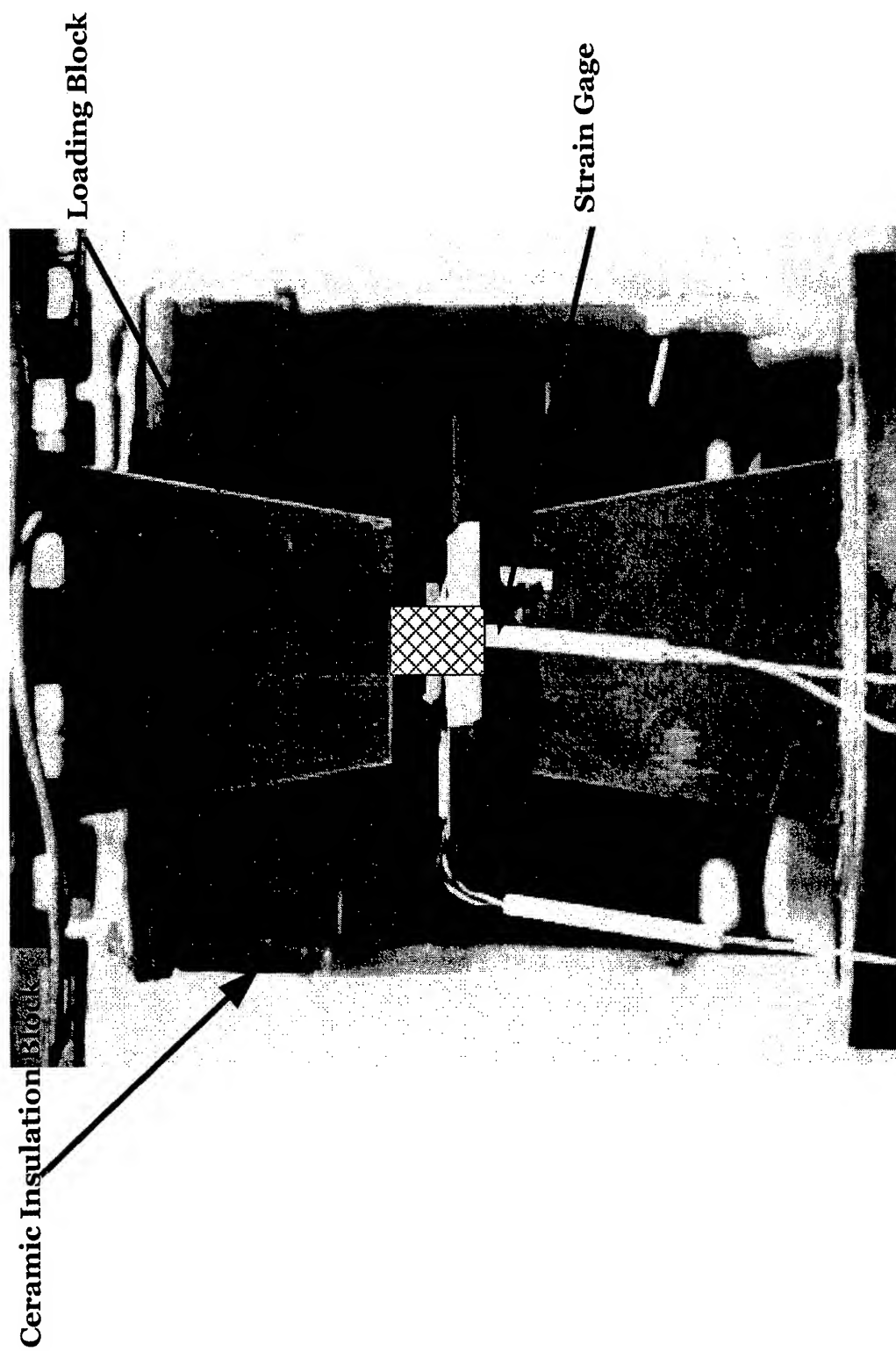Loading Block

Strain Gage

Ceramic Insulation Break

Figure 6.5 Experiment setup for uniaxial compression test of the pure matrix material

139
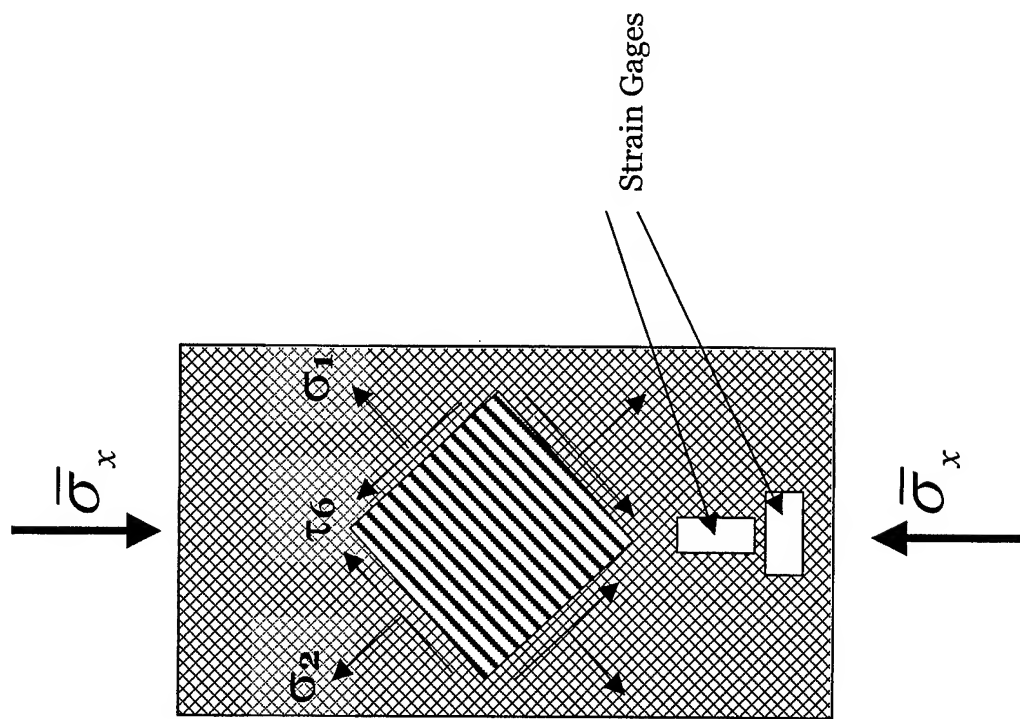
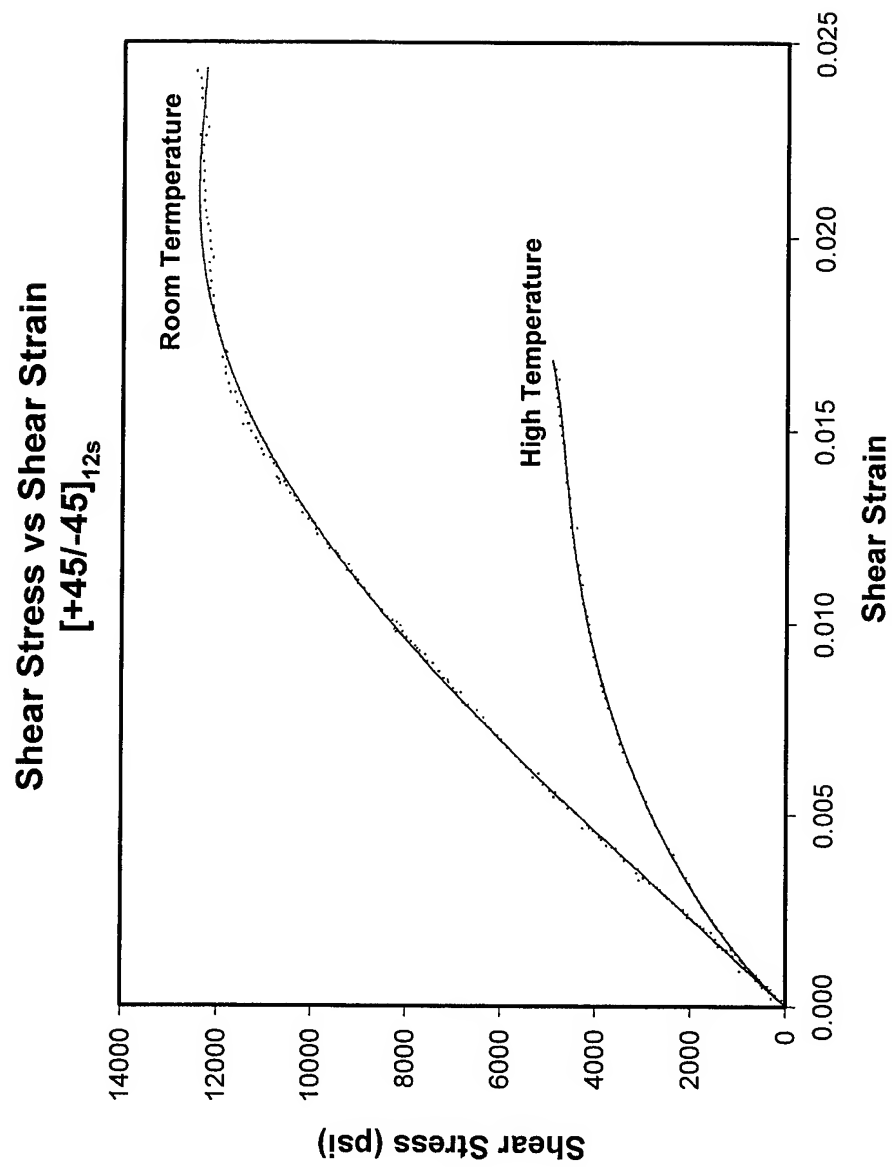Figure 6.6 +45/-45 coupon test of a specimen taken from the cross ply laminates (described in chapter 2)

140

Figure 6.7 Shear stress-shear strain of the (±45)12s laminates response as deduced from following ASTM D 3518-76). Loading rate of 0.0001 inch / sec.
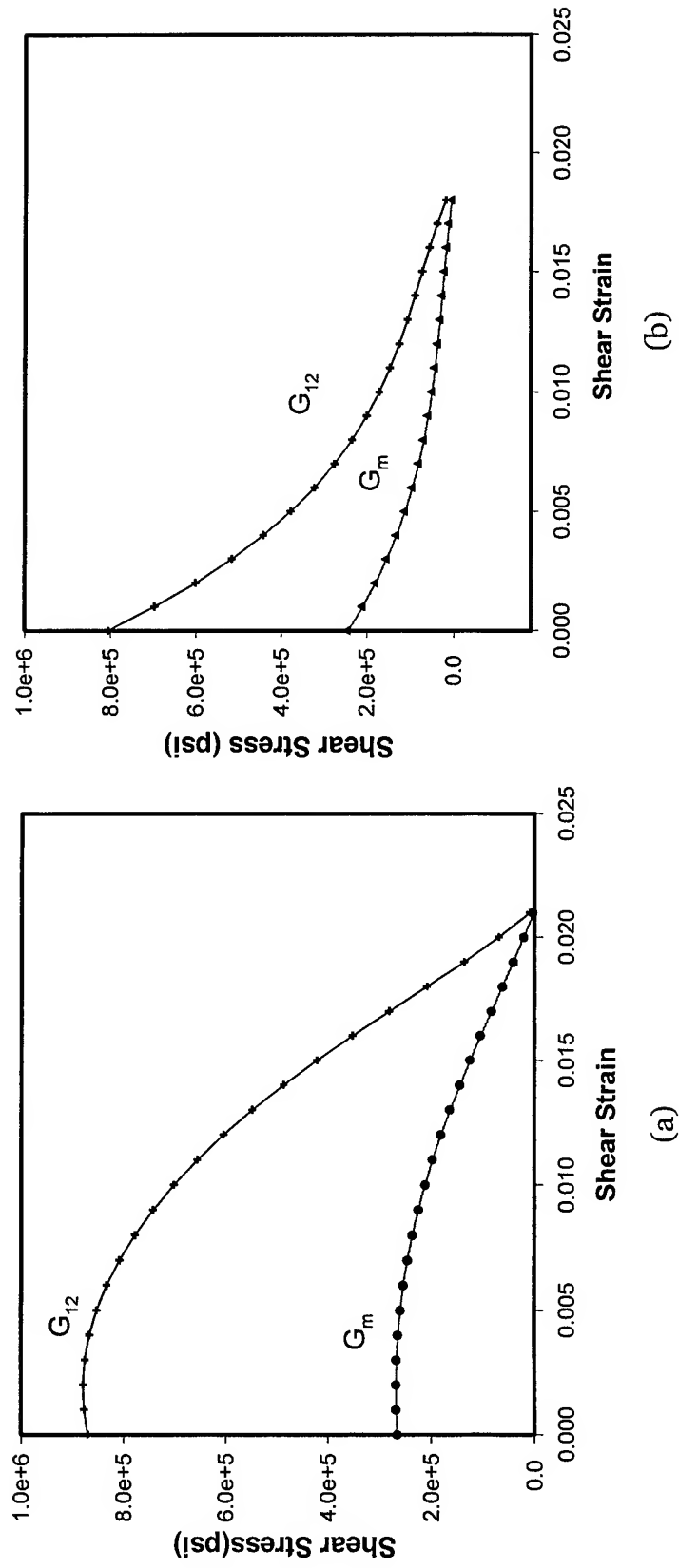
141

Figure 6.8 The matrix shear modulus $G_m(\gamma)$ and the lamina shear modulus $G_{12}(\gamma)$ at (a) Room (25 °C) and (b) elevated (200 °C) temperature
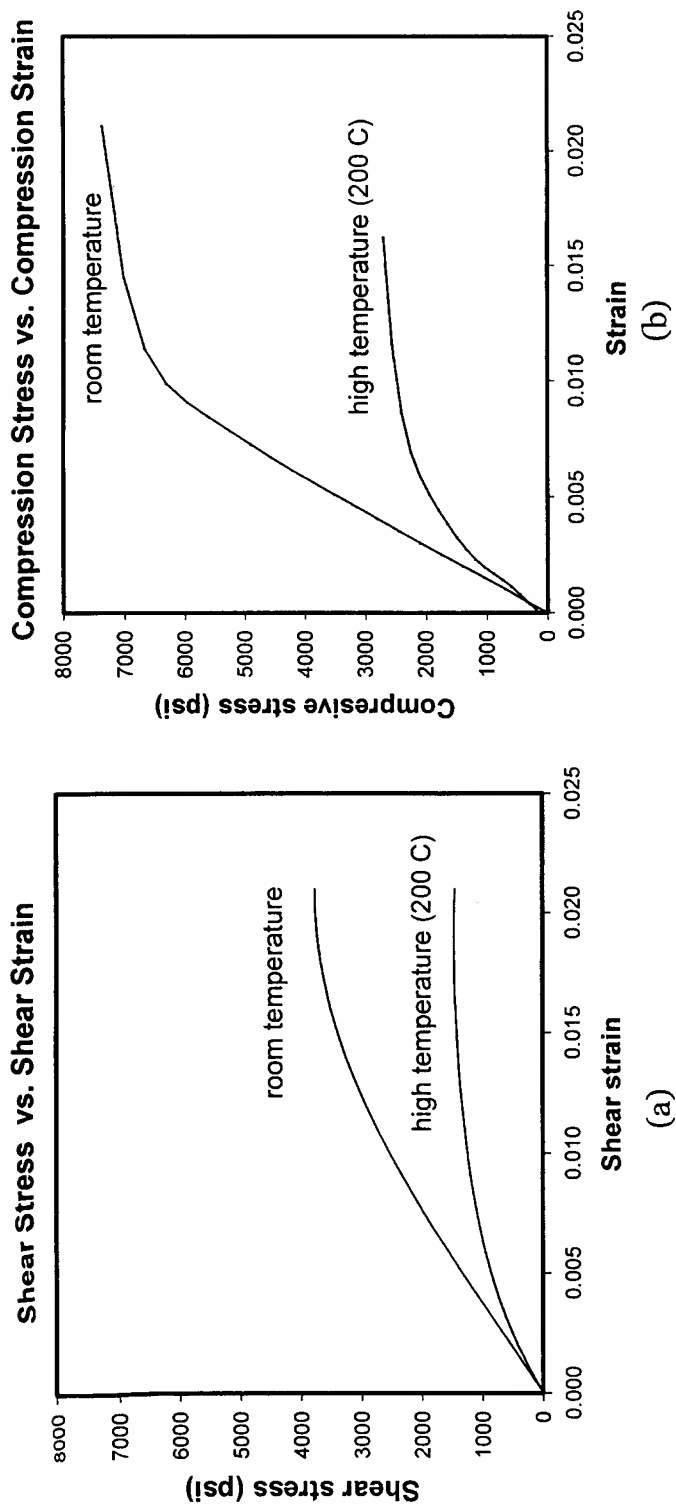
142

Figure 6.9 (a) The matrix shear response and (b) The matrix uniaxial response at room (25 °C) and elevated (200 °C) temperature
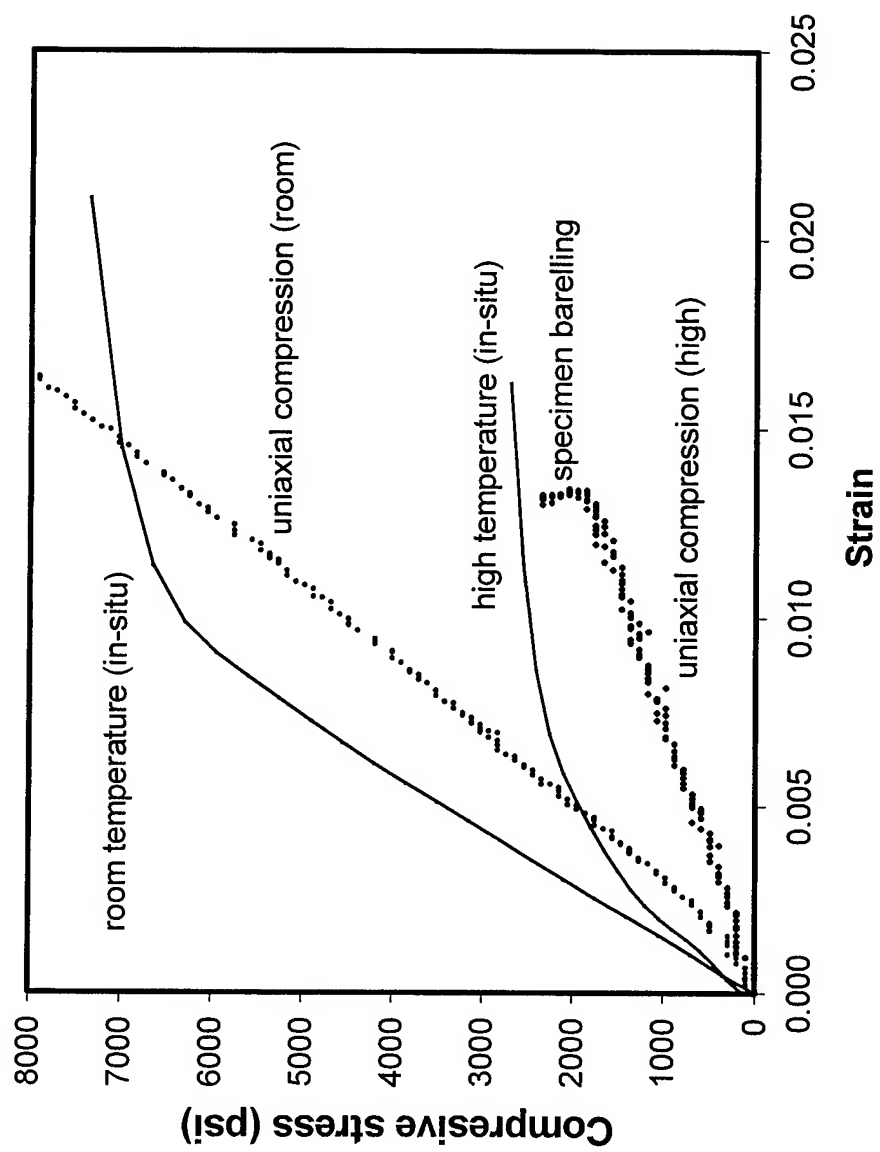
143

**Figure 6.10 Pure matrix test results**

144

## 6.6. References

1. Isaac M. Daniel & Ori Ishai, 1994,"*Engineering Mechanics of Composite Materials*", Oxford University Press, New York

2. Raymond L. Bisplinghoff et al.,1990, "Statics of Deformable Solids", Dover Publications, INC. New York

3. J. M. Whitney, I. M. Daniel & R. Byron Pipes, 1985, "*Experimental Mechanics of Fiber Reinforced Composite Materials*", Monograph No. 4, Society for Experimental Mechanics, Bethel, CT, Prentice-Hall, Englewood Cliffs, NJ, Rev. Ed.

4. I. M. Daniel, 1985, "Methods of Testing Composite Materials" *in Fracture Mechanics and Methods of Testing*, G. C. Sih and A. M. Skudra, Vol. Eds., *in Handbook of Fibrous Composites*, A Kelly and Y. N. Rabotnov, Eds., North Holland Publishing Co., Amsterdam, 1985, 277-373

5. ASTM Standards and Literature References for Composite Materials, 1990, 2nd Ed., *American Society for Testing and Materials*, Philadelphia, PA

6. Standard Tests for Toughened Resin Composites, 1983, Rev. Ed., NASA Reference publication 1092

7. D. F. Adams & D. R. Doner, 1967, "Longitudinal Shear Loading of a Unidirectional Composites", *J. Composite Materials, Vol. 1, No. 1,* 4-17

# CHAPTER 7

# MICROMECHANICS MODEL TO PREDICT FAILURE OF MULTIPLY, MULTIDIRECTIONAL NOTCHED LAMINATED COMPOSITES

## 7.1. Introduction

Throughout this thesis, micromechanics has been used as a tool to predict failure of a macroscopic structural object. In chapter 2, a uniply laminate was modeled, while in chapter 5, $(+\theta / -\theta)_{ns}$ laminates under a single remote unidirectional load were modeled. A theme that is used throughout these chapters is to model and interpret failure in the "large" using models that employ properties in the "small". In this manner, we have avoided using unnecessary empirical factors for the purpose of predicting strength. It must be borne in mind that in many instances, it is relatively easy to predict the stiffness of a structure, but this is not so for strength, since the notion of strength must be articulated and interpreted in terms of experimental observation. That is, strength data obtained from experiments must be accompanied by a description of the mechanism associated with the strength degradation or loss.

A systematic imperfection sensitivity analysis was performed in chapter 4 to estimate the compressive strength failure envelope of a notched laminate with a given constituent geometry (volume fraction, fiber diameter) and material

property (a linearly elastic fiber and an elastic-plastic matrix). In chapter 4, it was possible to understand the experimentally observed failure mechanism of the uniply notched laminate based on the assumption that initial failure of the single uniply lamina triggers the ensuing global laminate failure. Indeed, this was based on the previous experimental results reported in Khamseh and Waas [Ref. 4.2]. The situation treated in this chapter is more complex. Here, we will attempt to predict global failure of a *multidirectional laminate* by analyzing the micromechanics of strength of several isolated lamina. In order to do this, we will first set the stage regarding the assumptions made and revisit the important experimental observations reported in Chapter 2. Both, room and high temperature strength predictions are made.

For a symmetric multidirectional laminate, classical lamination theory (CLT-discussed in Chapter 3) will be employed to characterize the far field. This theory assumes that strains are continuous throughout the laminate. Thus, each lamina is subjected to the same in-plane strain fields. This necessitates that the stress fields within different lamina be different. In addition, in order to characterize the far-field stress field the laminate constitutive properties need to be calculated. This calculation brings in the effects of stacking sequence and construction of the laminate via the computation of the laminate **A, B** and **D** matrices, which are functions of lamina properties, lamina orientation and lamina stacking. More details of CLT and the computation of the **A, B** and **D** matrices can be found in the text of Daniel and Isahi [Ref. 6.1]. Furthermore, through-the thickness stresses are assumed zero since CLT is two-dimensional.

In Chapter 2, cross ply laminates were dominated by kink banding failure while the angle ply laminates failed through fiber/matrix interfacial failure. In many of the instances, the failed surface was a "clean cut", indicating that cracking occurred in the matrix layer confined between two fibers. For quasi-isotropic laminates, which has both angle and zero plies co-existing within the laminate, the failure was dominated by a combination of fiber/matrix interfacial failure and kink banding. Nearly always, both types of damage were visible in the quasi-isotropic laminate.

The approach adopted in this chapter is similar in essence to what was described in chapter 4, except that in the case of quasi isotropic laminates (where angle plies and 0/90 plies co-exist), it becomes necessary to isolate microregions near the cutout corresponding to both an angle ply and a 0/90 ply. Since the far-field strains are the same in all the lamina, this condition is used to find the values of far-field strain corresponding to the initiation of failure. At all times, the stress and strain states in both microregions are recorded for interpretation later. For cross ply laminates, only a single 0 and/or 90 ply needs be analyzed whereas for the pure angle ply laminates, a single angle ply suffices. Thus, in these two latter cases, interpretation is easier than that of the quasi-isotropic laminates. The microregions in relation to the problem that is being studied are schematically shown in Figure 7.1 and Figure 7.2.

## 7.2. Modeling of Compressive Response of a Multiply Multidirectional Laminate

First, the cross-ply laminate case will be presented followed by the quasi-isotropic/angle-ply laminates. Unlike the cross-ply laminates, the quasi-isotropic laminate has two kinds of lamina ($0°$ and $45°$ angled ply). Therefore, it is necessary to separate the two types of lamina in the region of study. The angled ply laminates are analyzed in the same manner as the angle plies in the quasi-isotropic laminates.

Each microregion is situated as shown in Figure 7.1 and Figure 7.2, where the symmetry plane ($y = 0$) is marked as indicated. As in chapter 4, the Lekhnitskii [Ref. 3.5] solution is used to compute the displacement fields along the edges corresponding to the microregion. These displacement fields are computed corresponding to a unit far-field load in the case of uniaxial loading and unit far-filed proportional loads in the case of biaxial loading. Along the bottom edge of the microregion (marked as AD), equilibrium nodal equivalent loads are enforced. That is, the edge AD is under load control, and the remaining edges are under displacement control, so that fibers can deform according to the requirement of far-field equilibrium. It turns out, that if an analysis is conducted with the edge AD free of tractions, the results obtained for the salient features associated with the deformations within this microregion do not change. This is not surprising since the dominant loading is compression along the fibers, whereas the tractions along the bottom edge (edge AD) of the microregion are negligible compared to these dominant compressive stresses. Nevertheless, the

objective is to obtain the limit load that the microregion can sustain and the corresponding far field stresses.

A flow chart of the analysis procedure is indicated in Figure 7.3(a). First, an elastic eigenvalue analysis is carried out in order to obtain the dominant eigenmodes of the microregion. Next, using the eigenmode associated with the smallest non-zero eigenvalue as a perturbation to an otherwise perfect mesh, a response analysis is carried out using the Riks method option provided in ABAQUS®. This is done for a series of imperfection magnitudes. The eigenmodes provide the perturbation shape but not the absolute magnitude of perturbation. Thus, the imperfection magnitude must be specified by the user. In the present work, this is achieved as follows; As shown in Figure 7.3(b), the maximum amplitude of the lowest eigenmode (which occurs along the edge AD) is chosen such that the fiber misalignment angle $\phi$ is approximately in the range $0.05^\circ - 2^\circ$. Since $\lambda$ is known, $\delta$ is chosen such that $\phi$ assures the intended value. After several runs corresponding to different values of $\phi$ are completed, the load maxima associated with the RF1 vs. LPF curves are plotted as a function of imperfection magnitude. Then, be extrapolating the maximum load value corresponding to the perfect case (no imperfection) is obtained. The perfect case corresponds to perfectly straight fibers and this case yields an upper bound for the attainable load maximum.

The fiber (IM7) is assumed to be linearly elastic as before (see Table 2.1), and the matrix (3270 toughened epoxy) property is evaluated from the +45/-45 coupon test, as described in chapter 6. Thus, the in-situ elastic plastic matrix

behavior is incorporated in the present analysis. As discussed in chapter 6, the matrix is modeled as a $J_2$ incremental flow theory solid with isotropic hardening.

The cases studied correspond to those experimental situations for which test data is available as presented in chapter 2. Thus for each laminate, two different runs are performed, one at room temperature and one at elevated temperature. For each temperature, uniaxial and biaxial loading cases are investigated. In this manner, we have studied four different cases for each laminate type. Of course, in the quasi-isotropic case, there are additional four cases, since both the zero ply and the 45 degree ply are investigated. Tables of results corresponding to the above cases are as shown in Table 7.1, 7.2, and 7.3. The results obtained for different imperfection magnitude are also shown in these tables.

## 7.3. FEA Results and Interpretation

A typical load response behavior of a microregion within a cross ply laminate model is shown in Figure 7.4 and a series of deformed plots of the microregion showing the initiation and propagation of damage in the form of kink banding is as shown in Figure 7.5. The numbers indicated in the plot of Figure 7.4 correspond to the series of deformation plots shown in Figure 7.5. The microregion response follows a linear path up to point ②. Although local matrix yielding (in areas of the microregion near the cutout) is indicated prior to the attainment of point ②, the total integrity of this region is not affected much from the matrix yielding because, (1) the area of yielding is small compared to the overall size of the microregion and (2) the fiber rotation is small up to the point of

maximum load (point ②). Thus, the reaction force (RF1) vs. LPF relation is linear up to the maximum load point, although this is not necessarily what could be expected; that is, in general the RF1 vs. LPF behavior is problem dependent. As loading increases, the fibers in the areas where the matrix has become "softer" start to rotate, resulting in a drop of the resultant reaction force (RF1) computed at the symmetry plane (indicated by point ③, in Figure 7.4). As deformation progresses, the region of matrix yielding (and corresponding fiber rotation) is expanding, propagating upward away from the areas near the cutout (until it reaches point ④-see figure 7.5 for the deformed configuration). Once the region expands away from the hole to an area where the effect of the stress gradient have diminished, there is no tendency for further propagating upward and thus the load assumes a fairly constant value (plateau load). After this point, deformation becomes stabilized (fiber rotation stops) and the band of kinked fibers starts to broaden in the x direction without any further sudden drop in the reaction force (⑤). The scenario just described is quite typical of the microregions for all the cases corresponding to the cross ply laminate as well as to the zero ply microregion within a quasi-isotropic laminate. The far-field load (or loads corresponding to biaxial tests) corresponding to point ② is read off and tabulated in Table 7.1 for all the cross-ply laminate cases studied herein.

For the case of quasi-isotropic laminates (Figure 7.2), the responses look different for each lamina (zero ply and 45 ply). Again, the zero ply response is similar to that of the cross-ply model but the far field load at which kink banding initiates is different. The 45 degree ply is modeled just as the zero ply microregion, but the microregion boundaries are taken to be along the material

152

principal directions (In this case the 45 degree and 135 degree directions-see Figure 7.2). Again, displacement boundary conditions are enforced on the edges AB, BC and CD, while edge AD is subject to equivalent equilibrium nodal loads. As loading proceeds, the RF1 vs. LPF relation is very nearly linear (Figure 7.6(a)) and shows no sign of leading to a load maximum preceding a sudden load drop. At the same time, the corresponding plots for the equivalent plastic strain $\varepsilon^p$ vs. LPF (Figure 7.6(b), sampled at the location with coordinates (0.025 in., 0.276 in.)) shows that the matrix elements contained between two fibers along the 45 degree direction and close to the cutout undergo increasing amounts of shearing. As loading proceeds, more and more of the matrix elements undergo large amounts of shearing. Simultaneously, the RF1 vs. LPF plot for the zero ply microregion approaches a maximum load. Thus, the scenario is as follows; the zero ply reaches a maximum load, at which stage kink banding is about to initiate in this ply. At the same time, the integrity of the 45-degree ply is compromised due to the large amounts of plastic straining. Thus, the laminate has a "choice" in selecting that failure path which corresponds to the largest release of energy. As observed experimentally, a fiber/matrix interfacial crack is seen to dominate the failure, but not without some incident kink banding in the zero plies. Thus, here, the maximum load corresponds to the initiation of kink banding which then triggers the mode of fiber/matrix interfacial failure that is observed experimentally in the 45 degree plies. Clearly, we need to have an accurate knowledge and measurement of the critical fiber/matrix interfacial fracture toughness (or the in-situ matrix fracture toughness, since the crack meanders between the fiber matrix interface and along the matrix) to carry out a fracture

mechanics based energy release rate analysis of the 45 degree ply to ensure that it is indeed the mode of failure for which the largest amount of energy is released. Such an analysis is relegated to the future, but details of such an analysis in the context of double cantilever beam specimens is reported in Song and Waas [Ref. 5.9]. For now, we observe the good agreement between the far-field load corresponding to the maximum load prediction and the experimentally measured failure loads as indicated in Table 7.2, especially for the case of small imperfection ($\phi$ = 0.8°). Thus, this lends confidence to our contention that zero ply kinking is the dominant and hence governing mode of failure initiation in notched quasi-isotropic laminates. Such a conclusion, based only on experimental results, has been reached earlier by several previous investigators- see for example, Soutis, Fleck and Smith [Ref. 4.11] and Waas et al. [Ref. 4.4].

The preceding discussion sets the stage clearly for the interpretation of the pure angle ply laminate results. It becomes evident that for the pure angle ply specimens, a structural instability such as kinking does not take place. Instead, failure of these laminates is governed by the shear stress vs. shear strain response of the matrix, the toughness of the fiber/matrix interface and/or the matrix fracture toughness.

For consistency, we have performed several runs corresponding to the test cases depicted in Table 7.3 for the angle ply laminates. As before, a microregion near the cutout and along the material principal directions is isolated and modeled as indicated in Figure 7.2. The details of the analysis procedure are as described for the 45-degree ply of the quasi-isotropic laminates. Again, the RF1 vs. LPF curve and the equivalent plastic strain vs. LPF curves are as shown in

Figure 7.7(a) and Figure 7.7(b). Notice that, in these angle ply laminates, there are no zero plies, thus the only mode of energy release is through plastic straining and fiber/matrix interfacial cracking. For the sake of argument, suppose that the fiber/matrix interfacial toughness is infinite. Then, this laminate will continue to get softer by plastic straining (yielding) of the matrix elements and the gradual spreading of the regions of yielding. However, in reality, there is a finite toughness for the fiber/matrix interface as well as the in-situ matrix. Thus, failure occurs when the strength of the interface is compromised due to plastic straining of the matrix elements (mainly in shear) between any two fibers and located in close proximity to the cutout. Notice that the present problem places a constraint on the edge AB of the microregion to be a symmetry plane throughout the loading process. This situation is contradicted against those cases studied in chapter 5, where the edge AB would have the freedom to rotate globally as loading proceeds.

Since, there are no zero plies to trigger the failure by interfacial fiber/matrix cracking, the angle ply laminates fail when the large amount of plastic straining between any two fibers compromises the fiber/matrix interfacial strength. A fracture mechanics based analysis of this scenario is relegated to the future.

## 7.4 Concluding Remarks

The results of the present micromechanics based global-local finite element analysis shows that the fundamental failure mechanisms of a symmetric multidirectional laminate is kink band formation due to a structural instability of the fibers, especially for laminates containing plies aligned along the remote load

directions (cross-ply and quasi-isotropic laminates). The cross-ply laminates have only 0/90-degree lamina, and the majority of load is carried by simple compression of this lamina. These lamina fail by fiber microbuckling, (on account of a gradually weakening matrix in shear), which in turn progresses to kink band formation due to fiber rotation, followed by band broadening and the triggering of failure in other plies.

For the quasi-isotropic laminate, the majority of the load is still carried by the zero ply lamina. However, the difference between this laminate and the cross ply laminate is the angled ply (45° ply in this case). This 45° ply acts as a buffer zone (lower stiffness, but better shear response). Based on the analysis result, it is possible to postulate that although the matrix layers between any two fibers and situated near the zone of large stress and strain gradient are undergoing excessive plastic deformation (implies the possibility of activating small cracks at the fiber/matrix interface or within the matrix) the integrity of the laminate is still controlled by the zero-plies. However, as soon as the zero ply reaches an instability limit, two possibilities are encountered. Either energy is released by the spreading of the kink band within the zero plies or through interfacial fiber/matrix failure within the now compromised 45-degree plies. The "winner" of this competition is governed by the toughness of the fiber/matrix interfacial fracture toughness and/or the in-situ matrix fracture toughness compared against the zero ply kink band toughness (defined as the energy released per unit advancement of the kinked band). Clearly, in this case, the kink banding triggers the failure since until the zero ply undergoes a load drop, the co-existing 45 degree ply has no possibility of initiating the fiber/matrix interfacial failure.

Thus, the failure load prediction based on the zero ply maximum loads provides a good agreement with the corresponding experimental data.

For pure angle ply laminates, failure is through fiber/matrix interfacial failure since this is the only mode of failure associated with a finite fracture toughness of the interface and/or the in-situ matrix. To incorporate this mechanism in our model, it is necessary to have detailed information of the fiber/matrix interface toughness. This aspect is suggested for future work.

## 7.5. Tables and Figures

| | Uniaxial (ksi) (25 °C) | Uniaxial (ksi) (200 °C) | Biaxial (ksi) (25 °C) | Biaxial(ksi) (200 °C) |
|---|---|---|---|---|
| Analysis | 54 | 25 | 67 | 26 |
| $\phi \approx 0.8°$ | 41 | 22 | 46 | 23 |
| Experiment | 44 | 19 | 37 | 18 |

**Table 7.1 Cross ply analysis result**

| | Uniaxial (ksi) (25 °C) | Uniaxial (ksi) (200 °C) | Biaxial (ksi) (25 °C) | Biaxial(ksi) (200 °C) |
|---|---|---|---|---|
| Analysis | 36 | 20 | 44 | 29 |
| $\phi \approx 0.8°$ | 26 | 15 | 34 | 18 |
| Experiment | 21 | 19 | 26 | 24 |

**Table 7.2 Quasi-Isotropic ply analysis result**

| | Uniaxial (ksi) (25 °C) | Uniaxial (ksi) (200 °C) | Biaxial (ksi) (25 °C) | Biaxial(ksi) (200 °C) |
|---|---|---|---|---|
| Analysis | No Limit Load | No Limit Load | No Limit Load | No Limit Load |
| Experiment | 22.5 | 22 | 35 | 31 |

**Table 7.3 Angle ply analysis result**
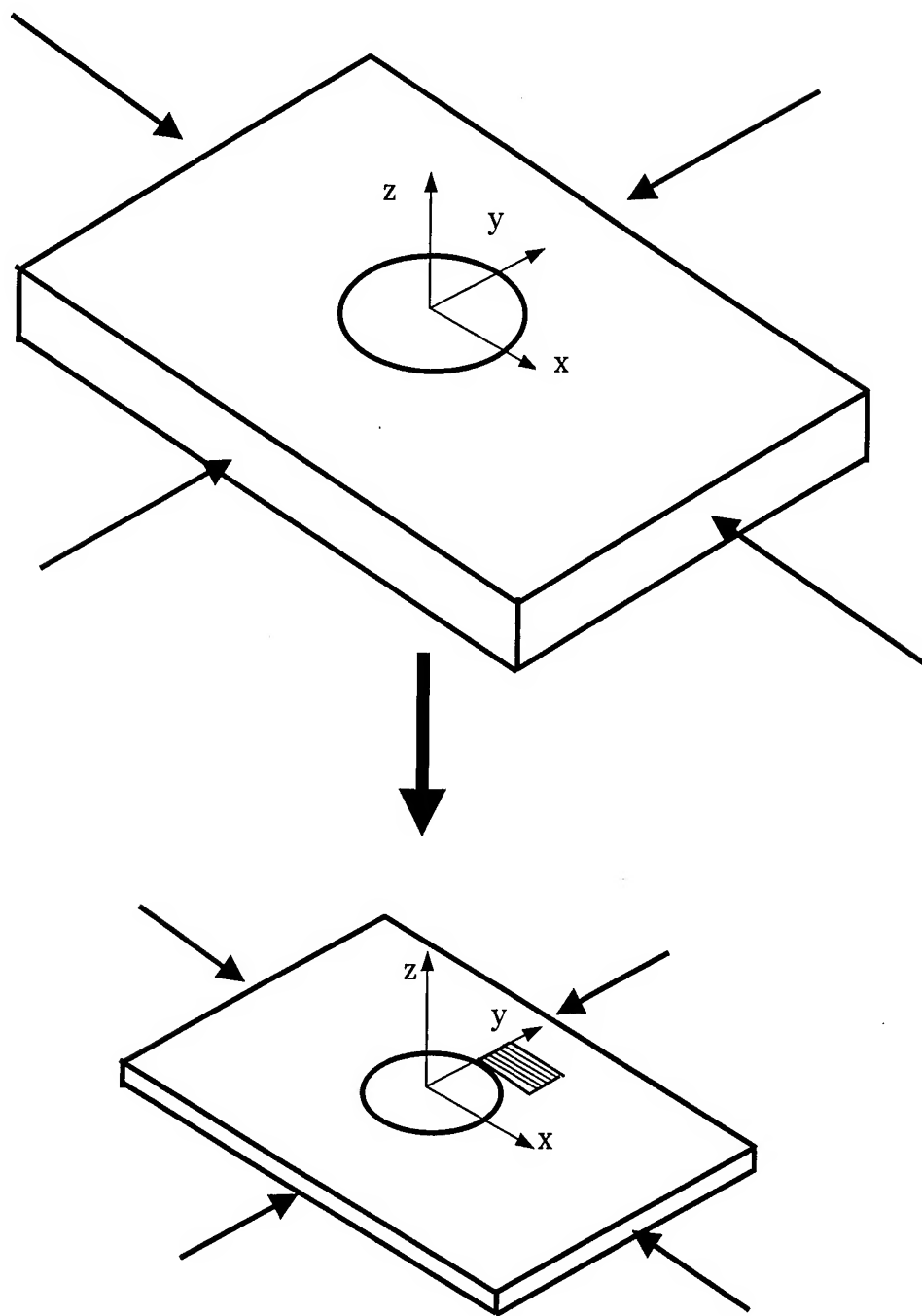
**Figure 7.1 Cross-Ply Laminates Model**

159
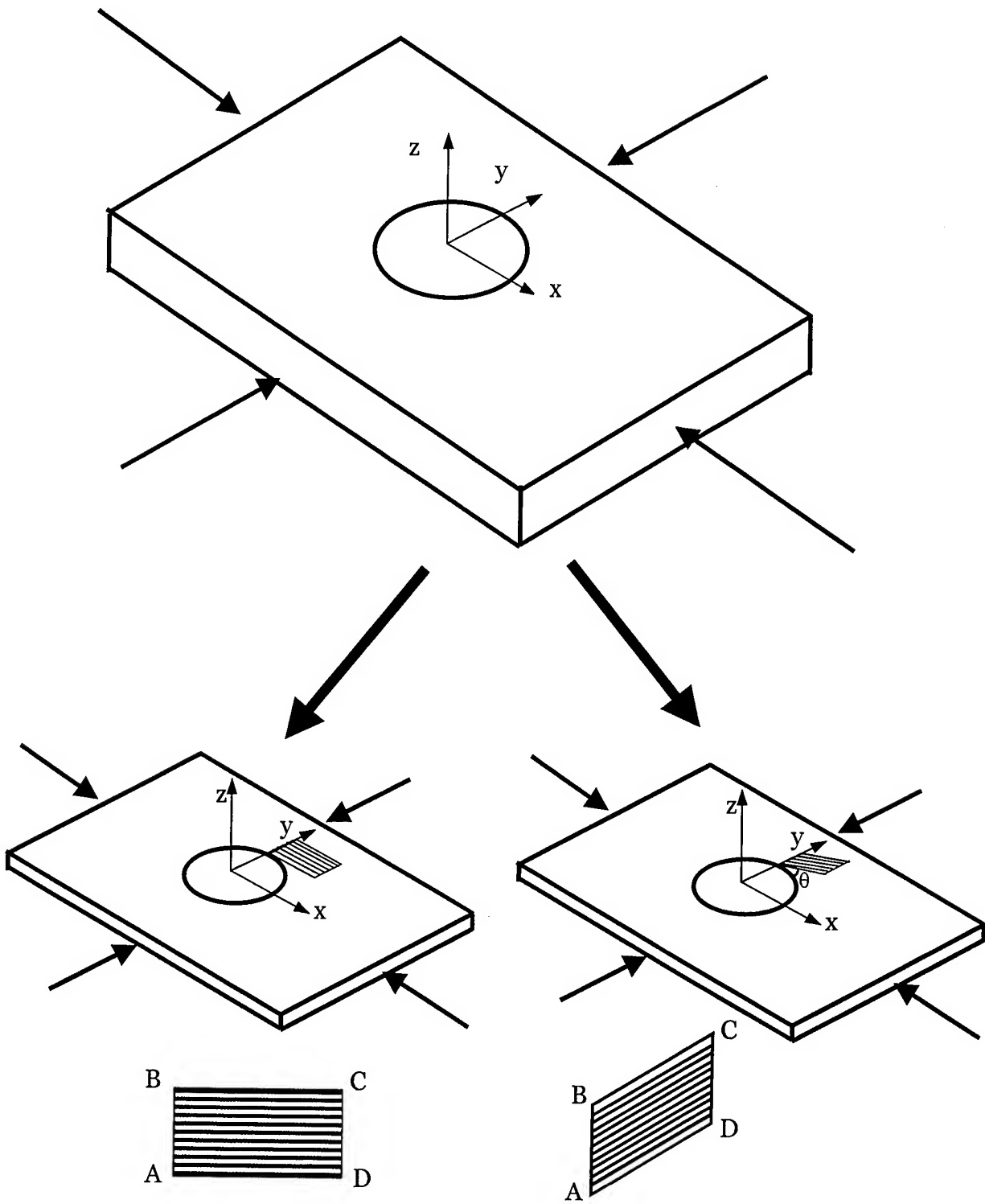
Figure 7.2 Quasi-Isotropic / Angle Ply Laminates Model

Response of Microregion        Extrapolation to Perfect Case
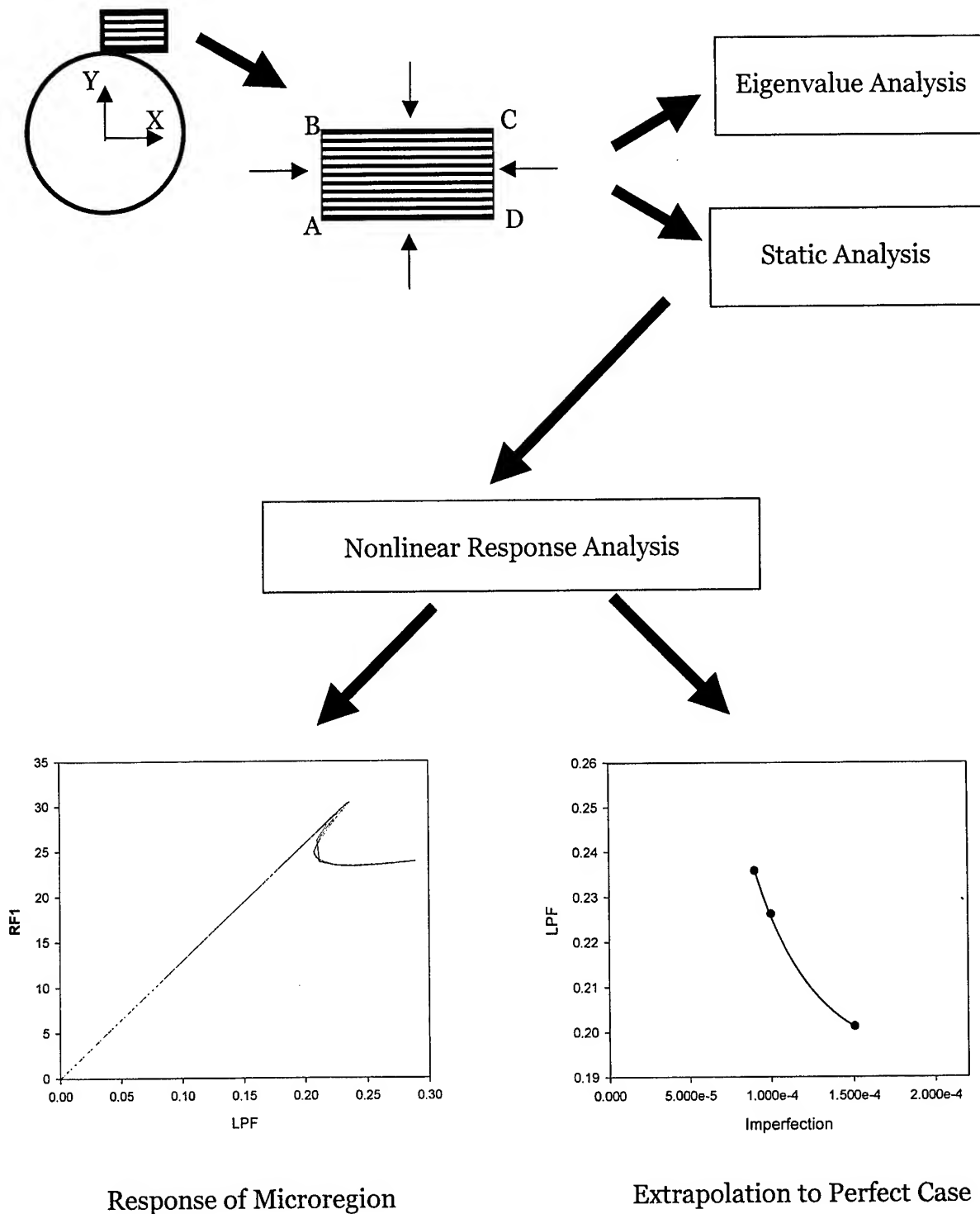
**Figure 7.3(a) Imperfection Sensitivity Analysis Procedure**

161

B   C

Y A   D
X

Eigenvalue Analysis

λ

Maximum deflection δ

$$\phi = \tan^{-1}\left(\frac{\delta}{\lambda}\right)$$
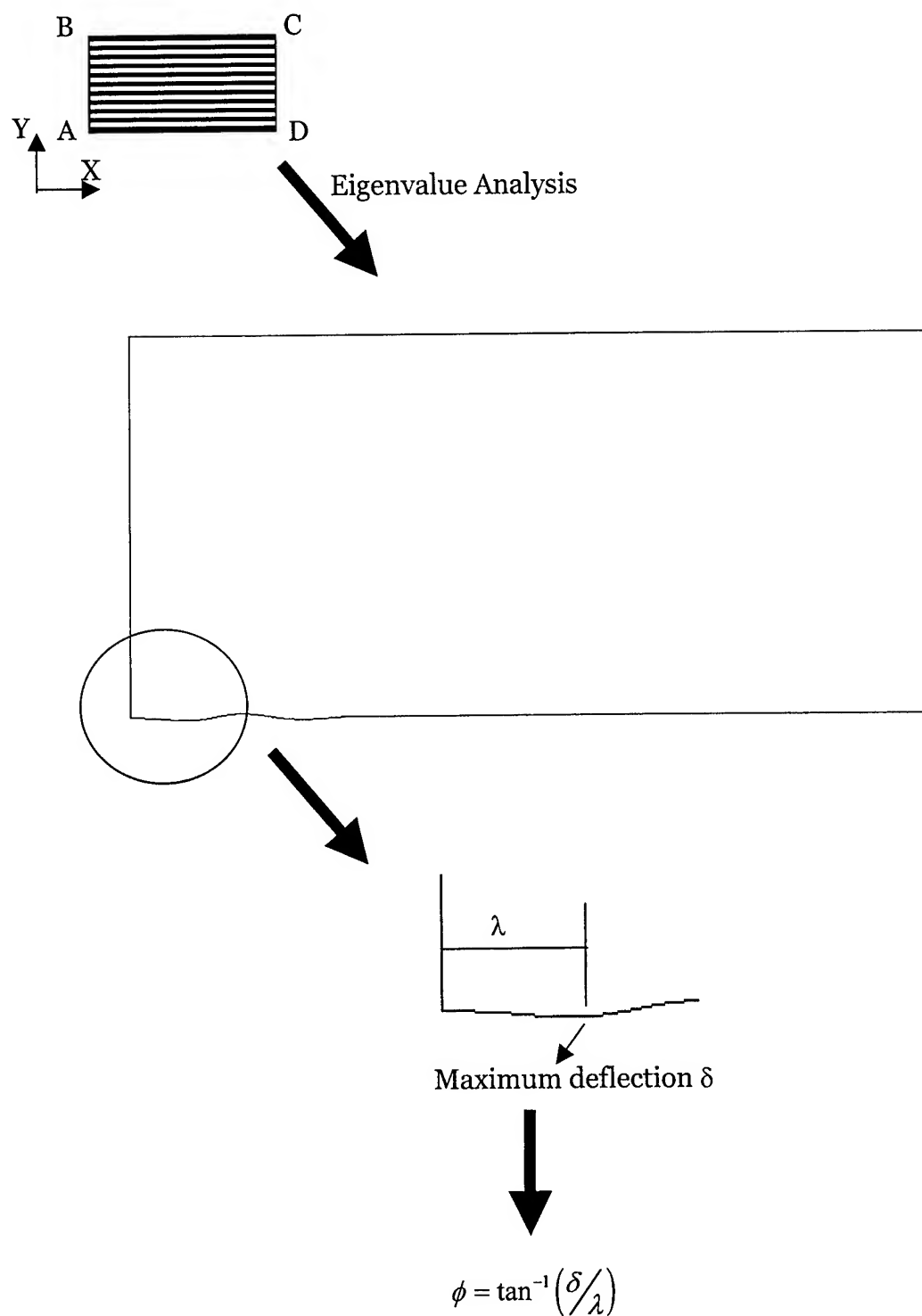
**Figure 7.3(b) Imperfection definition based on φ (maximum deflection angle)**
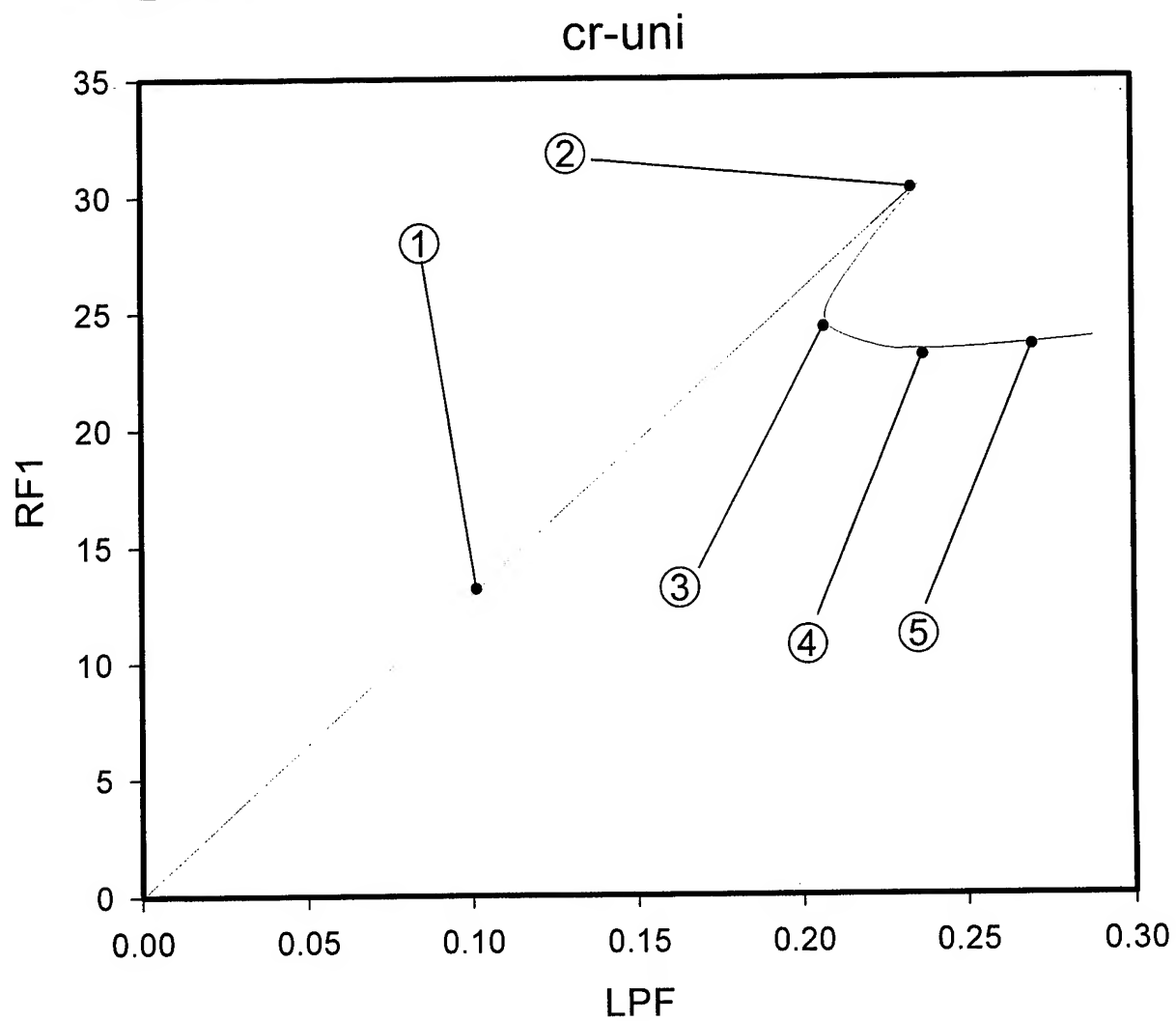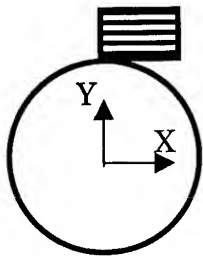
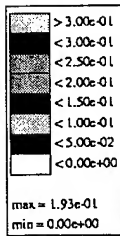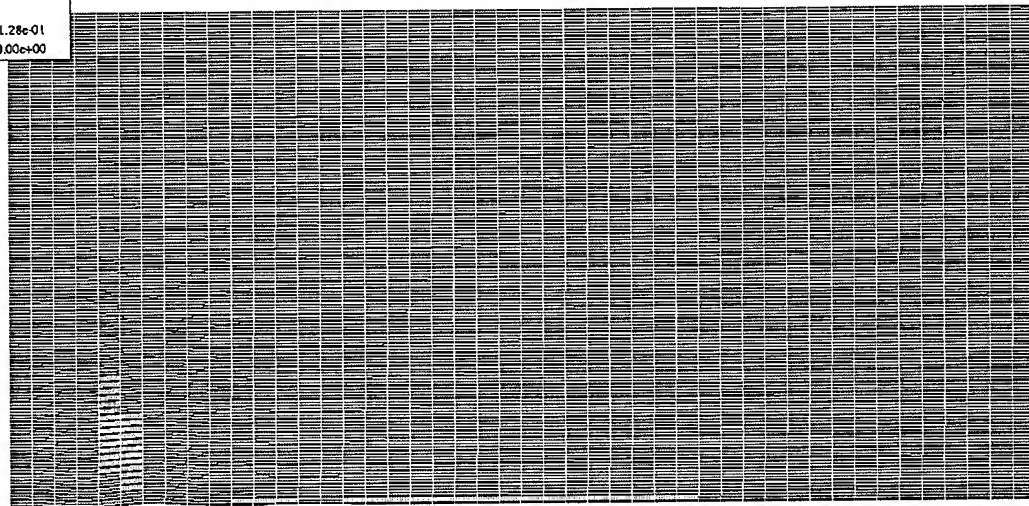Figure 7.4 Response Plot of Typical Cross-Ply Analysis
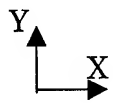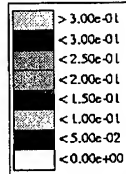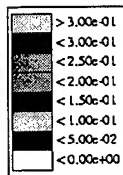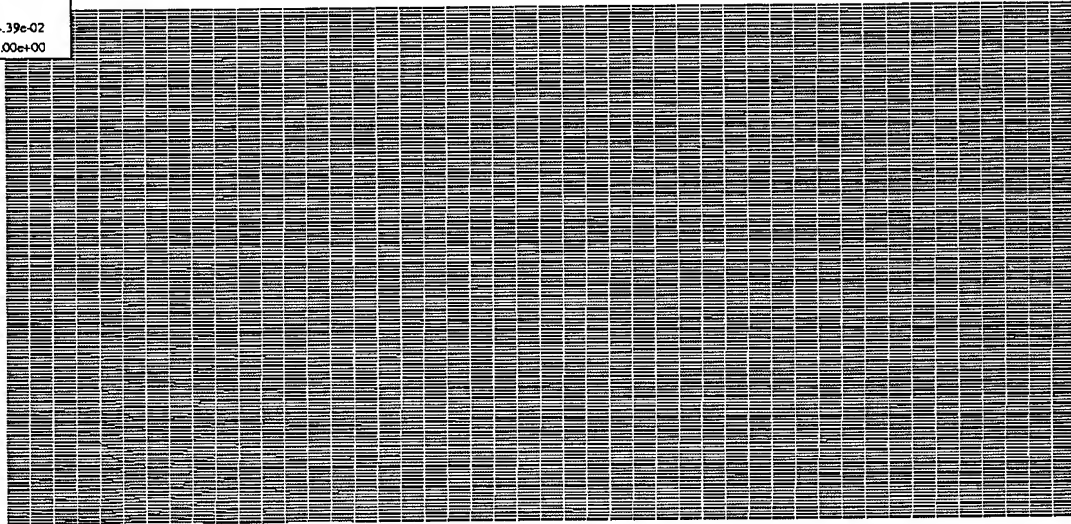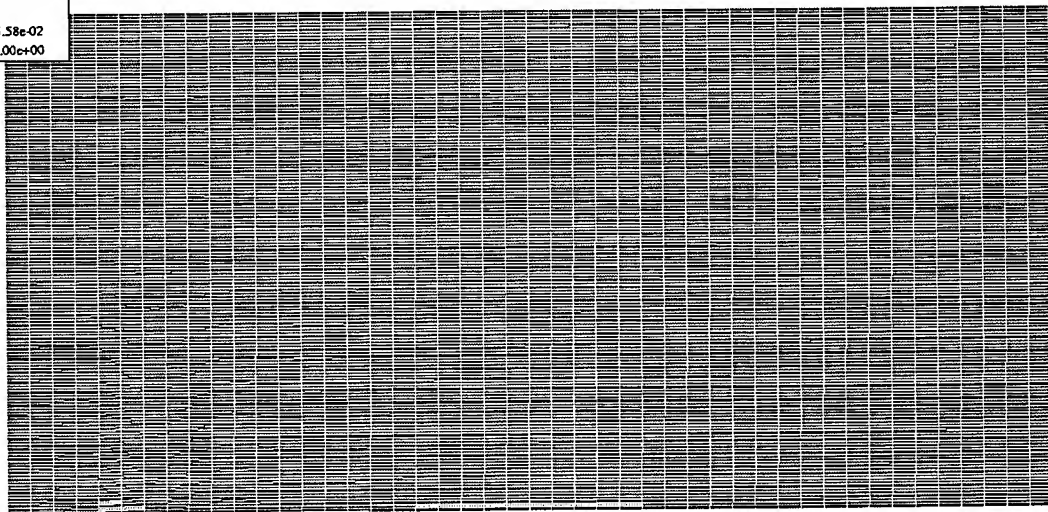
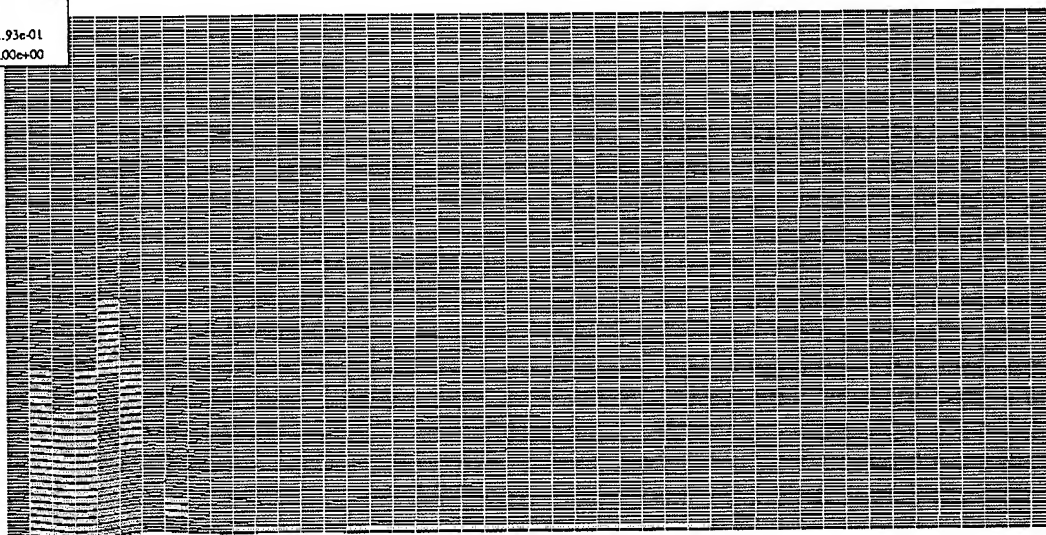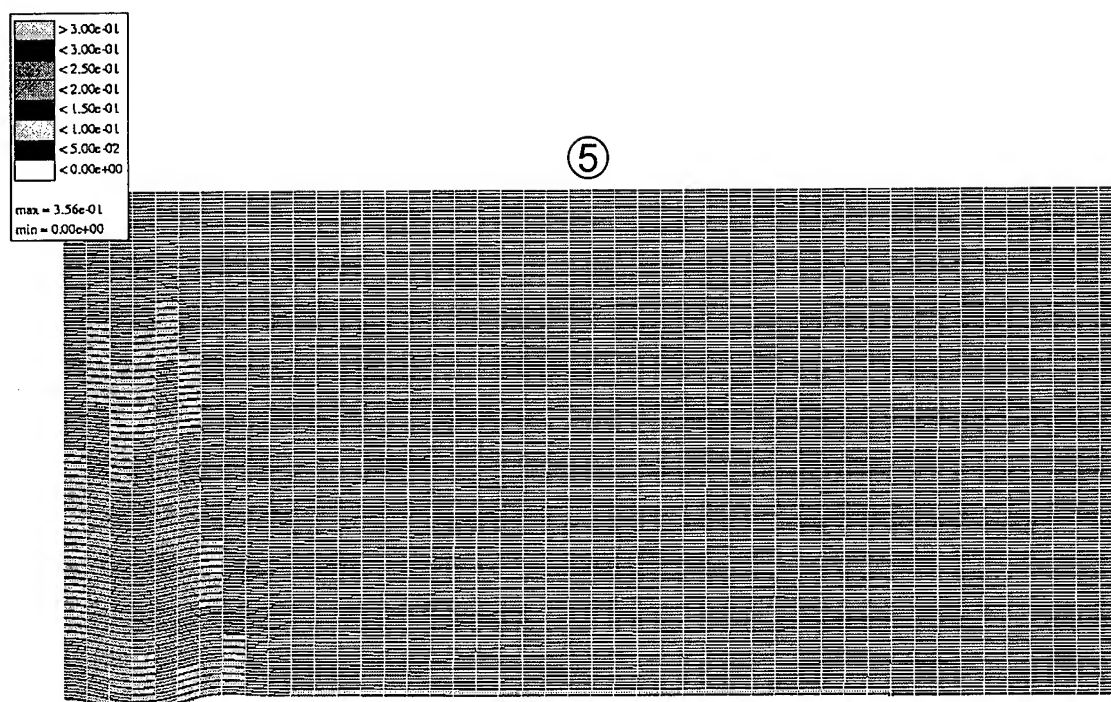Figure 7.5 Deformed Microregion Shape (Equivalent Plastic Strain)
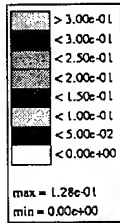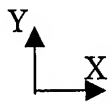
164

**Figure 7.5 Deformed Microregion Shape (Continued)**
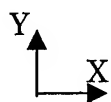
165

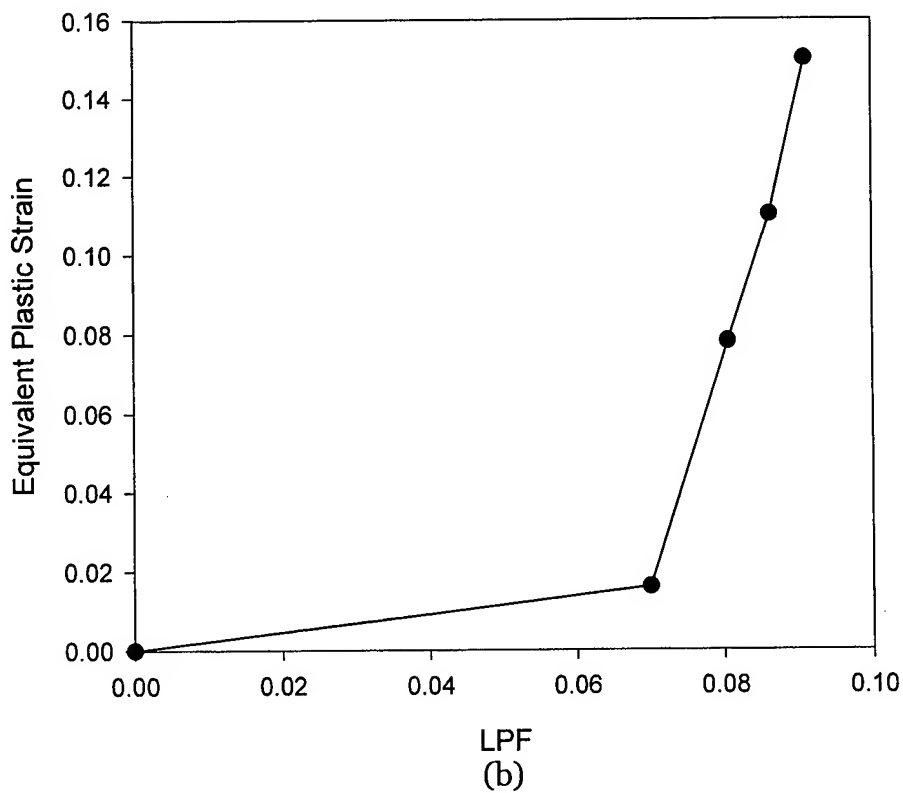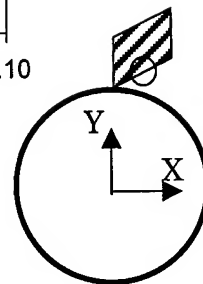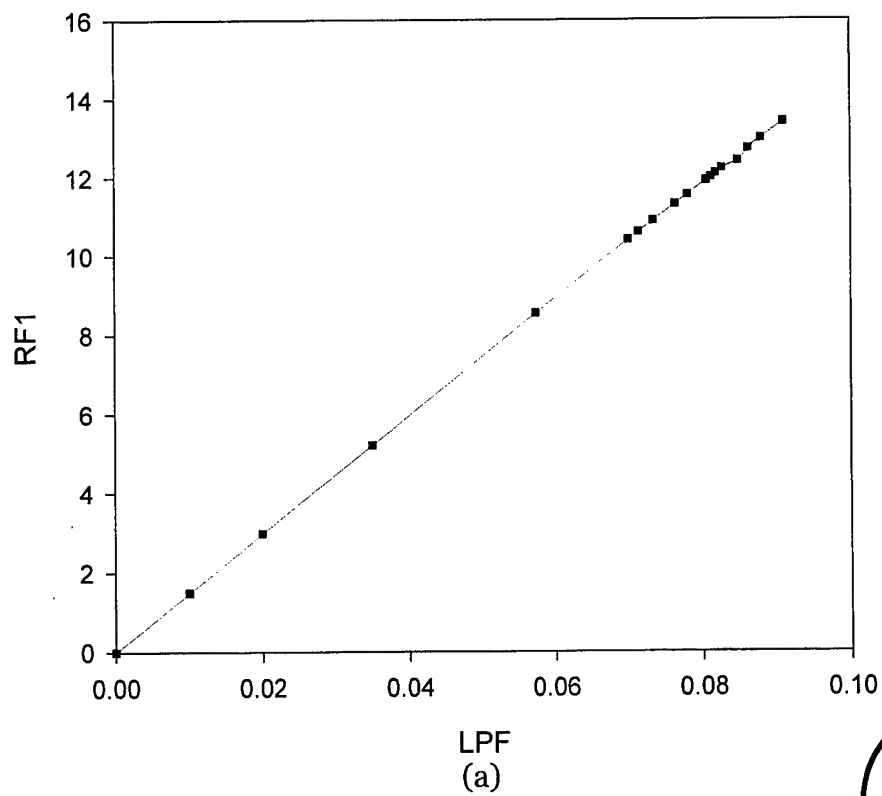**Figure 7.5 Deformed Microregion Shape (Continued)**

Figure 7.6 45° ply response result for a quasi-isotropic laminate (The equivalent plastic strain is sampled at the point with coordinate (0.021 in., 0.271 in.))
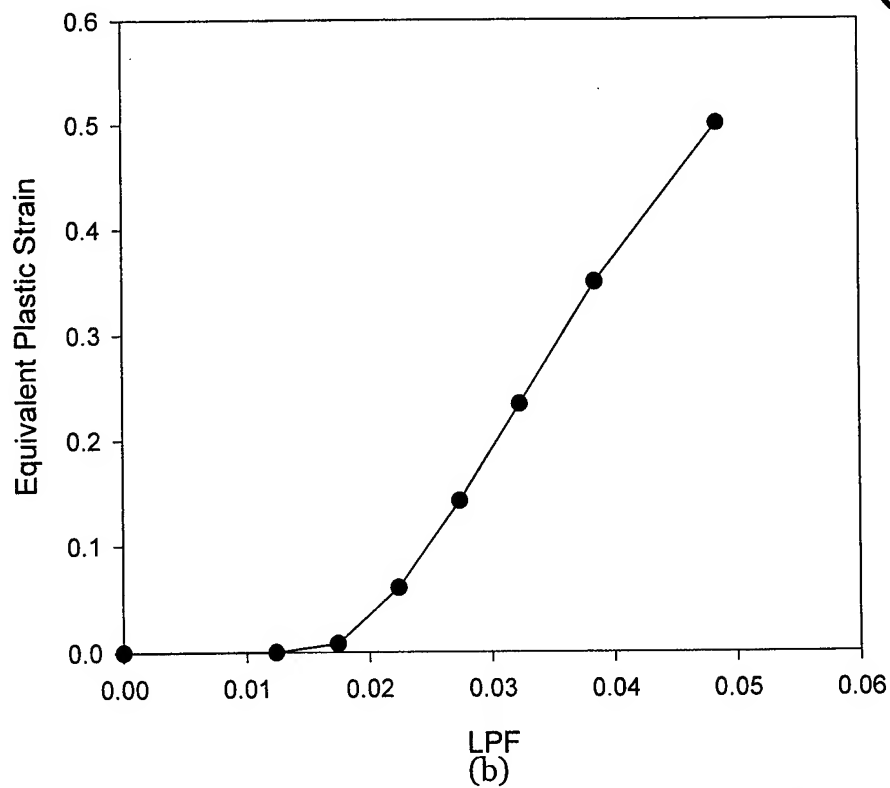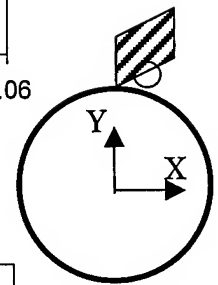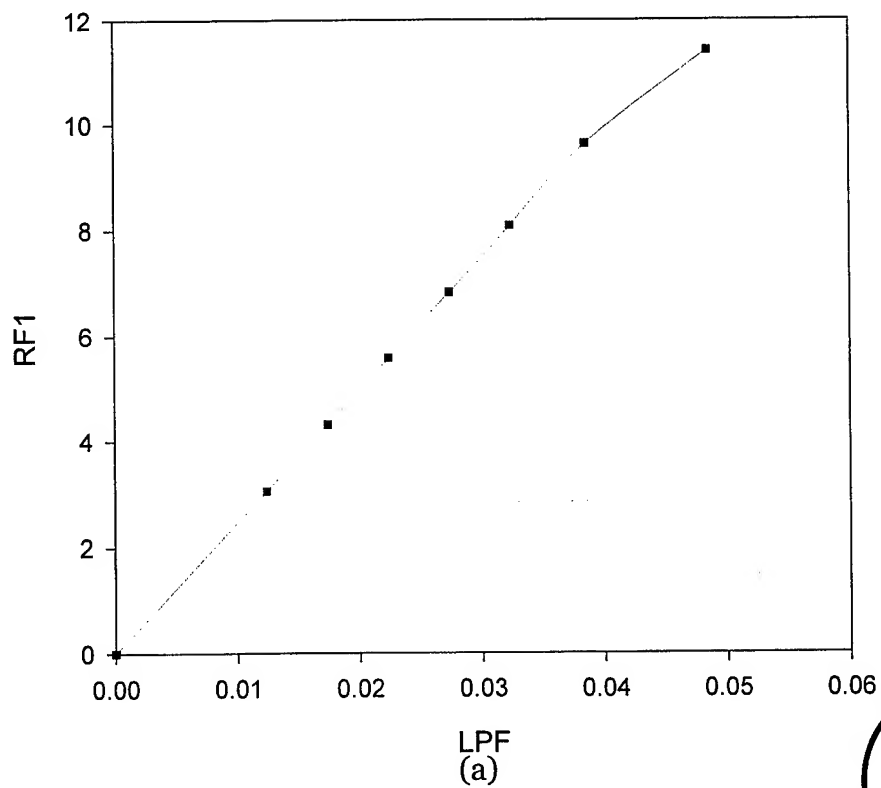
Figure 7.7 Angle ply response result for a angle ply laminate (The equivalent plastic strain is sampled at the point with coordinate (0.019 in., 0.261 in.))

168

## 7.6. References

1. Rosen B. W., 1972, "Mechanics of Composite Strengthening", *Fiber Composite materials*, American Society for Metals, Metals Park, OH, 37-75

2. Kim R.Y., "On the Off-Axis and Angled-Ply Strength of Composites", Test Methods and Design Allowables for Fibrous Composites, ASTM STP 734, edited by C. C. Chamis, American Society for Testing and Materials, Philadelphia, PA, 91-108

3. Shuart Mark J., 1988, "failure of Compression-Loaded Multidirectional Composite laminates", *AIAA Journal Vol. 27 No. 9*, 1274-1279

4. Zimmerman R. S., Adams D. F., and Walrath D. E., 1984, "Investigation of the Relations between Neat Resins and Advanced Composite mechanical properties, Vol. 1 – Results", *NASA CR-172303*

5. Hahn H. T. and Williams J. B., 1984, "Compression Failure Mechanisms in Unidirectional Composites", NASA TM 85834

6. "D 3410-75 Standard Test Method for Compressive Properties of Unidirectional or Cross-ply Fiber-Resin Composites", 1982, *Annual Book of ASTM Standards, Part 36*, American Society for Testing and Materials, Philadelphia, PA, 1982, 872-880

# CHAPTER 8

## CONCLUDING REMARKS

The investigation of failure mechanisms of notched laminated composites was performed throughout this thesis. A systematic experimental approach was performed to establish base data for the failure modeling of laminated composites. Previous test data generated by Khamseh and Waas [Ref. 4.2] was used for the uniply modeling reported in chapter 4. The essential failure mechanisms that govern the failure of composite were found to be: 1). Failure initiation due to instability in the form of kink banding, 2). Failure initiation due to matrix shear failure, also termed fiber/matrix interfacial failure. The kink banding failure mode was incorporated in a micromechanics based model analyzed through the finite element method in conjunction with the commercial code ABAQUS®. Based on the results from this analysis, it was possible to capture the failure initiation envelope of notched uni-directional laminates as a function of the notch size for both remote uniaxial and biaxial loads . The results of this analysis captures the test data well. This is the first time in which starting from basic constituent material properties, a complete analytical model has been presented to predict the failure of a notched structural component, without resorting to any form of empiricism. This important fact must be noted since the procedure we have put forth is a departure from the traditional empirical methods that have been used for this purpose in the Aerospace community.

A unification of different failure mechanisms was introduced next by using available test data from a previous set of experiments (Shuart, 1988). One simple model was seen to capture the transition of failure initiation from unstable kink formation to stable matrix shear failure. A procedure to obtain the in-situ material properties of the matrix was described and used in subsequent modeling of multidirectional laminates. For these laminates a set of specially designed stacking sequences (cross-plies that involve only zero and 90 degree plies, angle plies that involve no zero and 90 degree plies, and quasi-isotropic laminates that involve a combination of zero,90 and angle plies) was first studied experimentally at room and high temperature to obtain a consistent set of uniaxial and biaxial test data for room and elevated temperature. Finally, the test results were predicted by extending the uniply laminate modeling to the multi-directional laminates. Different failure mechanisms were considered and the different mechanisms of failure were interpreted through the analysis predictions.

It is clear at this stage that the fiber microbuckling/kink banding instability of the laminate system is dominating the mechanics of failure of symmetric notched laminates. The shear response of the matrix is highly influential in dictating the mechanics of failure, but the influence of the stress and strain gradients in influencing the failure(in terms of setting the kink band width and the maximum load sustained) is well captured by the procedure that has been put forth in this thesis. A flow chart of this procedure is shown in Figure 8.1 For the quasi-isotropic laminate, the system sustains the load via 0/90-ply lamina, however the initiated damage will propagate through the fiber/matrix interface in the 45 degree plies, where an excessive (and localized) plastic shear deformation is

already well in progress. A similar scenario persists for the pure angle ply laminates, but in this case, the failure mechanism is unique and is through the propagation of damage via fiber/matrix interfacial cracking.

**Known Data**
volume fraction
fiber properties
matrix stress-strain curve
fiber / matrix geometry

Find displacement field corresponding to given loading analytically or via a commercial Code.
These are the Macroscopic Stress and Strain Fields. In this case, we used a Closed Form Solution (Lekhnitski, 1964)

Perform nonlinear load-response analysis with micromodel that incorporates nonlinear constitutive response of matrix

Analysis of FEM data and comparison with experimental results

Obtain bounds for failure loads and sensitivity of prediction, corresponding to the degree of "softening" of the matrix
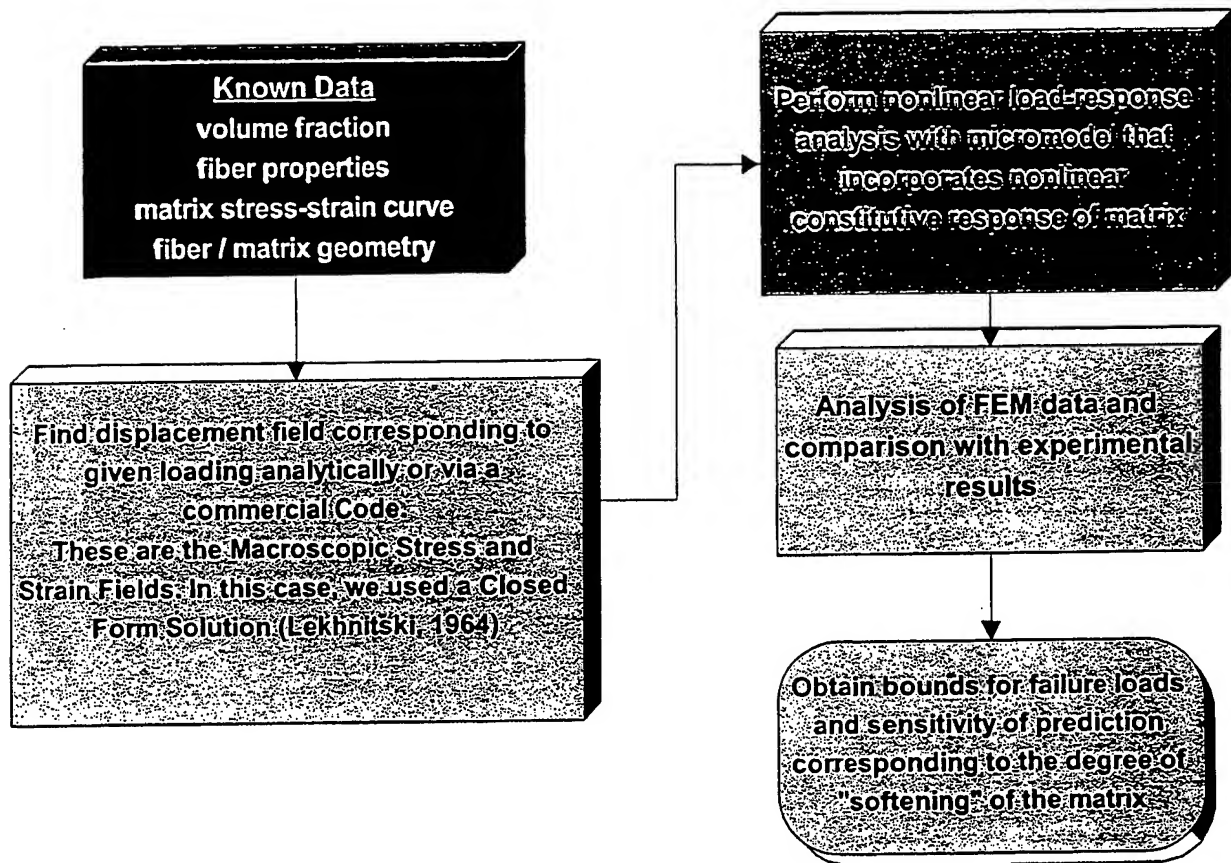
**Figure 8.1 Design Flow**

173

## Dissemination of Results

The scientific accomplishments under this grant has been presented at several National and International Conferences and through five journal publications as given below:

### Journal Papers

1) A. Waas, J.H. Ahn and A.R. Khamseh, "Compressive Failure of Notched Uniply Composite Laminates", Composites Part B,vol 29B, pp75-80, 1998.

2) J. H. Ahn and A. Waas, "A Micromechanics-Based Finite Element Model for Compressive Failure of Notched Uniply Composite Laminates under Remote Biaxial Loads", Trans. ASME J.Eng. Materials and Technology, vol. 121, pp360-366, July 1999.

3) J. H. Ahn and A. Waas, Micromechanics Based Predictive Model for Compressive Loading of Angle Ply Laminates, accepted to appear in the AIAA Journal, 2000.

4) J. H. Ahn and A. Waas, "A Micromechanics-Based Finite Element Model for Compressive Failure of Notched Multidirectional Composite Laminates under Remote Biaxial Loads", in preparation, to be submitted to AIAA Journal, 2000.

5) J. H. Ahn and A. Waas, "An Experimental Investigation of Compressive Failure of Notched Multidirectional Composite Laminates under Remote Biaxial Loads", in preparation, to be submitted to AIAA Journal, 2000.

### Conference Papers

1) A. Waas and J.H. Ahn, "Kink Banding Model for Compressive Failure of Gr/Epoxy Laminates," presented at ASME Winter Annual Meeting, Nov. 1996.

2) A. Waas and J.H. Ahn, "A Predictive Model for Compressive Failure of Biaxilly Loaded Gr/Epoxy Laminates," presented at AIAA SDM Meeting, April 1997, Orlando, Florida; paper to appear in Proceedings of the 38 th AIAA SDM Conference, AIAA Paper No. CP97-1565

3) A. Waas and J.H. Ahn, "Kink Banding in Notched Fiber Composites; A predictive model," presented at American Society of Composites Meeting, Nov. 1997, Dearborn, MI ; paper to appear in Proceedings of the 1997 ASC Meeting.

4) Waas, A. and Ahn, J.H, (1997), "A new model for Compressive Failure Mechanisms of Laminates", ASME Winter Annual Meeting, Nov. 97.

5) J. Ahn and Waas, A., (1998), "Response of biaxially loaded notched composite laminates", 39 th. AIAA SDM, April 1998, Long Beach, CA.

6) Jung H. Ahn and Anthony M. Waas, Compressive Response and Failure of Angle Ply Laminates, ASME International Congress 1998, Nov. 15-20, 1998, Anaheim, CA

7) Jung H. Ahn and Anthony M. Waas, "The Elevated Temperature Compressive Response of Notched Multi-Ply Laminated Composites", <u>40 th. AIAA SDM, St. Louis, MO, 1999</u>.

8) J. H. Ahn and A. M. Waas, Failure Mechanisms in Angle Ply Composites, <u>International Conference on Composites Engineering, July 1999, Orlando, Florida.</u>